Nanomaterial-Enabled Chemiresistive Devices for Sensing Applications

A thesis submitted
in partial fulfilment of the requirements
for the degree of

Doctor of Philosophy

by

Nirmal Chandra Roy

Centre for Nanotechnology
Indian Institute of Technology Guwahati
Guwahati-781039, Assam, India

January 2022


भारतीय प्रौद्योगिकी संस्थान गुवाहाटी
Indian Institute of Technology Guwahati

Dedicated to My Parents

&

Sister and Brother


भारतीय प्रौद्योगिकी संस्थान गुवाहाटी
Indian Institute of Technology Guwahati

Centre for Nanotechnology
Indian Institute of Technology Guwahati
Guwahati-781039, Assam, India

Statement

The work contained in the thesis entitled "**Nanomaterial-Enabled Chemiresistive Devices for Sensing Applications**" has been carried out by me at Indian Institute of Technology Guwahati under the supervision of Prof. Tapas K. Mandal and Prof. Harshal B. Nemade. This thesis has not been submitted elsewhere for the award of any degree.

Nirmal Chandra Roy

Roll No.- 156153001
Centre for Nanotechnology
Indian Institute of Technology Guwahati
Guwahati-781039, Assam, India

Centre for Nanotechnology
Indian Institute of Technology Guwahati
Guwahati-781039, Assam, India

Certificate

This is to certify that the work contained in the thesis entitled "**Nanomaterial-Enabled Chemiresistive Devices for Sensing Applications**" have been carried out by **Mr. Nirmal Chandra Roy** (Roll No.- 156153001) at Indian Institute of Technology Guwahati under our supervision. This thesis has not been submitted elsewhere for the award of any degree.

Thesis Supervisors

Prof. Tapas K. Mandal	**Prof. Harshal B. Nemade**
Professor	*Professor*
Department of Chemical Engineering & Centre for Nanotechnology	*Department of Electronics and Electrical Engineering & Centre for Nanotechnology*
Indian Institute of Technology Guwahati	*Indian Institute of Technology Guwahati*
Guwahati-781039, Assam, India	*Guwahati-781039, Assam, India*

January 2022

Acknowledgements

The completion of this Ph.D. thesis would never be possible without the help and support of these people. It is my pleasure to acknowledge everyone who contributed to the journey towards the successful completion of this Ph.D. thesis.

First and foremost, I would like to thank my thesis supervisors Prof. Tapas K. Mandal and Prof. Harshal B. Nemade, for giving me an opportunity to work in an exciting area of research. I am highly obliged to them for their continuous guidance, encouragement, essential advice, and inspiring discussions. In spite of their busy schedule, they always happily spent time analysing the problems and gave needed suggestions for the betterment of my work. The experience of working with them will definitely have a far-reaching influence on my life. I consider it an honour to work under them.

I am also grateful to my doctoral committee members, Prof. Siddhartha Sankar Ghosh, Department of Biosciences and Bioengineering, Prof. Dipankar Bandyopadhyay and Prof. Partho Sarathi Gooh Pattader, Department of Chemical Engineering, for their timely and invaluable suggestions and efforts during my thesis work.

My sincere acknowledgement goes to all the faculty and staff members of the Centre for Nanotechnology for their support and co-operations during all this time. I would also like to thank the Central Instrument Facility, Department of Chemical Engineering, and Department of Chemistry for providing me with the necessary instrumental facilities.

I would like to thank Ministry of Human Resource Development, India and Indian Institute of Technology Guwahati for providing financial assistance during my Ph.D. tenure.

A heartfelt thanks to my lab mates and colleagues for providing me with a healthy and enjoyable research environment. I would also like to extend my heartfelt thanks to all my friends for being with me in my ups and downs and constantly motivating and encouraging me throughout this journey. It is a pleasure to thank all my teammates and opponents of cricket, badminton, and table tennis for providing me with beautiful memories to cherish.

Last but not least, my sincere thanks and appreciation goes to my parents and elder sister and brother for their selfless love, blessings, encouragement, patience, support and understandings throughout my studies. I thank my brother-in-law and sister-in-law for their constant support, patience, and encouragement throughout my Ph.D. journey.

Nirmal

Abstract

The demand for inexpensive, miniaturized, reliable, and portable sensors is ever increasing in the present time. In this regard, nanomaterial enabled sensors are considered promising candidates for numerous sensing applications due to their distinct physical and chemical attributes. The present thesis explores the salient features of nanomaterials by incorporating them in sensor technology for various applications. The thesis aims to develop affordable, compact, and robust nanomaterial enabled chemiresistive sensors for various sensing applications, including healthcare, food processing and agriculture, and environmental monitoring.

In this research work, various chemiresistive sensors have been developed by incorporating surface modified multiwall carbon nanotubes (MWCNTs) and metal based nanomaterial composite as the sensing material. In this regard, covalent and noncovalent functionalization techniques have been explored to attach suitable functional groups on the surface of MWCNTs for highly sensitive and selective applications. In one research work, the surface of MWCNTs has been modified with thiol functional groups for urea sensing applications in aqueous solution and raw milk samples. In another work, poly(diallyldimethylammonium chloride) solution (PDDA) has been attached to MWCNTs surface using a noncovalent functionalization approach to form MWCNT-PDDA composites. These MWCNT-PDDA composites have been explored for room temperature carbon monoxide gas sensing applications. A section of research has also demonstrated the synthesis of metal oxide heterojunction composite, where molybdenum disulfide-copper oxide (MoS_2-CuO) nanocomposite has been explored for acetone gas sensing application. A section of the research has also demonstrated the development of a paper based enzymatic chemiresistor for point-of-care (POC) detection of ethanol in human breath. The sensor is developed on a biodegradable paper substrate with alcohol dehydrogenase (ADH) modified MWCNT composite as the sensing material. In addition, the sensor is also integrated with an electronic circuit to develop proof-of-concept prototypes for the POC detection of ethanol in human breath.

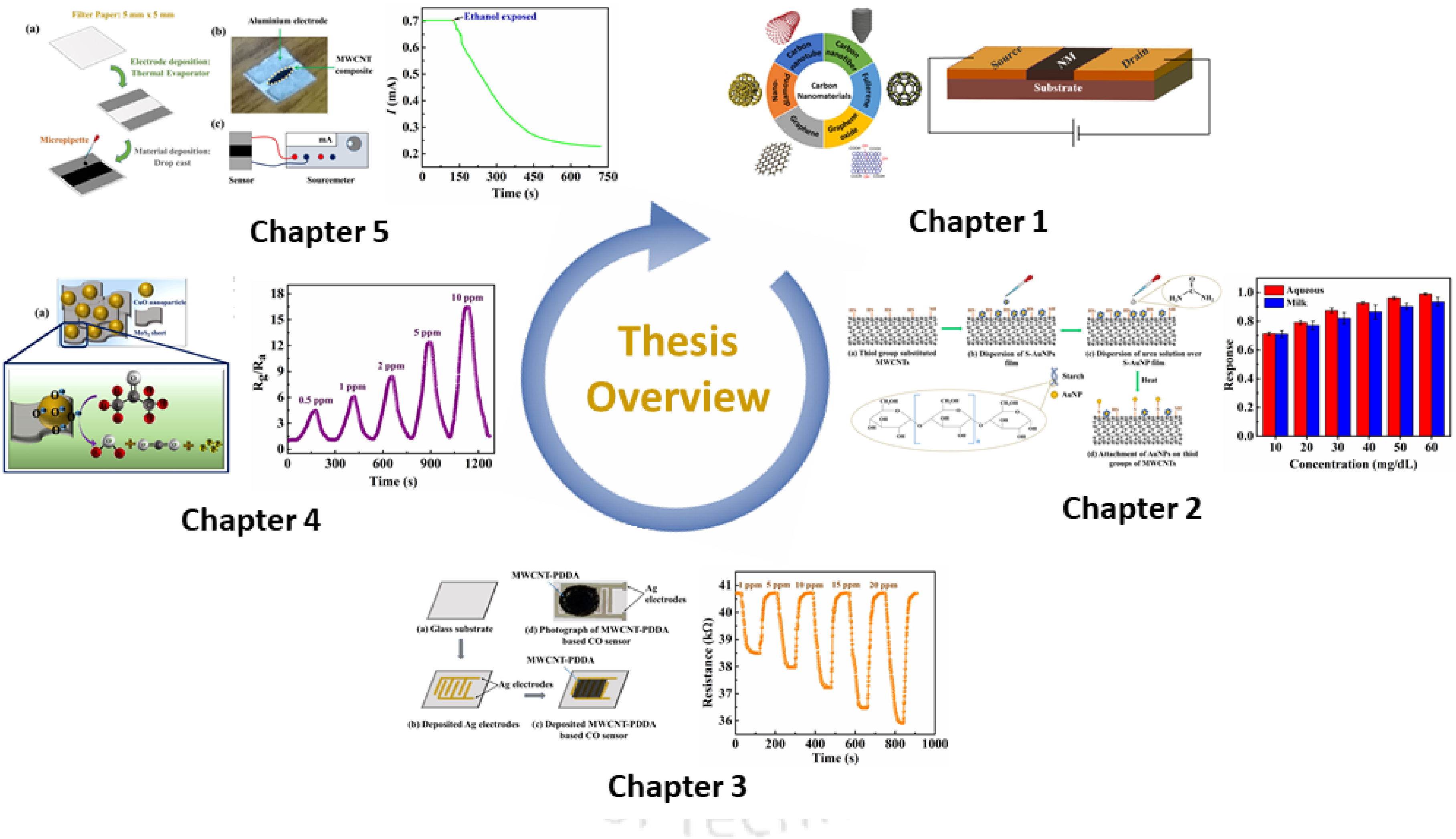
Thesis Overview
Chapter 1
Carbon Nanomaterials
Carbon nanotube
Carbon nanofiber
Fullerene
Graphene oxide
Graphene
Nano-diamond
Source
NM
Drain
Substrate
Chapter 2
(a) Thiol group substituted MWCNTs
(b) Dispersion of S-AuNPs film
(c) Dispersion of urea solution over S-AuNP film
(d) Attachment of AuNPs on thiol groups of MWCNTs
Starch
AuNP
Heat
Aqueous
Milk
Response
Concentration (mg/dL)
Chapter 3
(a) Glass substrate
(b) Deposited Ag electrodes
(c) Deposited MWCNT-PDDA based CO sensor
(d) Photograph of MWCNT-PDDA based CO sensor
MWCNT-PDDA
Ag electrodes
1 ppm
5 ppm
10 ppm
15 ppm
20 ppm
Resistance (kΩ)
Time (s)
Chapter 4
(a)
CuO nanoparticle
MoS₂ sheet
0.5 ppm
1 ppm
2 ppm
5 ppm
10 ppm
Rg/Ra
Time (s)
Chapter 5
Filter Paper: 5 mm x 5 mm
(a)
(b)
(c)
Electrode deposition: Thermal Evaporator
Micropipette
Material deposition: Drop cast
Aluminium electrode
MWCNT composite
Sensor
Sourcemeter
mA
Ethanol exposed
I (mA)
Time (s)

Contents

CHAPTER 1: Introduction

CHAPTER 2: Fabrication of a carbon nanotube based non-enzymatic sensor for urea detection in raw milk sample

CHAPTER 3: Development of a chemiresistor with surface modified carbon nanotubes for CO gas sensing application

CHAPTER 4: Synthesis of MoS_2-CuO nanocomposite for room temperature acetone gas sensing application

CHAPTER 5: Development of a paper based enzymatic chemiresistor for POC detection of ethanol in human breath

CHAPTER 6: Summary and Future scope

List of Figures

List of Tables

CHAPTER 1

Introduction

Contents

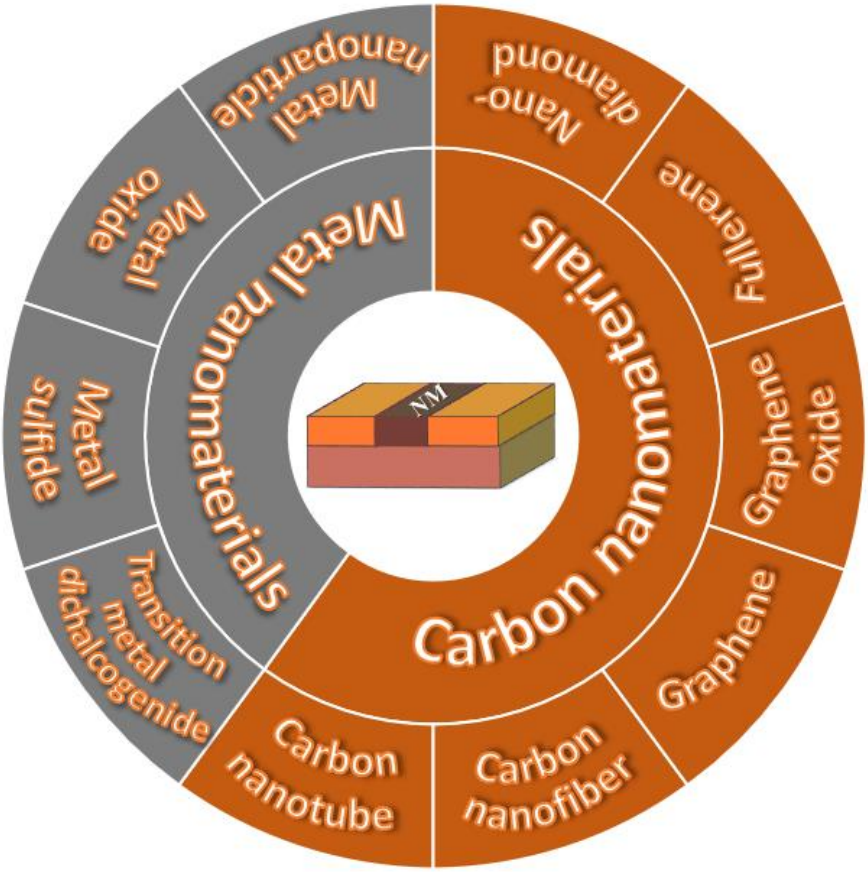
Metal nanomaterials
Carbon nanomaterials
NM
Metal nanoparticle
Metal oxide
Metal sulfide
Transition metal dichalcogenide
Nano-diamond
Fullerene
Graphene oxide
Graphene
Carbon nanofiber
Carbon nanotube

Abstract

The demand for sensing technologies providing miniaturization capability, ease of fabrication, high selectivity, cost-effectiveness, quick detection, high reliability, and easy portability is ever increasing in the present time. With rapid industrialization and urbanization, real-time monitoring of environmental pollutants has become one of the emerging areas of research across the globe as the excessive presence of environmental pollutants have a negative impact on the environment and human health. The integration of nanotechnology and material science with sensing technologies has broadened the scope of improvement in various sensing parameters for a wide range of applications. This chapter has focused on a detailed discussion about various nanomaterial enabled sensor architectures. A comprehensive discussion about various sensing nanomaterials has also been provided in this chapter. In context with the extensive discussion, this chapter identifies the knowledge gaps and presents the objectives of the thesis.

1.1 Overview

In recent years, the demands for sensor technologies have expanded enormously especially for applications in biomedical, chemical, food processing, environmental, and industrial safety. A sensor is a device that can respond to an external stimulus, which will change the conductance, capacitance, temperature, pressure, mass, or other properties of the sensing material and produce a recognizable signal. The key performance parameters of a sensor are sensitivity, selectivity, fast response, cost-effectiveness, stability, reproducibility, detection limit, and ease of fabrication [1–4]. Over the years, several sensor technologies such as electrical, electrochemical, microelectromechanical system (MEMS), and micro/nano-fluidics have been exploited by researchers and industrialists across the globe for various applications in the field of medical diagnostics, environmental monitoring, industrial safety etc. [5–9]. The present thesis aims to develop nanomaterials enabled chemiresistive sensors for various applications in healthcare, food processing and agriculture, and environmental monitoring.

In recent years, due to rapid urbanization and industrialization, the attention of the researchers across the globe has been attracted towards real-time monitoring of the excessive presence of environmental pollutants such as nitrogen monoxide (NO), carbon monoxide (CO), carbon dioxide (CO_2), nitrogen dioxide (NO_2), hydrogen sulfide (H_2S), ammonia (NH_3), methane (CH_4), sulfur dioxide (SO_2), and volatile organic compounds (VOCs) [10–20]. The excessive presence of environmental pollutants has negative effects on the environment and human health. Overexposure to environmental pollutants for a long period can lead to several health ailments related to nose, eye, liver, kidney, lung, central nervous systems and so on [21–24]. Recently, breath analysis is considered an emerging research area that enables rapid, cost-effective, simple, and non-invasive early-stage diagnosis of diseases. Human breath contains VOCs that include acetone (C_3H_6O), isoprene (C_5H_8), ethanol (C_2H_5OH), ethane (C_2H_6), methane (CH_4), pentane (C_5H_{12}), ammonia (NH_3), and hydrogen sulfide (H_2S) depending on abnormal metabolism or intoxications [25–33]. Thus, exhaled breath carries different biomarkers that enable early-stage diagnosis and help prevention of a broad range of diseases, including lung disorders, cancer, diabetes, gastrointestinal and liver diseases, and pathogen infections [34–39]. Thus, the need for affordable, rapid, reliable, portable, and point of care (POC) devices for real-time monitoring of health and environmental pollutants is of paramount importance. In this regard, nanomaterials have been considered promising candidates for sensing applications, including health and environmental monitoring, food safety, industrial safety etc.

The integration of nanotechnology and nanoscience with sensor technologies has boosted development of electrical sensors in numerous applications. In this regard, researchers have utilized the distinct physical and chemical attributes of nanomaterials and incorporated them with sensors for various applications, including biosensing, drug delivery, medicine, optoelectronic, microfluidics, energy storage, chemical and gas sensing [40–52]. Nanomaterials are those materials that present at least one dimension in nanometer scale and possess a high surface to volume ratio, quantum confinement, cost-effectiveness, superior catalytic activity, and unique electronic, mechanical, optical, magnetic or thermal properties [53–58]. Depending on the structural and dimensional evolution, nanomaterials can be classified as nanotubes, nanoparticles, nanofibers, nanorods, nanoflowers, nanosheets, nanoplates etc. [59–63]. Recently, a great deal of research is directed towards the miniaturization of nanomaterials based sensors, which can lead to low power consumption, compactness, less sensing materials, robustness, and cost-effectiveness. Integration of nanomaterials with sensors has opened up a large scope of development towards miniaturized devices for various sensing applications.

1.2 Classification of sensors

Recently, the demand for miniaturized, affordable, rapid, and reliable sensors for real-time health and environmental monitoring has increased. In this regard, nanomaterials enabled sensors have shown promising results for chemical and gas sensing applications. Sensor technologies can be classified into electrical, optical, gravimetric, or thermal, depending upon the method of transduction. Various types of sensors and the sub-categories are shown in Figure 1.1. Depending upon the device architecture, electrical sensors can be subdivided into chemiresistors, chemicapacitors and field effect transistors (FETs) based sensors. Optical sensors category can be divided into optical fiber, colorimetric, fluorescence, photoluminescence, and surface plasmon resonance (SPR) sensors. The gravimetric sensors can be sectioned into quartz crystal microbalance (QCM), surface acoustic wave (SAW) and microcantilever sensors [64–71]. The present thesis emphasizes the development of nanomaterial based electrical sensors for chemical and gas sensing applications.

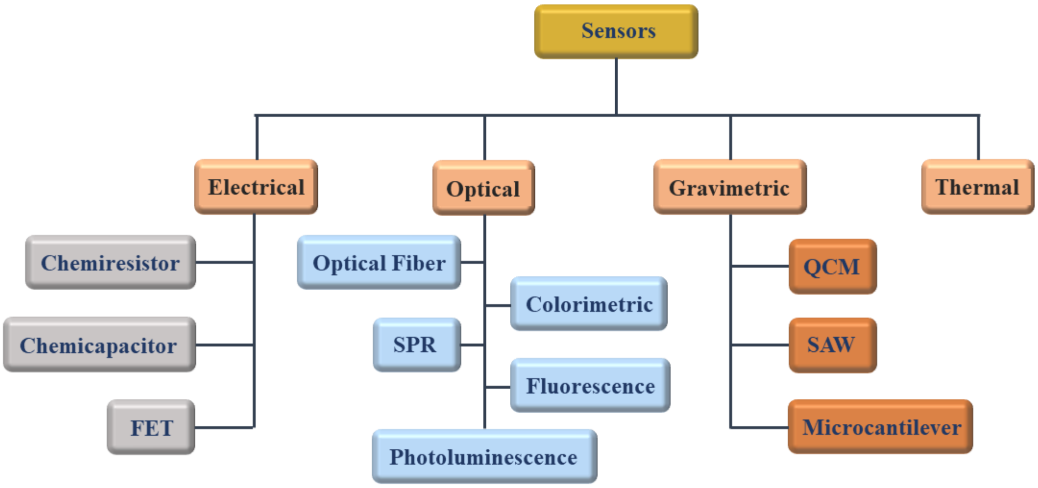

Figure 1.1: Various types of sensors and sub-categories.

1.2.1 Chemiresistor sensor

Chemiresistor sensor enabled with nanomaterials represents the simplest and common device architecture for numerous sensing applications. A chemiresistor consists of two metal electrodes (source and drain) on an insulating substrate (glass, silicon dioxide, plastic, paper) connected by nanomaterials (NM). The schematic diagram of a chemiresistor sensor device is shown in Figure 1.2. A chemiresistor sensor measures the variation of electrical resistance of the nanomaterial upon attachment or adsorption of target analytes on the surface of the nanomaterial. Depending on the variation of electrical resistance of the nanomaterial, target analytes can be detected quantitatively and qualitatively and the results can be represented in the form of various sensing parameters. The specificity of the chemiresistor sensor for a particular analyte can be achieved by incorporating suitable functional groups on the surface of the nanomaterial. Over the years, chemiresistor sensors have gathered tremendous attention due to their unique advantages such as simple structure, small size, ease of fabrication, low cost, robustness, and easy integration with electronic circuits for portable device applications [72–84].

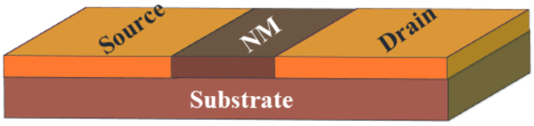

Figure 1.2: Schematic diagram of a simple chemiresistor sensor.

1.2.2 Chemicapacitor sensor

Chemicapacitor sensor is another device architecture of electrical sensors that consists of a dielectric layer and a nanomaterials (NM) layer sandwiched between two electrodes. The device architecture of the chemicapacitor sensor device is shown in Figure 1.3. The change in capacitance can also be analyte specific that enables detection of a particular analyte when it attaches to the surface of the nanomaterial. Different functional groups can be incorporated on the surface of the nanomaterial layer to increase the sensing performance of the chemicapacitor sensor. In recent years, chemicapacitor sensors have gained attention owing to their thermal stability, low power consumption, low cost, and high sensitivity [85–90]. Further, an AC field is used for measurements in chemicapacitors to reduce 1/f noise and ensure a rapid response. Moreover, electrophoretic effects from an applied directional voltage can also be avoided using an AC field that can reduce drift and enhance the reversibility of the chemicapacitor.

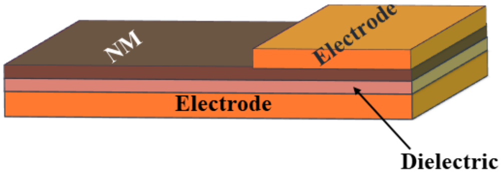

Figure 1.3: Device architecture of a chemicapacitor sensor.

1.2.3 Field effect transistor (FET) sensor

Field effect transistor (FET) device architecture is a three electrodes structure consists of the source, drain, and gate. The bottom gate configuration of the FET sensor is shown in Figure 1.4, where highly doped silicon is used as gate electrode and nanomaterials (NM) form the conducting channel between source and drain electrodes. The gate provides additional control of carrier densities of nanomaterials through modulation by applied gate voltage. Recently, nanomaterials are considered a potential candidate for sensing material in FET sensor for numerous sensing applications. In this regard, the nanomaterial surface is modified with a suitable functional group for sensing different target analytes. FET sensors have considerable applications due to their salient features such as high integration, mass production, miniaturization, high sensitivity, and tunable electrical properties [91–99].

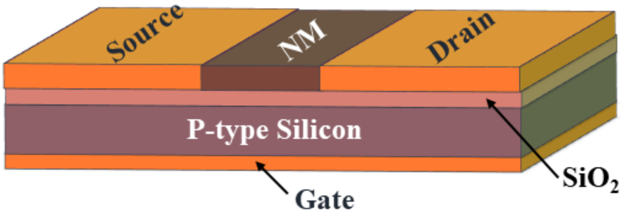

Figure 1.4: Schematic device architecture of a bottom gate FET sensor.

1.3 Classification of sensing nanomaterials

Over the past decade, researchers across the globe have extensively exploited the advantages of nanomaterials in the field of sensing and energy harvesting. A variety of nanomaterials based sensors have been developed for various sensing applications. In this section, a glimpse of various sensing nanomaterials has been presented.

1.3.1 Carbon nanomaterials

In recent years, carbon nanomaterials have been considered a promising candidate for nano-enabled devices for numerous sensing applications due to their fascinating electrical, chemical, and physical properties. Another significant advantage of carbon nanomaterials over its peers is the room temperature operation that enables carbon nanomaterial based sensors for portable sensing applications in the field of environmental, food and agriculture, and health monitoring. The most common carbon nanomaterials reported for various sensing applications include carbon nanotubes, carbon nanofibers, graphene, graphene oxide, nanodiamond, and fullerene [100–105]. Figure 1.5 presents various structures of carbon nanomaterials. For example, surface modified graphene and graphene oxide with nanoparticles and polymers have been proposed for numerous sensing applications [106–108]. Moreover, several works related to modified carbon nanofiber, nanodiamond, and fullerene have been reported for various sensing purposes in the field of healthcare, food and agriculture, chemical, and biosensing [109–112].

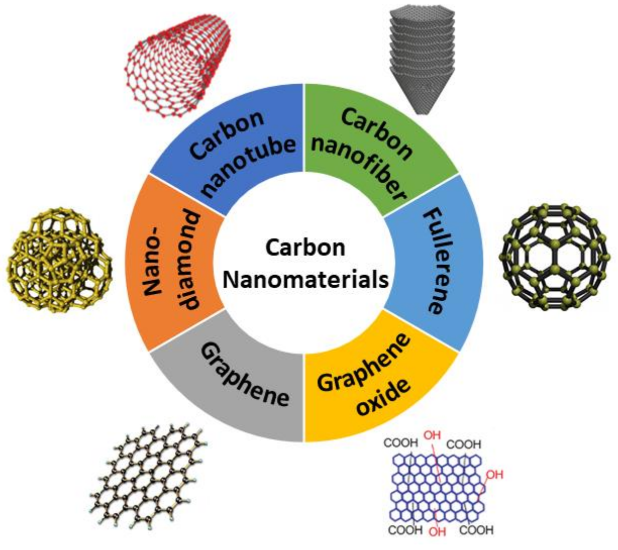

Figure 1.5: Various structures of carbon nanomaterials.

Among various carbon nanomaterials, carbon nanotube (CNT) has been able to grab attention as a sensing material owing to excellent electrical and mechanical properties, thermal stability, high surface to volume ratio, ease of fabrication, less toxicity, low power consumption, and so on [113–118]. CNTs are mainly categorized as single-walled carbon nanotube (SWCNT) and multi-walled carbon nanotube (MWCNT) depending on the number of graphene layers. In the CNT sensor, the electrical conductance of the nanotube changes upon exposure to the target analyte and produces a recognizable signal. The performance and selectivity of the CNT sensor can be improved by incorporating suitable functional groups on the CNT surface. The surface modification of the CNT has been reported through various techniques, including plasma treatment, low-pressure oxygen plasma treatment, for coating metal nanoparticles, conducting polymers, or polymeric composites, for the detection of NH_3, VOCs, H_2S, NO_2, CO, C_6H_6 or other gases [119–128]. For example, a wearable sensor has been developed by wrapping the surface of MWCNTs with polyvinyl alcohol, which showed a fast response and recovery time with higher selectivity and sensitivity towards ethanol vapors. The carboxyl functionalized MWCNT poly-(m-aminophenol) nanocomposite film and molecularly imprinted poly-(methyl methacrylate) on MWCNT have also been employed as effective sensor materials for the highly sensitive detection of various aliphatic alcohols [129, 130]. Further, SWCNTs have also been employed as the gate material in the field effect transistors for the measurement of alcoholic vapors [99]. Moreover, the performance and specificity of the sensor can also be drastically improved by incorporating suitable enzyme on CNT surface for various gas and biosensing applications [131–137]. For instance, biosensor based on conjugation of glucose oxidase have been demonstrated for enhanced glucose sensing applications [138, 139]. Similarly, urease enzyme has also been immobilized on the surface of MWCNTs for rapid urea detection [140]. In another example, cholesterol oxidase has been immobilized in carboxyl modified MWCNT surface for detection of cholesterol in human blood [141].

1.3.2 Metal based nanomaterials

Over the years, metal based nanomaterials are gaining much attention for various applications in medical and healthcare, environmental, chemical, and energy harvesting. Sensors using metal based nanomaterials possess faster response/recovery speed, higher sensitivity, better stability and reversibility, and they are cost-effective with simple fabrication processes compared to other sensing materials based sensor [142–148]. Metal based nanomaterials can be divided into four categories, including metal nanoparticles, metal oxides, metal sulfides, and transition metal dichalcogenides. Figure 1.6 shows classifications of various metal based nanomaterials and its subcategories.

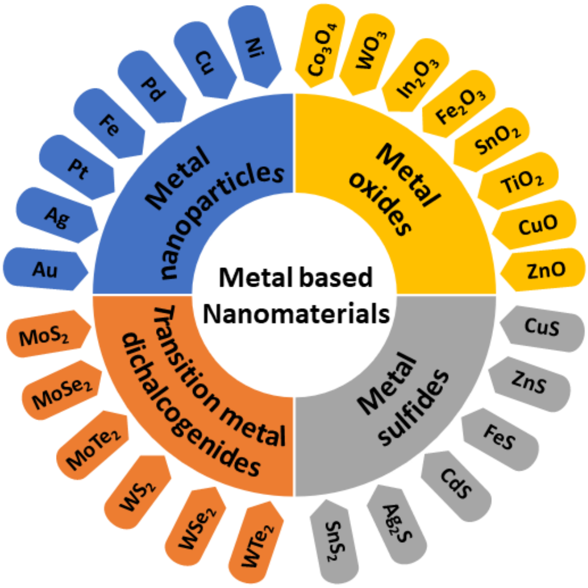

Figure 1.6: Classifications of metal based nanomaterials.

The combination of metal nanoparticles and chemical or biological molecules is very attractive and has gained great attention from researchers and industries for application specific sensor development. Over the years, several metal nanoparticles such as gold (Au), silver (Ag), platinum (Pt), iron (Fe), palladium (Pd), copper (Cu), and nickel (Ni) are reported in various chemical and biosensing applications [149–157]. For instance, Au and Ag nanoparticles have been widely used in various biomedical and sensing applications such as drug delivery and cancer treatment, antibacterial and antifungal activity, peroxides and glucose sensing and so on [158–161]. Moreover, several works have been reported on Pt and Pd nanoparticle based sensors for various applications in the field of medical, food, and agriculture [162–164].

The other category of metal based nanomaterials includes metal sulfides, which is a kind of combination of sulfur anions and metal/semi-metal cations in the form of M_xS_y ($x : y = 1 : 1, 1 : 2, 2 : 1, 3 : 4$). The tunable bandgaps of metal sulfides are suitable for transistor applications in addition to their excellent sensing performance [165–167]. In this regard, various metal sulfides such as copper sulfide (CuS), zinc sulfide (ZnS), iron sulfide (FeS), cadmium sulfide (CdS), silver sulfide (Ag_2S), and tin sulfide (SnS_2) have been extensively used for several sensing applications [168–175]. For example, ZnS nanowire and SnS_2 nanorods have been demonstrated as sensing material for acetone gas sensing application [176, 177]. In another example, CdS thin film and hollow sphere CuS have been reported for ethanol detection [178, 179]. Moreover, heterojunction of metal sulfide such as SnS_2/ZnS has also been proposed for ammonia gas sensing application [180].

Over the years, metal oxide based sensors have been broadly used in various gas sensing applications due to their outstanding physical and chemical properties, cost effectiveness, wide bandgap, and simple preparation method. Moreover, the surface of metal oxide has strong adsorption characteristics and high reactivity towards target gas due to the availability of large number of free electrons on the conduction band and oxygen vacancies on metal oxide surface [181–185]. Several metal oxide nanomaterials such as zinc oxide (ZnO), copper oxide (CuO), titanium dioxide (TiO_2), tin oxide (SnO_2), iron oxide (Fe_2O_3), indium oxide (In_2O_3), tungsten trioxide (WO_3), and cobalt oxide (Co_3O_4) have been reported for various sensing applications [186–197]. For example, different morphologies of ZnO such as nanowires, nanorods, nanofibers, nanosheets, and nanoparticles have been explored for various gas sensing applications, including ammonia, nitric oxide, methane, acetone, ethanol, and carbon monoxide [198–203]. In another example, TiO_2 nanotube, CuO nanowire, and CuO nanosheet have also been proposed for ethanol gas sensing application [204, 205]. Moreover, nanoparticle doped metal oxides such as Nb-doped TiO_2, F-doped SnO_2, and Al-doped TiO_2 have also been demonstrated for various gas sensing applications [206–208].

The other category of metal based nanomaterials includes transition metal dichalcogenides, which are semiconductors of type MX_2, where M denotes transition metal atom (Mo or W) and X denotes chalcogen atom (S, Se or Te). In this regard, various transition metal dichalcogenides, including molybdenum disulfide (MoS_2), molybdenum diselenide ($MoSe_2$), molybdenum ditelluride ($MoTe_2$), tungsten disulfide (WS_2), tungsten diselenide (WSe_2), and tungsten ditelluride ($MoTe_2$) have been reported for various sensing applications [209–214].

Among several metal oxide nanomaterials, copper oxide (CuO) is widely used in various gas sensing applications. CuO is a p-type semiconductor with excellent active gas sensing properties such as ease of access, good stability, and high catalytic activity towards a wide range of oxidation and reduction reactions. Moreover, p-type metal oxide nanomaterials provide the scope of formation of p-n junctions, which can be used for selective gas sensing applications [215–220]. Molybdenum disulfide (MoS_2) is a typical transition metal dichalcogenides with n-type semiconducting behaviors and exhibit excellent properties such as high mobility, high surface to mass ratio, tunable bandgap, nontoxic, excellent mechanical strength and so on [221–225]. Recently, hybrids of metal oxide and transition metal dichalcogenides as sensing material are attracting the academics across the globe for various applications, including electronic devices, energy storage, biosensing, gas and chemical sensing, and so on [226–234].

1.4 Knowledge gap

In the context of previous discussion, although several works have been reported on nanomaterial based sensors, only few literature have shown gas sensing application at room temperature. Further, sensors based on pristine nanomaterial usually exhibit low sensitivity, poor selectivity, slow response and recovery, and require high operating temperature. The room temperature operation of a sensor provides the platform for easy integration of electronic circuits for miniaturized devices in portable applications. The surface of the nanomaterial can be incorporated with suitable functional group/enzyme for highly selective and sensitive detection of target analytes. Moreover, analytical techniques have been extensively explored for chemical and gas sensing, however these analytical techniques are time-consuming, expensive, complex sample collection, need pre-possessing of samples, and require expertise in performing the experiment. With this knowledge gap, the objectives of the thesis are designed based on chemiresistive devices and discussed in the subsequent sections.

1.5 Objective of the Thesis

The main objective of the thesis is the development of nanomaterial enabled electrical sensors for healthcare, food processing and agriculture, and environmental monitoring applications. For the development of electrical sensor, chemiresistive device architecture has been explored with various nanomaterials as sensing platform. The present thesis demonstrates the development of affordable chemiresistor sensors for various chemical and gas sensing applications. The objectives of the present thesis are as follows:

- Fabrication of a carbon nanotube based non-enzymatic sensor for urea detection in raw milk sample.
- Development of a chemiresistor with surface modified carbon nanotubes for CO gas sensing application.
- Synthesis of MoS_2-CuO nanocomposite for room temperature acetone gas sensing application.
- Development of a paper based enzymatic chemiresistor for POC detection of ethanol in human breath.

1.6 Organization of the Thesis

The complete thesis work is presented in six chapters. **Chapter 1** starts with the introduction, providing a brief overview of sensor technologies, sensor architectures, and various sensing nanomaterials, followed by the objectives of the present thesis.

Subsequently, four technical chapters are presented. **Chapter 2** presents the development of a non-enzymatic urea sensor based on MWCNT nanocomposite. The thiol functional group (SH) is attached on the surface of MWCNT for the preparation of sensing material. The sensing performance of the sensor has been examined for various urea concentrations, and a probable sensing mechanism is proposed. Further, the sensor has been used to detect urea concentrations in raw milk samples to evaluate practical applicability. **Chapter 3** demonstrates the development of a room temperature CO gas sensor based on MWCNT-PDDA composite. Here, the surface of MWCNTs has been modified with poly(diallyldimethylammonium chloride) solution (PDDA). The sensing performance of the MWCNT-PDDA composite has been explored for CO gas, and a probable sensing mechanism is proposed. **Chapter 4**, demonstrates room temperature acetone gas sensing based on MoS_2-CuO nanocomposite. The gas sensing performance of MoS_2-CuO nanocomposite has been evaluated by exposing the sensor to various acetone concentrations and interfering gases. The probable sensing mechanism of the sensor has been discussed in detail. **Chapter 5** demonstrates a paper based enzymatic chemiresistor for POC detection of ethanol in human breath. The sensor is developed on a biodegradable paper substrate with alcohol dehydrogenase (ADH) modified MWCNT composite as the sensing material. The sensor is exposed to various ethanol concentrations and other VOC gases, and the performance of the sensor has been evaluated. The sensor is integrated with an electronic circuit to develop proof-of-concept prototypes for the POC detection of ethanol in human breath. **Chapter 6** presents the summary of the significant findings and important conclusions of the present thesis and future scope of work. A brief detail of outcomes of this thesis in terms of patents, publications, and conferences has also been provided at the end of the thesis. The flowchart for the organization of the thesis is shown in Figure 1.7.

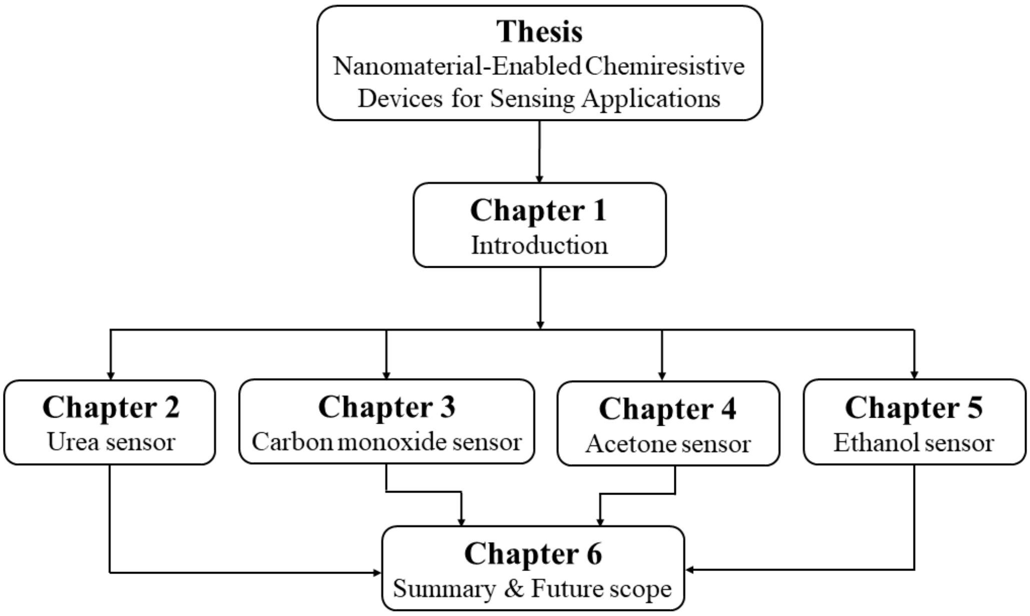

Figure 1.7: Flowchart for the organization of the thesis.

References

[1] J. F. Fennell Jr, S. F. Liu, J. M. Azzarelli, J. G. Weis, S. Rochat, K. A. Mirica, J. B. Ravnsbæk, and T. M. Swager, *Angew. Chem., Int. Ed.*, 55 (4), 1266-1281, 2016.

[2] V. D. N. Bezzon, T. L. A. Montanheiro, B. R. C. de Menezes, R. G. Ribas, V. A. N. Righetti, K. F. Rodrigues, and G. P. Thim, *Adv. Mater. Sci. Eng.*, 2019, 4293073, 2019.

[3] S. Mehdi Aghaei, M. M. Monshi, I. Torres, S. M. J. Zeidi, and I. Calizo, *Appl. Surf. Sci.*, 427, 326-333, 2018.

[4] P. Bindra and A. Hazra, *J. Mater. Sci.: Mater. Electron.*, 29 (8), 6129-6148, 2018.

[5] W. Pang, H. Zhao, E. S. Kim, H. Zhang, H. Yu, and X. Hu, *Lab Chip*, 12 (1), 29-44, 2012.

[6] S. M. Majhi, A. Mirzaei, H. W. Kim, S. S. Kim, and T. W. Kim, *Nano Energy*, 79, 105369, 2021.

[7] D. W. Kimmel, G. LeBlanc, M. E. Meschievitz, and D. E. Cliffel, *Anal. Chem.*, 84 (2), 685-707, 2012.

[8] S. G. Surya, S. Bhanoth, S. M. Majhi, Y. D. More, V. M. Teja, and K. N. Chappanda, *CrystEngComm*, 21 (47), 7303-7312, 2019.

[9] Y. Song, J. Zhang, and D. Li, *Micromachines (Basel)*, 8 (7), 204, 2017.

[10] A. Afroozeh, E. Akbari, and P. Yupapin, *J. Nanoelectron. Optoelectron.*, 14 (9), 1225-1229, 2019.

[11] H. Tang, L. N. Sacco, S. Vollebregt, H. Ye, X. Fan, and G. Zhang, *J. Mater. Chem. A*, 8 (47), 24943-24976, 2020.

[12] N. Roy, R. Sinha, T. T. Daniel, H. B. Nemade, and T. K. Mandal, *IEEE Sens. J.*, 20 (22), 13245-13252, 2020.

[13] R. Li, H. Qi, Y. Ma, Y. Deng, S. Liu, Y. Jie, J. Jing, J. He, X. Zhang, L. Wheatley, C. Huang, X. Sheng, M. Zhang, and L. Yin, *Nat. Commun.*, 11 (1), 3207, 2020.

[14] Y. Wu, M. Yan, C. Tian, Y. Liu, and Z. Hua, *Front. Chem.*, 7 (907), 2020.

[15] Z. Li, N. Wang, Z. Lin, J. Wang, W. Liu, K. Sun, Y. Q. Fu, and Z. Wang, *ACS Appl. Mater. Interfaces*, 8 (32), 20962-20968, 2016.

[16] N. Ingle, S. Mane, P. Sayyad, G. Bodkhe, T. AL-Gahouari, M. Mahadik, S. Shirsat, and M. D. Shirsat, *Front. Mater.*, 7 (93), 2020.

[17] J. Gębicki, A. Kloskowski, and W. Chrzanowski, *Sens. Actuators, B*, 177, 1173-1179, 2013.

[18] X. Wang, S. Hou, H. Goktas, P. Kovacik, F. Yaul, A. Paidimarri, N. Ickes, A. Chandrakasan, and K. Gleason, *ACS Appl. Mater. Interfaces*, 7 (30), 16213-16222, 2015.

[19] Y. Chen, H. Zhang, Z. Feng, H. Zhang, R. Zhang, Y. Yu, J. Tao, H. Zhao, W. Guo, W. Pang, X. Duan, J. Liu, and D. Zhang, *ACS Appl. Mater. Interfaces*, 8 (33), 21742-21749, 2016.

[20] M. Penza, G. Cassano, P. Aversa, A. Cusano, M. Consales, M. Giordano, and L. Nicolais, *IEEE Sens. J.*, 6 (4), 867-875, 2006.

[21] G. de Gennaro, G. Farella, A. Marzocca, A. Mazzone, and M. Tutino, *Int. J. Environ. Res. Public Health*, 10 (12), 6273-6291, 2013.

[22] N. Roy, S. Mitra, N. M. Das, N. Mandal, D. Bandyopadhyay, H. B. Nemade, and T. K. Mandal, *IEEE Sens. J.*, 20 (5), 2278-2286, 2020.

[23] X. Zhu, H. Zhang, and J. Wu, *Sens. Actuators, B,* 202, 105-113, 2014.

[24] T. Endo, Y. Yanagida, and T. Hatsuzawa, *Sens. Actuators, B,* 125 (2), 589-595, 2007.

[25] M. Bhattacharjee, H. B. Nemade, and D. Bandyopadhyay, *Biosens. Bioelectron.*, 94, 544-551, 2017.

[26] O. Lawal, W. M. Ahmed, T. M. E. Nijsen, R. Goodacre, and S. J. Fowler, *Metabolomics,* 13 (10), 110-110, 2017.

[27] E. Bihar, Y. Deng, T. Miyake, M. Saadaoui, G. G. Malliaras, and M. Rolandi, *Sci. Rep.*, 6, 27582-27582, 2016.

[28] P. J. Mazzone, *J. Thorac. Oncol.*, 3 (7), 774-780, 2008.

[29] R. Schnabel, R. Fijten, A. Smolinska, J. Dallinga, M.-L. Boumans, E. Stobberingh, A. Boots, P. Roekaerts, D. Bergmans, and F. J. van Schooten, *Sci. Rep.*, 5 (1), 17179, 2015.

[30] K. H. Kim, S. A. Jahan, and E. Kabir, *TrAC, Trends Anal. Chem.*, 33, 1-8, 2012.

[31] S. Das and M. Pal, *J. Electrochem. Soc.*, 167 (3), 037562, 2020.

[32] E. Kabir, N. Raza, V. Kumar, J. Singh, Y. F. Tsang, D. K. Lim, J. E. Szulejko, and K.-H. Kim, *Chem*, 5 (12), 3020-3057, 2019.

[33] J.-E. Chang, D.-S. Lee, S.-W. Ban, J. Oh, M. Y. Jung, S.-H. Kim, S. Park, K. Persaud, and S. Jheon, *Sens. Actuators, B,* 255, 800-807, 2018.

[34] S. T. Chambers, A. Scott-Thomas, and M. Epton, *Curr Opin Pulm Med,* 18 (3), 228-32, 2012.

[35] C. S. Probert, I. Ahmed, T. Khalid, E. Johnson, S. Smith, and N. Ratcliffe, *J Gastrointestin Liver Dis,* 18 (3), 337-43, 2009.

[36] M. Phillips, R. N. Cataneo, T. Cheema, and J. Greenberg, *Clin Chim Acta,* 344 (1-2), 189-94, 2004.

[37] M. Hakim, Y. Y. Broza, O. Barash, N. Peled, M. Phillips, A. Amann, and H. Haick, *Chem Rev*, 112 (11), 5949-66, 2012.

[38] A. W. Boots, J. J. van Berkel, J. W. Dallinga, A. Smolinska, E. F. Wouters, and F. J. van Schooten, *J Breath Res*, 6 (2), 027108, 2012.

[39] S. Sethi, R. Nanda, and T. Chakraborty, *Clin Microbiol Rev*, 26 (3), 462-475, 2013.

[40] Y. Zhou, M. Zhang, Z. Guo, L. Miao, S.-T. Han, Z. Wang, X. Zhang, H. Zhang, and Z. Peng, *Mater. Horiz.*, 4 (6), 997-1019, 2017.

[41] W. Tao, X. Ji, X. Zhu, L. Li, J. Wang, Y. Zhang, P. E. Saw, W. Li, N. Kong, M. A. Islam, T. Gan, X. Zeng, H. Zhang, M. Mahmoudi, G. J. Tearney, and O. C. Farokhzad, *Adv. Mater.*, 30 (38), 1802061, 2018.

[42] S. Zhang, S. Guo, Z. Chen, Y. Wang, H. Gao, J. Gómez-Herrero, P. Ares, F. Zamora, Z. Zhu, and H. Zeng, *Chem. Soc. Rev.*, 47 (3), 982-1021, 2018.

[43] S. Venkateshalu and A. N. Grace, *Appl. Mater. Today*, 18, 100509, 2020.

[44] S. Park, M. Vosguerichian, and Z. Bao, *Nanoscale*, 5 (5), 1727-1752, 2013.

[45] G. Aragay, J. Pons, and A. Merkoçi, *Chem. Rev.*, 111 (5), 3433-3458, 2011.

[46] E. Duguet, S. Vasseur, S. Mornet, and J. M. Devoisselle, *Nanomedicine (Lond)*, 1 (2), 157-68, 2006.

[47] M. Xie, S. Zhang, B. Cai, Y. Gu, X. Liu, E. Kan, and H. Zeng, *Nano Energy*, 38, 561-568, 2017.

[48] W. Liu, X. Zhou, L. Xu, S. Zhu, S. Yang, X. Chen, B. Dong, X. Bai, G. Lu, and H. Song, *Nanoscale*, 11 (24), 11496-11504, 2019.

[49] Y. Y. Broza and H. Haick, *Nanomedicine*, 8 (5), 785-806, 2013.

[50] R. Jayakumar, D. Menon, K. Manzoor, S. V. Nair, and H. Tamura, *Carbohydr. Polym.*, 82 (2), 227-232, 2010.

[51] J. Wang, *Electroanalysis*, 17 (1), 7-14, 2005.

[52] Y. Song, J. Hormes, and C. S. S. R. Kumar, *Small*, 4 (6), 698-711, 2008.

[53] K. Khoshnevisan, H. Maleki, E. Honarvarfard, H. Baharifar, M. Gholami, F. Faridbod, B. Larijani, R. Faridi Majidi, and M. R. Khorramizadeh, *Microchim. Acta*, 186 (1), 49, 2019.

[54] A. A. Yaqoob, T. Parveen, K. Umar, and M. N. Mohamad Ibrahim, *Water*, 12 (2), 2020.

[55] A. A. Yaqoob, H. Ahmad, T. Parveen, A. Ahmad, M. Oves, I. M. I. Ismail, H. A. Qari, K. Umar, and M. N. Mohamad Ibrahim, *Front. Chem.*, 8 (341), 2020.

[56] W. G. Kreyling, M. Semmler-Behnke, and Q. Chaudhry, *Nano Today*, 5 (3), 165-168, 2010.

[57] Y. Shen, W. Wang, A. Fan, D. Wei, W. Liu, C. Han, Y. Shen, D. Meng, and X. San, *Int. J. Hydrogen Energy*, 40 (45), 15773-15779, 2015.

[58] F. Yavari and N. Koratkar, *J. Phys. Chem. Lett.*, 3 (13), 1746-1753, 2012.

[59] K. Shrivas, A. Ghosale, P. K. Bajpai, T. Kant, K. Dewangan, and R. Shankar, *Microchem. J.*, 156, 104944, 2020.

[60] Q. Wang, M. Safdar, K. Xu, M. Mirza, Z. Wang, and J. He, *ACS Nano*, 8 (7), 7497-7505, 2014.

[61] J. Chen, Y. Dai, Y. Ma, X. Dai, W. Ho, and M. Xie, *Nanoscale*, 9 (41), 15945-15948, 2017.

[62] C. D. Brown, D. M. Cruz, A. K. Roy, and T. J. Webster, *J. Nanopart. Res.*, 20 (9), 254, 2018.

[63] K. Schwirn, L. Tietjen, and I. Beer, *Environ. Sci. Eur.*, 26 (1), 4, 2014.

[64] Y. Okahata, K. Matsuura, K. Ito, and Y. Ebara, *Langmuir*, 12 (4), 1023-1026, 1996.

[65] U. Latif, A. Rohrer, P. A. Lieberzeit, and F. L. Dickert, *Anal Bioanal Chem*, 400 (8), 2457-62, 2011.

[66] X. C. Zhou, L. Zhong, S. F. Y. Li, S. C. Ng, and H. S. O. Chan, *Sens. Actuators, B*, 42 (1), 59-65, 1997.

[67] M. J. Fernández, J. L. Fontecha, I. Sayago, M. Aleixandre, J. Lozano, J. Gutiérrez, I. Gràcia, C. Cané, and M. d. C. Horrillo, *Sens. Actuators, B*, 127 (1), 277-283, 2007.

[68] D. Sil, J. Hines, U. Udeoyo, and E. Borguet, *ACS Appl. Mater. Interfaces*, 7 (10), 5709-5714, 2015.

[69] A. Afzal, N. Iqbal, A. Mujahid, and R. Schirhagl, *Anal. Chim. Acta*, 787, 36-49, 2013.

[70] A. Bietsch, J. Zhang, M. Hegner, H. P. Lang, and C. Gerber, *Nanotechnology*, 15 (8), 873-880, 2004.

[71] Y. K. Yoo, M.-S. Chae, J. Y. Kang, T. S. Kim, K. S. Hwang, and J. H. Lee, *Anal. Chem.*, 84 (19), 8240-8245, 2012.

[72] V. Schroeder, S. Savagatrup, M. He, S. Lin, and T. M. Swager, *Chem. Rev.*, 119 (1), 599-663, 2019.

[73] A. Mirzaei, J.-H. Lee, S. M. Majhi, M. Weber, M. Bechelany, H. W. Kim, and S. S. Kim, *J. Appl. Phys.*, 126 (24), 241102, 2019.

[74] S. Sharma, S. Hussain, S. Singh, and S. S. Islam, *Sens. Actuators, B*, 194, 213-219, 2014.

[75] T. Sarkar, S. Srinives, S. Sarkar, R. C. Haddon, and A. Mulchandani, *J. Phys. Chem. C*, 118 (3), 1602-1610, 2014.

[76] Y. Zhang, M. Xu, B. R. Bunes, N. Wu, D. E. Gross, J. S. Moore, and L. Zang, *ACS Appl. Mater. Interfaces*, 7 (14), 7471-7475, 2015.

[77] S. Mahajan and S. Jagtap, *J. Electron. Mater.*, 50 (5), 2531-2555, 2021.

[78] C. Parameswaran and D. Gupta, *Nano Convergence*, 6 (1), 28, 2019.

[79] J. Pan, S. Liu, Y. Yang, and J. Lu, *Nanomaterials*, 8 (6), 2018.

[80] M. Y. Rezk, J. Sharma, and M. R. Gartia, *Nanomaterials*, 10 (11), 2020.

[81] H. Schlicke, M. Rebber, S. Kunze, and T. Vossmeyer, *Nanoscale*, 8 (1), 183-186, 2016.

[82] S. S. Barkade, J. B. Naik, and S. H. Sonawane, *Colloids Surf., A,* 378 (1), 94-98, 2011.

[83] J. Im, S. K. Sengupta, M. F. Baruch, C. D. Granz, S. Ammu, S. K. Manohar, and J. E. Whitten, *Sens. Actuators, B,* 156 (2), 715-722, 2011.

[84] M. De Wit, E. Vanneste, H. J. Geise, and L. J. Nagels, *Sens. Actuators, B,* 50 (2), 164-172, 1998.

[85] H. Taghinejad, M. Taghinejad, M. Abdolahad, A. Saeidi, and S. Mohajerzadeh, *Sens. Actuators, B,* 176, 413-419, 2013.

[86] A. M. Kummer, A. Hierlemann, and H. Baltes, *Anal. Chem.,* 76 (9), 2470-2477, 2004.

[87] T. Ishihara and S. Matsubara, *J. Electroceram.,* 2 (4), 215-228, 1998.

[88] S. Homayoonnia and S. Zeinali, *Sens. Actuators, B,* 237, 776-786, 2016.

[89] T. Ishihara, S. Sato, T. Fukushima, and Y. Takita, *J. Electrochem. Soc.*, 143 (6), 1908-1914, 1996.

[90] M. Agarwal, M. D. Balachandran, S. Shrestha, and K. Varahramyan, *J. Nanomater.*, 2012, 145406, 2012.

[91] A. Nehra and K. Pal Singh, *Biosens. Bioelectron.*, 74, 731-743, 2015.

[92] K. Lee, P. R. Nair, A. Scott, M. A. Alam, and D. B. Janes, *J. Appl. Phys.*, 105 (10), 102046, 2009.

[93] S. Liu and X. Guo, *NPG Asia Mater.*, 4 (8), e23-e23, 2012.

[94] B. L. Allen, P. D. Kichambare, and A. Star, *Adv. Mater.*, 19 (11), 1439-1451, 2007.

[95] L. Syedmoradi, A. Ahmadi, M. L. Norton, and K. Omidfar, *Microchim. Acta*, 186 (11), 739, 2019.

[96] S. Mao, J. Chang, H. Pu, G. Lu, Q. He, H. Zhang, and J. Chen, *Chem. Soc. Rev.*, 46 (22), 6872-6904, 2017.

[97] Y.-W. Cho, J.-H. Park, K.-H. Lee, T. Lee, Z. Luo, and T.-H. Kim, *Nano Convergence*, 7 (1), 40, 2020.

[98] M. Sedki, Y. Shen, and A. Mulchandani, *Biosens. Bioelectron.*, 176, 112941, 2021.

[99] T. Someya, J. Small, P. Kim, C. Nuckolls, and J. T. Yardley, *Nano Lett.*, 3 (7), 877-881, 2003.

[100] B. T. Zhang, X. Zheng, H. F. Li, and J. M. Lin, *Anal Chim Acta*, 784 1-17, 2013.

[101] D. Yadav, F. Amini, and A. Ehrmann, *Eur. Polym. J.*, 138, 109963, 2020.

[102] W.-T. Koo, H.-J. Cho, D.-H. Kim, Y. H. Kim, H. Shin, R. M. Penner, and I.-D. Kim, *ACS Nano*, 14 (11), 14284-14322, 2020.

[103] K. D. Patel, R. K. Singh, and H.-W. Kim, *Mater. Horiz.*, 6 (3), 434-469, 2019.

[104] K. S. Novoselov, V. I. Fal′ko, L. Colombo, P. R. Gellert, M. G. Schwab, and K. Kim, *Nature*, 490 (7419), 192-200, 2012.

[105] L.-M. Peng, Z. Zhang, and S. Wang, *Mater. Today*, 17 (9), 433-442, 2014.

[106] E. Morales-Narváez, L. Baptista-Pires, A. Zamora-Gálvez, and A. Merkoçi, *Adv. Mater.*, 29 (7), 1604905, 2017.

[107] B. C. Janegitz, T. A. Silva, A. Wong, L. Ribovski, F. C. Vicentini, M. d. P. Taboada Sotomayor, and O. Fatibello-Filho, *Biosens. Bioelectron.*, 89, 224-233, 2017.

[108] N. Chauhan, T. Maekawa, and D. N. S. Kumar, *J. Mater. Res.*, 32 (15), 2860-2882, 2017.

[109] J. Horne, L. McLoughlin, B. Bridgers, and E. K. Wujcik, *Sens. Actuators Rep.*, 2 (1), 100005, 2020.

[110] W. Zeng, L. Shu, Q. Li, S. Chen, F. Wang, and X.-M. Tao, *Adv. Mater.*, 26 (31), 5310-5336, 2014.

[111] S. Pilehvar and K. De Wael, *Biosensors (Basel)*, 5 (4), 712-735, 2015.

[112] N. Bondon, L. Raehm, C. Charnay, R. Boukherroub, and J.-O. Durand, *J. Mater. Chem. B*, 8 (48), 10878-10896, 2020.

[113] R. Tang, Y. Shi, Z. Hou, and L. Wei, *Sensors*, 17 (4), 882, 2017.

[114] J.-F. Feller, N. Gatt, B. Kumar, and M. Castro, *Chemosensors*, 2 (1), 26-40, 2014.

[115] S. Abdulla, T. L. Mathew, and B. Pullithadathil, *Sens. Actuators, B*, 221, 1523-1534, 2015.

[116] C.-M. Tîlmaciu and M. C. Morris, *Front. Chem.*, 3, 59-59, 2015.

[117] Y. Zhou, Y. Fang, and R. P. Ramasamy, *Sensors*, 19 (2), 2019.

[118] J. W. Mintmire and C. T. White, *Carbon*, 33 (7), 893-902, 1995.

[119] C. Chen, A. Ogino, X. Wang, and M. Nagatsu, *Appl. Phys. Lett.*, 96 (13), 131504, 2010.

[120] D. W. H. Fam, A. I. Y. Tok, A. Palaniappan, P. Nopphawan, A. Lohani, and S. G. Mhaisalkar, *Sens. Actuators, B*, 138 (1), 189-192, 2009.

[121] E. H. Espinosa, R. Ionescu, C. Bittencourt, A. Felten, R. Erni, G. Van Tendeloo, J. J. Pireaux, and E. Llobet, *Thin Solid Films*, 515 (23), 8322-8327, 2007.

[122] S. Middya, M. Bhattacharjee, and D. Bandyopadhyay, *Nanotechnology*, 30 (14), 145502, 2019.

[123] Z. Zanolli, R. Leghrib, A. Felten, J.-J. Pireaux, E. Llobet, and J.-C. Charlier, *ACS Nano*, 5 (6), 4592-4599, 2011.

[124] D. Maity, K. Rajavel, and R. T. R. Kumar, *Sens. Actuators, B*, 261, 297-306, 2018.

[125] C.-K. Liu, J.-M. Wu, and H. C. Shih, *Sens. Actuators, B*, 150 (2), 641-648, 2010.

[126] C.-T. Hu, C.-K. Liu, M.-W. Huang, S.-H. Syue, J.-M. Wu, Y.-s. Chang, J.-W. Yeh, and H.-C. Shih, *Diamond Relat. Mater.*, 18 (2), 472-477, 2009.

[127] M. Penza, M. A. Tagliente, P. Aversa, and G. Cassano, *Chem. Phys. Lett.*, 409 (4), 349-354, 2005.

[128] J. K. Abraham, B. Philip, A. Witchurch, V. K. Varadan, and C. C. Reddy, *Smart Mater. Struct.*, 13 (5), 1045-1049, 2004.

[129] S. K. Verma, P. Kar, D. J. Yang, and A. Choudhury, *Sens. Actuators, B*, 219, 199-208, 2015.

[130] T. Alizadeh and F. Rezaloo, *Sens. Actuators, B*, 176, 28-37, 2013.

[131] M. Sireesha, V. Jagadeesh Babu, A. S. Kranthi Kiran, and S. Ramakrishna, *Nanocomposites*, 4 (2), 36-57, 2018.

[132] M. Zhang, A. Smith, and W. Gorski, *Anal. Chem.*, 76 (17), 5045-5050, 2004.

[133] K. Balasubramanian and M. Burghard, *Anal. Bioanal. Chem.*, 385 (3), 452-468, 2006.

[134] V. Biju, *Chem Soc Rev*, 43 (3), 744-64, 2014.

[135] D. Pantarotto, R. Singh, D. McCarthy, M. Erhardt, J. P. Briand, M. Prato, K. Kostarelos, and A. Bianco, *Angew Chem Int Ed Engl*, 43 (39), 5242-6, 2004.

[136] J. Oh, G. Yoo, Y. W. Chang, H. J. Kim, J. Jose, E. Kim, J. C. Pyun, and K. H. Yoo, *Biosens Bioelectron*, 50, 345-50, 2013.

[137] A. Le Goff, M. Holzinger, and S. Cosnier, *The Analyst*, 136 (7), 1279-87, 2011.

[138] F. Patolsky, Y. Weizmann, and I. Willner, *Angew. Chem., Int. Ed.*, 43 (16), 2113-2117, 2004.

[139] Y. Lin, F. Lu, Y. Tu, and Z. Ren, *Nano Lett.*, 4 (2), 191-195, 2004.

[140] T. Ahuja, D. Kumar, N. Singh, A. M. Biradar, and Rajesh, *Mater. Sci. Eng. C*, 31 (2), 90-94, 2011.

[141] G. Li, J. M. Liao, G. Q. Hu, N. Z. Ma, and P. J. Wu, *Biosens. Bioelectron.*, 20 (10), 2140-2144, 2005.

[142] P. G. Jamkhande, N. W. Ghule, A. H. Bamer, and M. G. Kalaskar, *J. Drug Delivery Sci. Technol.*, 53, 101174, 2019.

[143] C.-H. Lai, M.-Y. Lu, and L.-J. Chen, *J. Mater. Chem.*, 22 (1), 19-30, 2012.

[144] Z. Li, H. Li, Z. Wu, M. Wang, J. Luo, H. Torun, P. Hu, C. Yang, M. Grundmann, X. Liu, and Y. Fu, *Mater. Horiz.*, 6 (3), 470-506, 2019.

[145] X. Xu, W. Yao, D. Xiao, and T. F. Heinz, *Nat. Phys.*, 10 (5), 343-350, 2014.

[146] M. R. Willner and P. J. Vikesland, *J Nanobiotechnol*, 16 (1), 95, 2018.

[147] S. Rodriguez-Mozaz, M. J. Lopez de Alda, and D. Barceló, *Anal Bioanal Chem*, 386 (4), 1025-41, 2006.

[148] M. C. Estevez, M. A. Otte, B. Sepulveda, and L. M. Lechuga, *Anal Chim Acta*, 806, 55-73, 2014.

[149] E. C. Dreaden, A. M. Alkilany, X. Huang, C. J. Murphy, and M. A. El-Sayed, *Chem. Soc. Rev.*, 41 (7), 2740-2779, 2012.

[150] A. Schröfel, G. Kratošová, I. Šafařík, M. Šafaříková, I. Raška, and L. M. Shor, *Acta Biomater.*, 10 (10), 4023-4042, 2014.

[151] H. K. Kumar, N. Venkatesh, H. Bhowmik, and A. Kuila, *Biomed J Sci &Tech Res*, 4 (2), 3765-3775, 2018.

[152] L. A. Paramo, A. A. Feregrino-Pérez, R. Guevara, S. Mendoza, and K. Esquivel, *Nanomaterials*, 10 (9), 2020.

[153] C. C. Ndaya, N. Javahiraly, and A. Brioude, *Sensors*, 19 (20), 2019.

[154] O. Zeiri, *ACS Sens.*, 5 (12), 3806-3820, 2020.

[155] P. Pengo, M. Şologan, L. Pasquato, F. Guida, S. Pacor, A. Tossi, F. Stellacci, D. Marson, S. Boccardo, S. Pricl, and P. Posocco, *Eur Biophys J.*, 46 (8), 749-771, 2017.

[156] K. Saha, S. S. Agasti, C. Kim, X. Li, and V. M. Rotello, *Chem. Rev.*, 112 (5), 2739-2779, 2012.

[157] D. Vilela, M. C. González, and A. Escarpa, *Anal. Chim. Acta*, 751, 24-43, 2012.

[158] Q. A. Pankhurst, N. T. K. Thanh, S. K. Jones, and J. Dobson, *J. Phys. D: Appl. Phys.*, 42 (22), 224001, 2009.

[159] M. Rai, A. Yadav, and A. Gade, *Biotechnol. Adv.*, 27 (1), 76-83, 2009.

[160] Y. Cui, Y. Zhao, Y. Tian, W. Zhang, X. Lü, and X. Jiang, *Biomaterials*, 33 (7), 2327-2333, 2012.

[161] B. Zheng, S. Xie, L. Qian, H. Yuan, D. Xiao, and M. M. F. Choi, *Sens. Actuators, B*, 152 (1), 49-55, 2011.

[162] Q. Zeng, J.-S. Cheng, X.-F. Liu, H.-T. Bai, and J.-H. Jiang, *Biosens. Bioelectron.*, 26 (8), 3456-3463, 2011.

[163] J. Wang, X. Wang, Y. Song, C. Zhu, J. Wang, K. Wang, and Z. Guo, *Chem. Commun.*, 49 (27), 2786-2788, 2013.

[164] H. Yu, J. Yu, L. Li, Y. Zhang, S. Xin, X. Ni, Y. Sun, and K. Song, *Front. Chem.*, 9, 677876-677876, 2021.

[165] Y. Cui, Z. Zhou, T. Li, K. Wang, J. Li, and Z. Wei, *Adv. Funct. Mater.*, 29 (24), 1900040, 2019.

[166] T.-L. Li, Y.-L. Lee, and H. Teng, *J. Mater. Chem.*, 21 (13), 5089-5098, 2011.

[167] T. H. Kim, Y. H. Kim, S. Y. Park, S. Y. Kim, and H. W. Jang, *Chemosensors*, 5 (2), 2017.

[168] F. A. Sabah, N. M. Ahmed, Z. Hassan, and H. S. Rasheed, *Sens. Actuators, A*, 249, 68-76, 2016.

[169] S. Hussain, T. Liu, M. S. Javed, N. Aslam, and W. Zeng, *Sens. Actuators, B*, 239, 1243-1250, 2017.

[170] S. Chandrasekaran, L. Yao, L. Deng, C. Bowen, Y. Zhang, S. Chen, Z. Lin, F. Peng, and P. Zhang, *Chem. Soc. Rev.*, 48 (15), 4178-4280, 2019.

[171] L. Cheng, Q. Xiang, Y. Liao, and H. Zhang, *Energy Environ. Sci.*, 11 (6), 1362-1391, 2018.

[172] V. Guidi, B. Fabbri, A. Gaiardo, S. Gherardi, A. Giberti, C. Malagù, G. Zonta, and P. Bellutti, *Procedia Eng.*, 120, 138-141, 2015.

[173] Z. Xie, D. Wang, T. Fan, C. Xing, Z. Li, W. Tao, L. Liu, S. Bao, D. Fan, and H. Zhang, *J. Mater. Chem. B*, 6 (29), 4747-4755, 2018.

[174] A. Gaiardo, B. Fabbri, V. Guidi, P. Bellutti, A. Giberti, S. Gherardi, L. Vanzetti, C. Malagù, and G. Zonta, *Sensors*, 16 (3), 2016.

[175] X. Fu, J. Liu, Y. Wan, X. Zhang, F. Meng, and J. Liu, *J. Mater. Chem.*, 22 (34), 17782-17791, 2012.

[176] X. Wang, Z. Xie, H. Huang, Z. Liu, D. Chen, and G. Shen, *J. Mater. Chem.*, 22 (14), 6845-6850, 2012.

[177] A. Giberti, A. Gaiardo, B. Fabbri, S. Gherardi, V. Guidi, C. Malagù, P. Bellutti, G. Zonta, D. Casotti, and G. Cruciani, *Sens. Actuators, B*, 223, 827-833, 2016.

[178] A. Giberti, D. Casotti, G. Cruciani, B. Fabbri, A. Gaiardo, V. Guidi, C. Malagù, G. Zonta, and S. Gherardi, *Sens. Actuators, B*, 207, 504-510, 2015.

[179] X. L. Yu, Y. Wang, H. L. W. Chan, and C. B. Cao, *Microporous Mesoporous Mater.*, 118 (1), 423-426, 2009.

[180] Q. Zhang, S. Ma, R. Zhang, K. Zhu, Y. Tie, and S. Pei, *J. Alloys Compd.*, 807, 151650, 2019.

[181] H. Ji, W. Zeng, and Y. Li, *Nanoscale*, 11 (47), 22664-22684, 2019.

[182] F. Vajhadin, M. Mazloum-Ardakani, and A. Amini, *Med. Devices Sens.*, 4 (1), e10161, 2021.

[183] Y. Wang, S. Ma, L. Wang, and Z. Jiao, *Appl. Surf. Sci.*, 492, 116-124, 2019.

[184] A. S. H. Rabee, M. F. O. Hameed, A. M. Heikal, and S. S. A. Obayya, *Optik*, 188, 78-86, 2019.

[185] W. Guan, N. Tang, K. He, X. Hu, M. Li, and K. Li, *Front. Chem.*, 8 (76), 2020.

[186] D. N. Oosthuizen, D. E. Motaung, and H. C. Swart, *Sens. Actuators, B*, 266, 761-772, 2018.

[187] R. Kumar, O. Al-Dossary, G. Kumar, and A. Umar, *Nano-Micro Lett.*, 7 (2), 97-120, 2015.

[188] X. Tong, W. Shen, X. Chen, and J.-P. Corriou, *Ceram. Int.*, 43 (16), 14200-14209, 2017.

[189] S. Xu, H. Zhao, Y. Xu, R. Xu, and Y. Lei, *ACS Appl. Mater. Interfaces*, 10 (16), 13895-13902, 2018.

[190] Z. Li, Y. Huang, S. Zhang, W. Chen, Z. Kuang, D. Ao, W. Liu, and Y. Fu, *J. Hazard. Mater.*, 300, 167-174, 2015.

[191] D. Han, L. Zhai, F. Gu, and Z. Wang, *Sens. Actuators, B*, 262, 655-663, 2018.

[192] G. Korotcenkov, *Mater. Sci. Eng., B*, 139 (1), 1-23, 2007.

[193] S. F. Shen, M. L. Xu, D. B. Lin, and H. B. Pan, *Appl. Surf. Sci.*, 396, 327-332, 2017.

[194] A. Dey, *Mater. Sci. Eng., B*, 229, 206-217, 2018.

[195] J. Ma, H. Fan, N. Zhao, W. Zhang, X. Ren, C. Wang, Y. Wen, and W. Wang, *Ceram. Int.*, 45 (7, Part A), 9225-9230, 2019.

[196] R. Zhang, T. Zhou, L. Wang, Z. Lou, J. Deng, and T. Zhang, *New J. Chem.*, 40 (8), 6796-6802, 2016.

[197] A. Wei, L. Pan, and W. Huang, *Mater. Sci. Eng., B*, 176 (18), 1409-1421, 2011.

[198] B. Selvaraj, J. B. Balaguru Rayappan, and K. Jayanth Babu, *Mater. Sci. Semicond. Process.*, 112, 105006, 2020.

[199] P. Singh, F. M. Simanjuntak, Y.-C. Wu, A. Kumar, H.-W. Zan, and T.-Y. Tseng, *J. Mater. Sci.*, 55 (21), 8850-8860, 2020.

[200] A. Aljaafari, F. Ahmed, C. Awada, and N. M. Shaalan, *Front. Chem.*, 8 (456), 2020.

[201] H. Du, W. Yang, W. Yi, Y. Sun, N. Yu, and J. Wang, *ACS Appl. Mater. Interfaces*, 12 (20), 23084-23093, 2020.

[202] H. Chen, H. Yu, S. Cui, and C. Liu, *Int. J. Appl. Ceram. Technol.*, 17 (3), 1460-1466, 2020.

[203] M. Hjiri, F. Bahanan, M. S. Aida, L. El Mir, and G. Neri, *J. Inorg. Organomet. Polym. Mater.*, 30 (10), 4063-4071, 2020.

[204] D. Zappa, E. Comini, and G. Sberveglieri, *Procedia Eng.*, 47, 430-433, 2012.

[205] A. Umar, A. A. Alshahrani, H. Algarni, and R. Kumar, *Sens. Actuators, B*, 250, 24-31, 2017.

[206] T. Anukunprasert, C. Saiwan, and E. Traversa, *Sci. Technol. Adv. Mater.*, 6 (3), 359-363, 2005.

[207] C.-H. Han, S.-D. Han, I. Singh, and T. Toupance, *Sens. Actuators, B*, 109 (2), 264-269, 2005.

[208] Y. J. Choi, Z. Seeley, A. Bandyopadhyay, S. Bose, and S. A. Akbar, *Sens. Actuators, B*, 124 (1), 111-117, 2007.

[209] S. Manzeli, D. Ovchinnikov, D. Pasquier, O. V. Yazyev, and A. Kis, *Nat. Rev. Mater.*, 2 (8), 17033, 2017.

[210] W. Choi, N. Choudhary, G. H. Han, J. Park, D. Akinwande, and Y. H. Lee, *Mater. Today*, 20 (3), 116-130, 2017.

[211] J. Ping, Z. Fan, M. Sindoro, Y. Ying, and H. Zhang, *Adv. Funct. Mater.*, 27 (19), 1605817, 2017.

[212] R. Kumar, N. Goel, M. Hojamberdiev, and M. Kumar, *Sens. Actuators, A*, 303, 111875, 2020.

[213] L. Wang, D. Xu, L. Jiang, J. Gao, Z. Tang, Y. Xu, X. Chen, and H. Zhang, *Adv. Funct. Mater.*, 31 (5), 2004408, 2021.

[214] Y. Hu, Y. Huang, C. Tan, X. Zhang, Q. Lu, M. Sindoro, X. Huang, W. Huang, L. Wang, and H. Zhang, *Mater. Chem. Front.*, 1 (1), 24-36, 2017.

[215] J. E. Lee, C. K. Lim, H. J. Park, H. Song, S.-Y. Choi, and D.-S. Lee, *ACS Appl. Mater. Interfaces*, 12 (31), 35688-35697, 2020.

[216] D. Gao, J. Zhang, J. Zhu, J. Qi, Z. Zhang, W. Sui, H. Shi, and D. Xue, *Nanoscale Res. Lett.*, 5 (4), 769, 2010.

[217] N. Barsan, C. Simion, T. Heine, S. Pokhrel, and U. Weimar, *J. Electroceram.*, 25, 11-19, 2010.

[218] K. Diao, J. Xiao, Z. Zheng, and X. Cui, *Appl. Surf. Sci.*, 459, 630-638, 2018.

[219] R. López, G. Villa-Sánchez, I. Vivaldo de la Cruz, C. Encarnación-Gómez, V. H. Castrejón-Sánchez, A. Coyopol, J. E. Mastache, and C. Leyva-Porras, *Results Phys.*, 22, 103891, 2021.

[220] A. Kargar, Y. Jing, S. J. Kim, C. T. Riley, X. Pan, and D. Wang, *ACS Nano*, 7 (12), 11112-11120, 2013.

[221] K. Y. Ko, J.-G. Song, Y. Kim, T. Choi, S. Shin, C. W. Lee, K. Lee, J. Koo, H. Lee, J. Kim, T. Lee, J. Park, and H. Kim, *ACS Nano*, 10 (10), 9287-9296, 2016.

[222] S. Sharma, A. Kumar, N. Singh, and D. Kaur, *Sens. Actuators, B*, 275, 499-507, 2018.

[223] W. Zhang, P. Zhang, Z. Su, and G. Wei, *Nanoscale*, 7 (44), 18364-18378, 2015.

[224] T. Li and G. Galli, *J. Phys. Chem. C*, 111 (44), 16192-16196, 2007.

[225] J. Wu, G. Nie, J. Xu, J. He, Q. Xu, and Z. Zhang, *Phys. Chem. Chem. Phys.*, 17 (48), 32425-32435, 2015.

[226] E. Lee, Y. S. Yoon, and D.-J. Kim, *ACS Sens.*, 3 (10), 2045-2060, 2018.

[227] H. Yan, P. Song, S. Zhang, Z. Yang, and Q. Wang, *RSC Adv.*, 5 (97), 79593-79599, 2015.

[228] X.-Q. Qiao, Z.-W. Zhang, D.-F. Hou, D.-S. Li, Y. Liu, Y.-Q. Lan, J. Zhang, P. Feng, and X. Bu, *ACS Sustainable Chem. Eng.*, 6 (9), 12375-12384, 2018.

[229] S. Cui, Z. Wen, X. Huang, J. Chang, and J. Chen, *Small*, 11 (19), 2305-2313, 2015.

[230] D. Zhang, C. Jiang, and Y. e. Sun, *J. Alloys Compd.*, 698, 476-483, 2017.

[231] P. X. Zhao, Y. Tang, J. Mao, Y. X. Chen, H. Song, J. W. Wang, Y. Song, Y. Q. Liang, and X. M. Zhang, *J. Alloys Compd.*, 674, 252-258, 2016.

[232] D. Zhang, C. Jiang, P. Li, and Y. e. Sun, *ACS Appl. Mater. Interfaces*, 9 (7), 6462-6471, 2017.

[233] Z. Qin, C. Ouyang, J. Zhang, L. Wan, S. Wang, C. Xie, and D. Zeng, *Sens. Actuators, B*, 253, 1034-1042, 2017.

[234] F. Perrozzi, S. M. Emamjomeh, V. Paolucci, G. Taglieri, L. Ottaviano, and C. Cantalini, *Sens. Actuators, B*, 243, 812-822, 2017.

CHAPTER 2

Fabrication of a carbon nanotube based non-enzymatic sensor for urea detection in raw milk sample

Contents

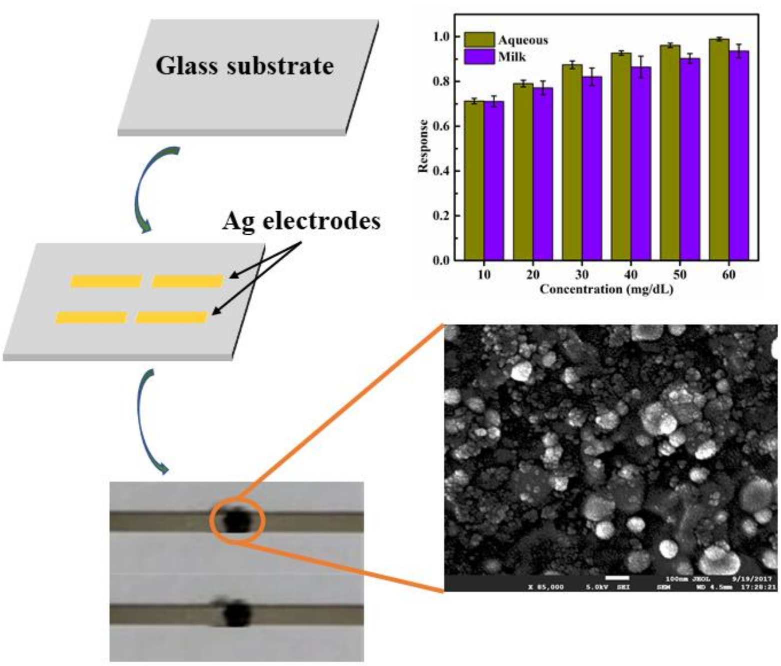

The contents in this chapter have been published in *IEEE Sensors Journal*. 21 (17), 18417-18424 (2021).

Abstract

In this work, we have demonstrated a urea sensor based on starch coated gold nanoparticles (S-AuNPs) and thiol group (-SH) functionalized multiwall carbon nanotube (MWCNT-SH) nanocomposite. The surface modifications of the MWCNTs are characterized using Fourier transform infrared (FTIR) and Raman spectroscopy. The surface analysis of the nanocomposite is recorded using field emission scanning electron microscope (FESEM) and field emission transmission electron microscope (FETEM). The sensor is developed on a glass substrate where silver and MWCNT-SH/S-AuNPs are used as contact electrodes and sensing material, respectively. The response of the sensor is observed over a range between 10 mg/dL to 60 mg/dL with high sensitivity and limit of detection of 0.48 mg/dL. The sensor has demonstrated almost stable performance for two months with excellent reproducibility. The developed sensor is evaluated to detect urea in a raw milk sample, where the sensor can recover urea between 85.17 % and 88.73 % in the milk sample. The proposed sensor has the potential to be used for milk quality assessment in households and dairy industries.

2.1 Overview

Integration of nanomaterials with chemiresistive devices has opened up a large scope of development of sensing parameters for various applications, including healthcare, food processing and agriculture, environmental monitoring etc. In this regard, carbon and metal based nanomaterials have been extensively used for various sensing applications due to their salient features like high surface to volume ratio, superior catalytic activity, cost-effectiveness, excellent electronic and mechanical properties, and unique magnetic, optical or thermal properties [1–7]. Moreover, nanomaterials enabled chemiresistive sensors provide small size, simple structure, ease of fabrication, cost-effectiveness, and ease of integration with microcontrollers for portable device applications. Over the years, carbon based materials like carbon nanotubes (CNTs), carbon blacks, graphene, carbon nanofibers, graphene oxide, nanodiamond, fullerene, and nanocomposites have been able to grab the attention of researchers for sensing applications [8–15]. In the literature, several sensors based on CNT composite such as platinum doped CNT, CNT-poly(diallyldimethylammonium chloride) solution (PDDA), CNT-palladium (Pd), carboxyl functionalized CNT-poly-(m-aminophenol) nanocomposite, molecularly imprinted poly-(methyl methacrylate) on CNT, CNT/zinc oxide (ZnO) nanofibers, etc. have been established for chemical and biosensing applications [16–21].

Urea is the final product of nitrogen metabolism and extensively used in agriculture, food, and dairy industries. However, excessive use of urea in agricultural fields leads to an increase in residual nitrate in the soil indiscriminately and causing soil pollution. Further, the toxicity of ammonia and carbon dioxide, released from urea degradation, is also a detriment to crops and plants. In addition, the excess urea derivatives present on the soil wash off to nearby water streams and water bodies with rain or leaches into the groundwater, thus causing water pollution. Currently, the presence of urea derivatives on daily use products is of foremost concern worldwide [22, 23]. The detection and monitoring of urea have great importance in clinical analysis, food processing technology, and dairy industries. In dairy industries, urea is used as one of the milk adulterate over the years in developing countries and causes serious health hazards such as acidity, ulcers, indigestion, and kidney malfunctions [24, 25]. The permissible concentration level of urea in milk is 18–40 mg/dL [26]. Further, the measurement of milk urea nitrogen (MUN) could help control the diet of dairy cattle as protein overfeeding is harmful to the reproductive process and may cause health problems in the dairy cattle [27]. Several analytical techniques such as colorimetry, infrared spectroscopy, fluorimetry, gas chromatography (GC), high performance liquid chromatography (HPLC), liquid chromatography-mass spectrometry (LCMS), electroanalytical, and chemiluminescence have been explored for urea quantification [28–34]. However, these analytical techniques are time consuming, expensive, and require expertise in running the experiment. Moreover, most of these techniques use urease as an enzyme, which catalyzes the hydrolysis of urea to ammonia (NH_3) and carbon dioxide (CO_2), but stability and storage of enzyme based sensors are always a major concern. Several non-enzymatic sensors based on materials like tin oxide (SnO_2), nickel cobalt oxide ($NiCo_2O_4$) nanoneedles, nickel/cobalt oxide decorated graphene, and polypyrrole/platinum electrode have been used for detection of urea concentration [35–38].

In this study, we have proposed a nanomaterial based resistive sensor to quantify urea concentration in an aqueous solution. The resistive sensor consists of a pair of silver (Ag) electrodes deposited on a glass substrate and surface modified MWCNTs composite as the sensing material. The surface of MWCNTs was functionalized using the oxidation of MWCNTs, followed by the attachment of the thiol group on the surface of MWCNTs. The surface modifications of MWCNTs were characterized by using Fourier transform infrared (FTIR) and Raman spectroscopy. The synthesis of starch coated gold nanoparticles (S-AuNPs) was characterized by transmission electron microscopy (TEM) and UV visible spectroscopy. The thiol functionalized MWCNTs were used as a conducting channel between the electrodes, and the S-AuNPs layer provides the platform for starch-urea reaction. The electrical resistance change was measured based on starch-urea interaction for different urea concentration, and the influence of other milk adulterant was also performed. The response of different urea concentrations was observed between 10 mg/dL to 60 mg/dL with high sensitivity and limit of detection of 0.48 mg/dL. The stability and reproducibility of the urea sensor were examined for the feasibility of its commercial potential. Further, the standard addition and spike-recovery methods were used to detect urea in the raw milk sample.

2.2 Experimental section

2.2.1 Materials

Multiwall carbon nanotubes (purity 98 %, diameter = 6–13 nm, length = 2.5–20 µm), nitric acid (HNO_3), sulfuric acid (H_2SO_4), glass slides, silver wire, dicyclohexylcarbodiimide solution (DCC) ($C_{13}H_{22}N_2$), cysteamine ($NH_2CH_2CH_2SH$), ethanol (C_2H_5OH), starch ($(C_6H_{10}O_5)_n$), urea (NH_2CONH_2), gold(III) chloride solution ($HAuCl_4$), ammonium sulfate ($(NH_4)_2SO_4$), calcium carbonate ($CaCO_3$), hydrogen peroxide solution (H_2O_2) were procured from Sigma Aldrich, India. The Milli-Q grade water was used in all the experiments.

2.2.2 Preparation of materials

The surface of MWCNTs was functionalized using the oxidation of MWCNTs in a (1:3) HNO_3/H_2SO_4 mixture followed by ultrasonication for 3 h at room temperature [39]. Herein, 2 mg MWCNTs were dispersed in 8 mL of the mixed acid solution and sonicated for 3 h. The treated MWCNTs were washed thoroughly with deionized water until the pH of the filtrate became neutral and dried in a vacuum oven. Further, the carboxylic acid functionalized MWCNTs (MWCNT-COOH) were functionalized with thiol group by reacting it with cysteamine in ethanol suspension with the assistance of DCC [40]. Typically, 6 mg of oxidized MWCNTs were spread in 20 mL ethanol and sonicated for 10 min. The DCC solution (0.5 mg/mL) was prepared by spreading in ethanol and added to the MWCNT-COOH solution and stirred for 20 min. Subsequently, 5 mM cysteamine solution was added to the solution and stirred for 24 h at room temperature. The precipitate obtained after 24 h was centrifuged, and thiol-functionalized MWCNTs (MWCNT-SH) were obtained. Starch solution (0.01%) was prepared by dissolving 20 mg of starch powder in 20 mL boiling water and cooled down. Starch coated gold nanoparticles (S-AuNPs) were prepared by adding 300 µL of 0.03 M $HAuCl_4$ solution in 20 mL starch solution, and the mixture was sonicated for 5 min. Further, 400 µL of H_2O_2 was added to the solution and sonicated for 20 min resulting in reddish violet color, which confirmed the formation of starch coated gold nanoparticles [41].

2.2.3 Sensor fabrication

The urea sensor was developed on a clean glass substrate of 1 cm × 1 cm size with MWCNT composites as the sensing material. A pair of silver (Ag) electrodes was deposited on the glass substrate using a shadow mask to cover the channel with a thermal evaporator (Hind High Vacuum, Auto 500). The sensing materials were deposited between the two silver electrodes by drop casting and dried in a hot air oven for 30 min. The fabrication process steps of the urea sensor are illustrated in Figure 2.1 (a)–(d), and the optical image of the urea sensor is shown in Figure 2.1 (e).

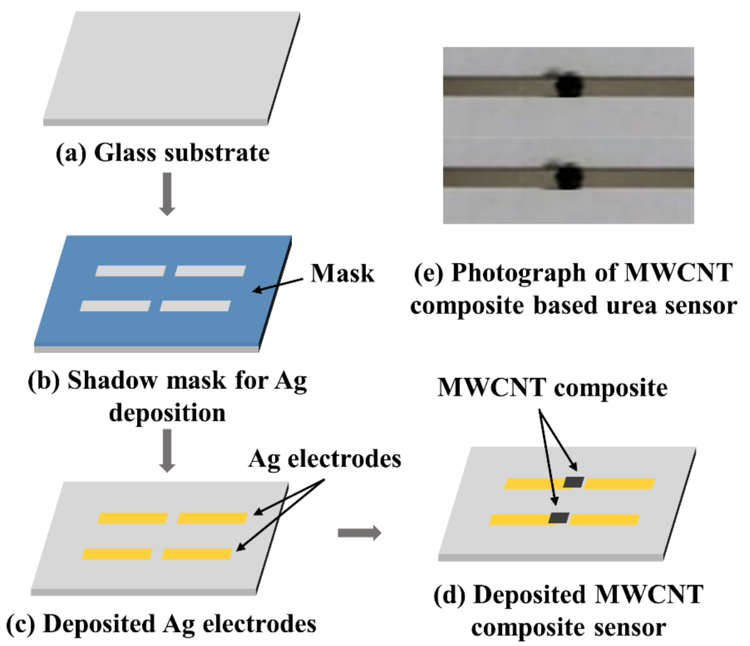

Figure 2.1: (a)–(d) Schematic diagram of MWCNT composite based urea sensor fabrication; (e) Optical image of the fabricated urea sensor.

2.2.4 Characterizations

The material characterizations were performed using Fourier transform infrared spectroscopy (FTIR) (Thermo Scientific Nicolet, iS10) and Raman spectroscopy (Horiba LabRam HR Evolution). Field emission transverse micrograph and selected area electron diffraction (SAED) pattern were recorded with the help of a field emission transmission electron microscope (FETEM) (JEOL, JEM-2100F). The formation of starch coated gold nanoparticles (S-AuNPs) was characterized using UV visible spectrophotometer (Shimadzu, UV-2600). The surface morphology of the materials was recorded using field emission scanning electron microscope (FESEM) (JEOL, JSM-7610F). The thermogravimetric analysis (TGA) was performed using a thermogravimetric analyzer (Mettler Toledo). The electrical characterizations of the fabricated sensors were performed with a parameter analyzer (Keithley, 4200 SCS).

2.3 Results and discussion

2.3.1 Material's characteristics

The attachment of functional groups on the surface of MWCNTs has been characterized using FTIR and Raman spectroscopy. The FTIR spectra of MWCNT, MWCNT-COOH, and MWCNT-SH are shown in Figure 2.2 (a). For MWCNTs, the appearance of a peak at 1634 cm^{-1} is due to the presence of a C=C bond available on the surface of MWCNTs [42]. The oxidation of MWCNTs (MWCNT-COOH) can be confirmed by the appearance of a peak at 1721 cm^{-1}, which is due to the presence of a C=O bond on the carboxyl group [43]. For thiol functionalized MWCNTs, the appearance of peaks at 2972 cm^{-1} and 2876 cm^{-1} are attributed to stretching vibration bands of CH_2 and CH_3, respectively. The peaks at 2552 cm^{-1}, 1655 cm^{-1}, and 1322 cm^{-1} indicate the presence of thiol functional group (-SH), amide group (-CONH) and amine group (-CN) respectively [40].

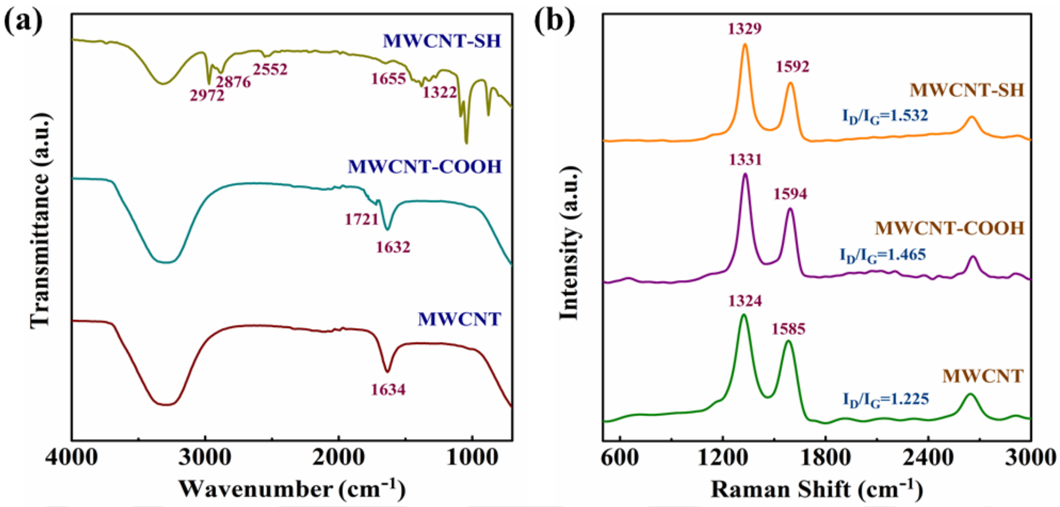

Figure 2.2: Characterization of surface modified MWCNTs at different functionalization stages. (a) FTIR and (b) Raman spectra of MWCNT, MWCNT-COOH, and MWCNT-SH.

Further, Raman spectroscopy is also used to confirm the carboxyl and thiol group's functionalization on the surface of MWCNTs. Figure 2.2 (b) shows the Raman spectra of MWCNTs, MWCNT-COOH, and MWCNT-SH. The prominent peak appeared at 1324 cm^{-1} (D band), and 1585 cm^{-1} (G band) can be attributed to disorder in sp^2 carbons available on the surface of MWCNTs and sp^2 vibration of carbon atoms on the graphitic surface of MWCNTs, respectively. The shifting of D band (1324–1331 cm^{-1}) and G band (1585–1594 cm^{-1}) confirms the functionalization of the carboxyl group on the MWCNTs surface [44]. After the functionalization of the thiol group on the MWCNT-COOH surface, the D band and G band shift from (1331–1329 cm^{-1}) and (1594–1592 cm^{-1}), respectively. Another evidence for this functionalization is the increase in I_D/I_G ratio in the

Raman spectrum [45]. The calculated I_D/I_G ratios for MWCNTs, MWCNT-COOH, and MWCNT-SH are 1.225, 1.465, and 1.532, respectively. The functionalization of the carboxyl group on the MWCNTs surface creates defects on the surface of MWCNTs and the I_D/I_G ratio increases.

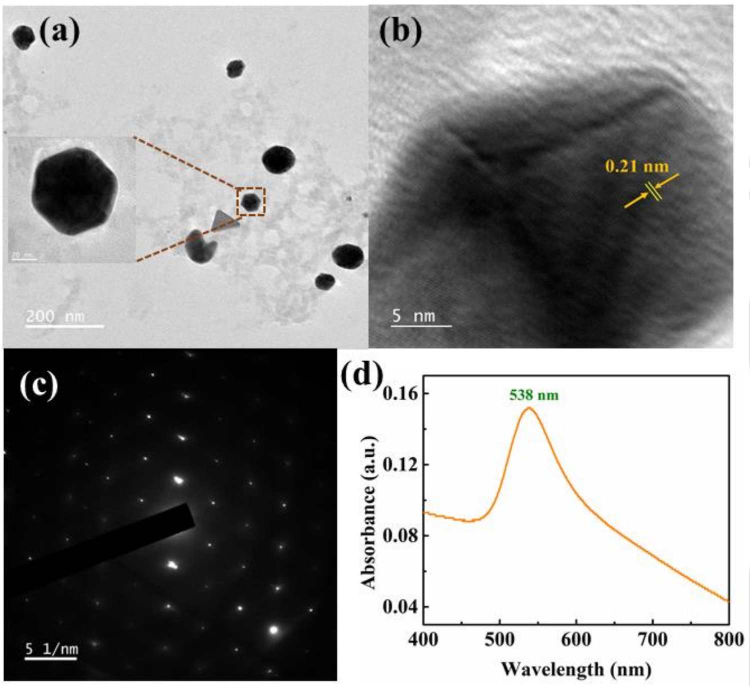

Figure 2.3: S-AuNP characterization, (a) FETEM image at 200 nm scale with inset at 20 nm scale, (b) HRTEM image, (c) SAED pattern, and (d) UV visible spectra.

Figure 2.3 (a) represents the FETEM image of the starch coated gold nanoparticles (S-AuNPs), and the inset shows the enlarged image of a single S-AuNP. The image reveals the formation of a hexagonal shaped S-AuNP. The HRTEM image of the S-AuNP is illustrated in Figure 2.3 (b), and the calculated inter-planar distance is ~0.21 nm. Figure 2.3 (c) shows the SAED pattern of the S-AuNPs, which confirms the crystalline nature of the particles. The UV visible spectroscopy of the S-AuNPs is represented in Figure 2.3 (d).

The observance of UV visible absorption peak at 538 nm endorses the formation of S-AuNPs, as described in [41].

2.3.2 Sensing mechanism

Starch is a polymeric carbohydrate consisting of long chains of glucose connected by glycoside bonds. When starch reacts with urea at elevated temperature (>150 °C) for a longer duration (~2 h), the following chemical reactions occur,

$$\mathrm{St.OH} + \mathrm{CO(NH_2)_2} \xrightarrow{\mathrm{Heat}} \mathrm{St.OCONH_2} + \mathrm{NH_3} \tag{2.1}$$

where $\mathrm{St.OH}$ represents the starch solution. In the present case, we use this concept for the development of the urea sensor. The sensing mechanism of the urea sensor is proposed in Figure 2.4. The synthesized starch coated gold nanoparticles (S-AuNPs) are coated over thiol functionalized MWCNTs. Urea degrades starch above 150 °C, and gold nanoparticles are attached with the thiol (-SH) group present on the surface of MWCNTs. Thus, the electrical conductivity of the sensor changes upon exposure to urea.

Figure 2.5 represents the FESEM images and FTIR spectra of MWCNT-SH, MWCNT-SH/S-AuNP nanocomposite, and reaction product of starch urea reaction. FESEM images for MWCNT-SH, MWCNT-SH/S-AuNP nanocomposite, and reaction product are shown in Figure 2.5 (a), (b) and (c), respectively. The image of MWCNT-SH reveals a smooth surface with entangled tubes, whereas the surface of MWCNT-SH/S-AuNP composite shows formation of clusters. Figure 2.5 (c) shows that the starch layer was decomposed after the reaction at elevated temperature (180 °C), and hence the morphology looks different compared to Figure 2.5 (b). Further, FTIR spectra of starch, urea, and the starch-urea reaction product are shown in Figure 2.5 (d). For starch, peaks at 2934 $\mathrm{cm^{-1}}$ (-CH

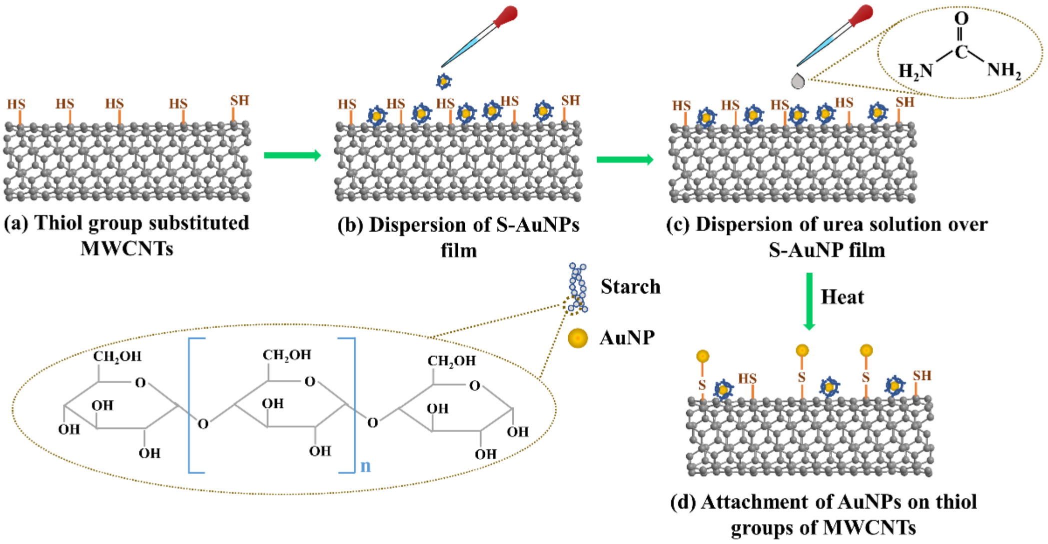

Figure 2.4: Schematic representation of the sensing mechanism of MWCNT-SH nanocomposite based urea sensor.

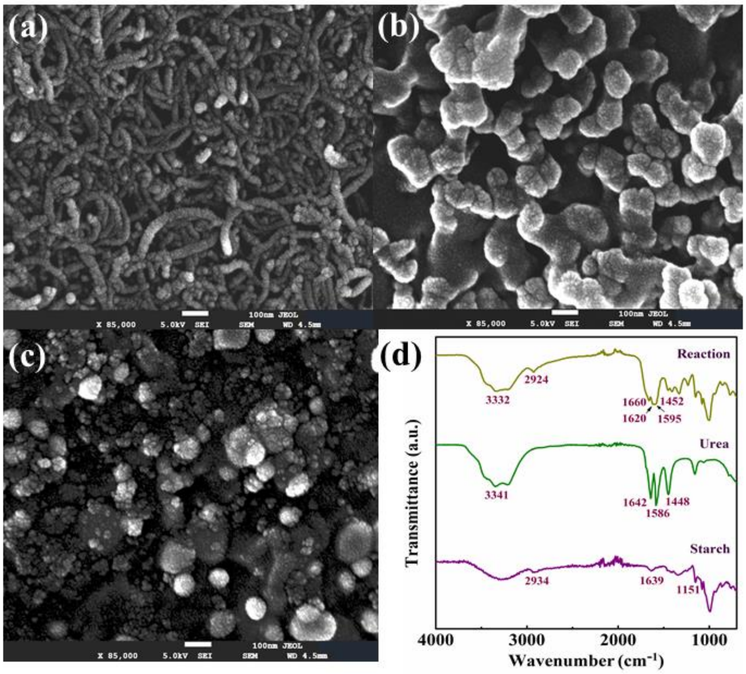

Figure 2.5: FESEM images of (a) MWCNT-SH, (b) MWCNT-SH/S-AuNP composite, and (c) reaction product of starch-urea reaction; (d) FTIR spectra of starch, urea, and starch-urea reaction product.

group), 1639 cm^{-1} (-H bonding in COOH group) and 1159 cm^{-1} (-CO group) have appeared [46]. Peaks at 3341 cm^{-1} (-NH group), 1642 cm^{-1} (-CO group), 1586 cm^{-1} (-NH deformation) and 1448 cm^{-1} (-CN group) are observed for urea [47]. The spectrum of starch-urea reaction product shows peaks at 3332 cm^{-1} (-NH group), 2924 cm^{-1} (-CH group), 1660 cm^{-1} (-CO group), 1620 cm^{-1} (-H bonding in COOH group), 1595 cm^{-1} (-NH deformation) and 1452 cm^{-1} (-CN group).

We have performed a thermogravimetric analysis (TGA) of the components, and the mixtures undergone the chemical reaction. TGA of starch (Figure 2.6 (a)) shows minimal degradation (less than 10%), mainly because of the removal of water and volatile molecules present in the starch molecules, since starch does not undergo decomposition below 200 °C. TGA of urea (Figure 2.6 (b)) shows onset of weight loss at 150 °C and rapid decomposition (up to 65%) above 200 °C. Figure 2.6 (c) shows the TGA analysis of a 1:1 mixture of starch and urea, while Figure 2.6 (d) shows the thermal curves of the three samples in a single plot. The thermal curve of the mixture falls in between that of starch and urea, as the weight loss of the mixture is mitigated by the slow degradation of starch. The thermal curve of urea shows that although onset temperature of urea is 150 °C, the weight loss is insignificant (less than 10%) up to 180 °C. Therefore, in this study on urea sensor, we have restricted the temperature at ~180 °C or below, to avoid total degradation of urea.

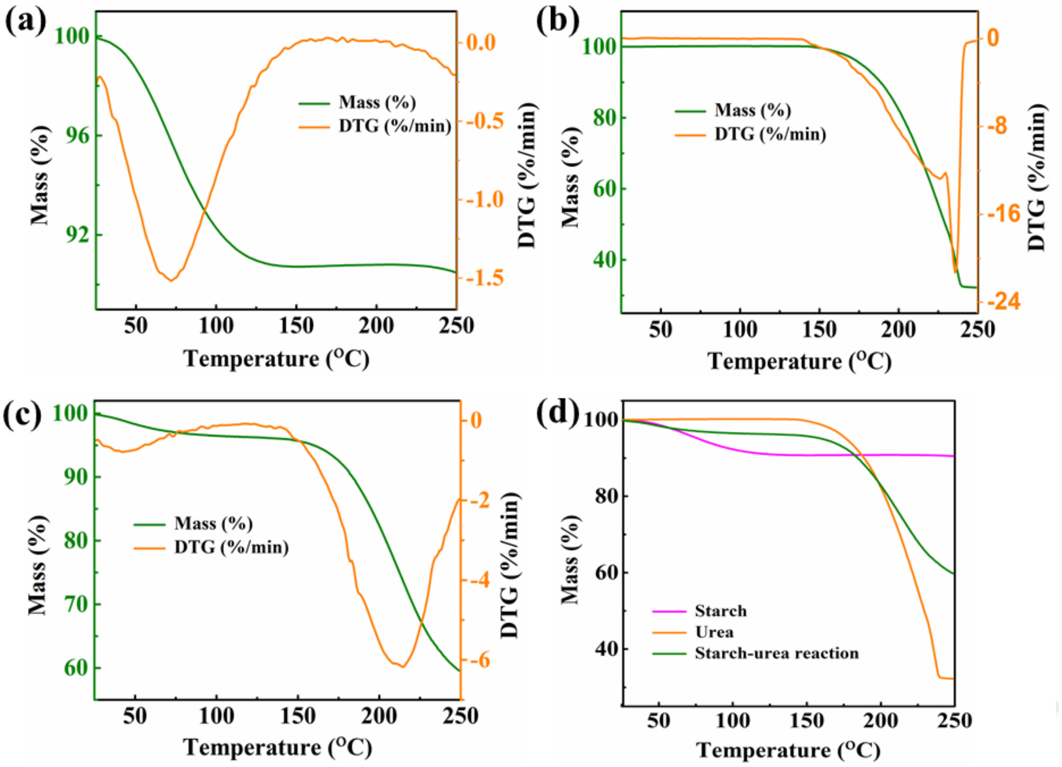

Figure 2.6: TGA analysis of (a) starch, (b) urea, (c) starch-urea reaction product, and (d) comparison of thermal curves of the three samples.

2.3.3 Sensing performance

The MWCNT based urea sensor fabricated as described in section 2.2.3 is initially characterized using a sourcemeter, and the corresponding I-V curve is plotted in Figure 2.7 (a). Then, 5 µL of S-AuNPs solution (0.01%) is dispensed on top of the MWCNT layer and dried for 30 min at room temperature, and corresponding I-V characteristics are measured. It is observed that the current reduces significantly due to the de-doping of the MWCNTs. The electrical conductance of MWCNTs is very high, however starch available on the S-AuNP solution possesses very low electrical conductance. Thus, the overall electrical conductance of the nanocomposite (MWCNT-SH/S-AuNP) reduces and hence the current of the sensor decreases. Subsequently, urea solution of 10 mg/dL is dispensed on the sensor surface and heated at an elevated temperature (~180 °C) for two hours, and resultant I-V characteristics are measured. In this case, urea degrades starch and current through the sensor channel increases. Different urea concentrations ranging from 10 mg/dL to 60 mg/dL are prepared in deionized water to carry out sensitivity analysis. The calibration curve is obtained from the measured values of the sensor current at different urea concentrations. Figure 2.7 (b) shows the sensor response calculated by using the equation,

$$\text{Response} = \frac{\Delta R}{R_0} = \frac{R_0 - R_u}{R_0} \tag{2.2}$$

where R_0 is the resistance of MWCNT-SH/S-AuNP composite, and R_u is the resistance of the sensor after the reaction. The measurements are repeated for three times for each concentration and the average value and error bar are reported. In Figure 2.7 (b), linear regression analysis is used in two different concentration ranges 10–40 mg/dL and 40–60 mg/dL, and the coefficients of determination (R^2) are found to be 0.992 and 0.995, respectively. The sensitivity values of the sensor are 0.72 % per mg/dL and 0.31 % per mg/dL for urea concentration in the ranges of 10–40 mg/dL and 40–60 mg/dL, respectively. The calculated limit of detection (LOD) of the urea sensor is found to be 0.48 mg/dL. Further, another two different combinations of sensing materials are also evaluated for various urea concentrations. In the first case, MWCNT-COOH/starch composite is used as sensing material instead of MWCNT-SH/S-AuNP. In the other case, the MWCNT-COOH/S-AuNP composite is being exposed to different urea concentrations. The calibration plots of MWCNT-COOH/starch and MWCNT-COOH/S-AuNP composite based urea sensors are presented in Figure 2.7 (c) and (d), respectively. The calculated LOD for MWCNT-COOH/starch and MWCNT-COOH/S-AuNP composite based urea

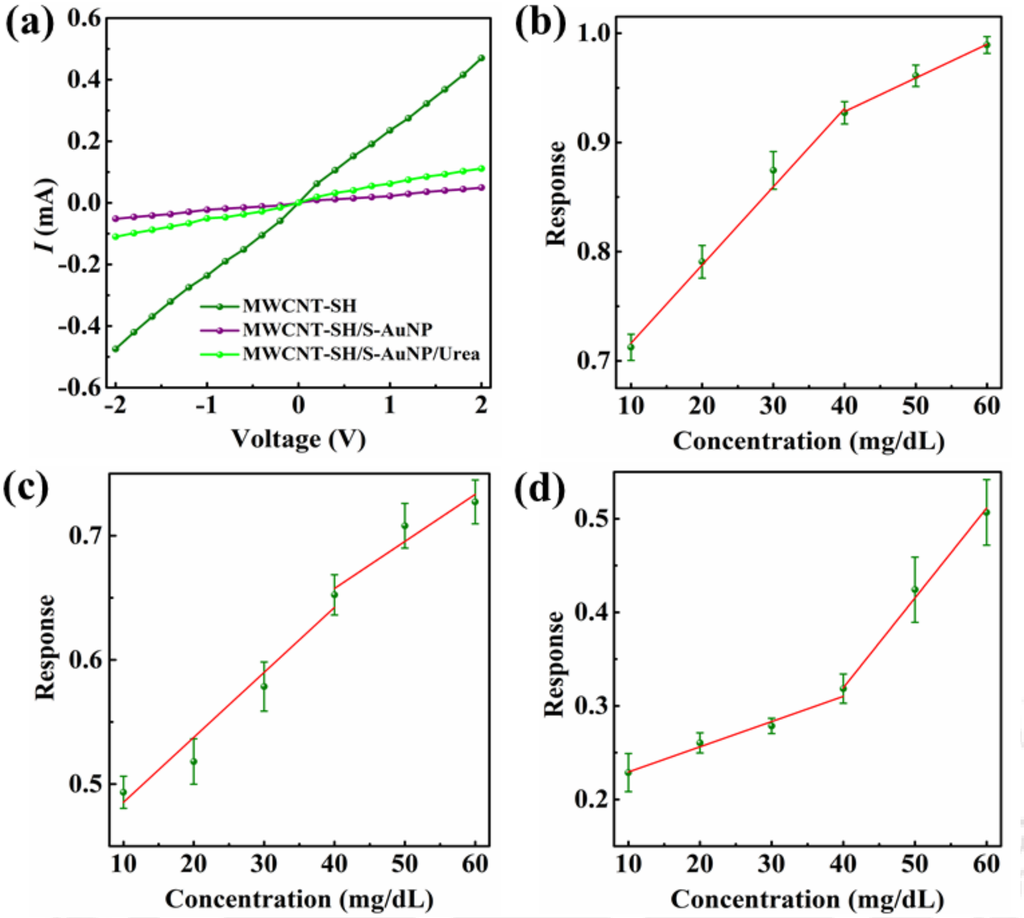

Figure 2.7: (a) I-V analysis of the sensor for MWCNT-SH, MWCNT-SH/S-AuNP nanocomposite, and after reaction of starch with 10 mg/dL urea solution; Response of urea sensor based on (b) MWCNT-SH/S-AuNP, (c) MWCNT-COOH/starch, and (d) MWCNT-COOH/S-AuNP nanocomposites for different urea concentrations.

Table 2.1: Urea sensing parameters of various sensing materials.

Sl. No.	Sensing material	Sensitivity (% per mg/dL)	LOD (mg/dL)
1	MWCNT-SH/S-AuNP	0.72	0.48
2	MWCNT-COOH/starch	0.27	4.62
3	MWCNT-COOH/S-AuNP	0.52	2.23

sensors are found to be 4.62 mg/dL and 2.23 mg/dL, respectively. The sensing parameters, such as sensitivity and LOD of all three sensing material combinations, are shown in Table 2.1. The ascending order of response to urea is found to be MWCNT-COOH/starch, MWCNT-COOH/S-AuNP, and MWCNT-SH/S-AuNP composite.

The selectivity of the sensor judges the practical applicability of any sensor. Therefore, the developed MWCNT-SH/S-AuNP nanocomposite based urea sensor was tested towards various common milk adulterants such as detergent, calcium carbonate, and ammonium sulfate. For the selectivity study, the interference compound of 60 mg/dL concentration was prepared in deionized water. The selectivity of the urea sensor towards other compounds is shown in Figure 2.8 (a). The response of the sensor towards urea is much higher (at least 4 times) compared to other milk adulterants. In order to study repeatability and reproducibility of the sensor, three different sets of the sensor were prepared distinctly in three different batches. The sensors were exposed to urea solutions (60 mg/dL), and the response of the sensor is shown in Figure 2.8 (b). The response of the urea sensor is found to be negligibly changed under the same fabrication procedures, which indicates that the developed urea sensors are highly reproducible. The stability of the sensors was evaluated for two months, and the response is shown in Figure 2.8 (c). The sensors showed excellent stability for two months, with a 7.54 % decrease in response, which exhibits excellent practical applicability of the developed urea sensor. The decrease in the sensor response after four weeks is probably due to the degradation of the starch coated gold nanoparticles solution.

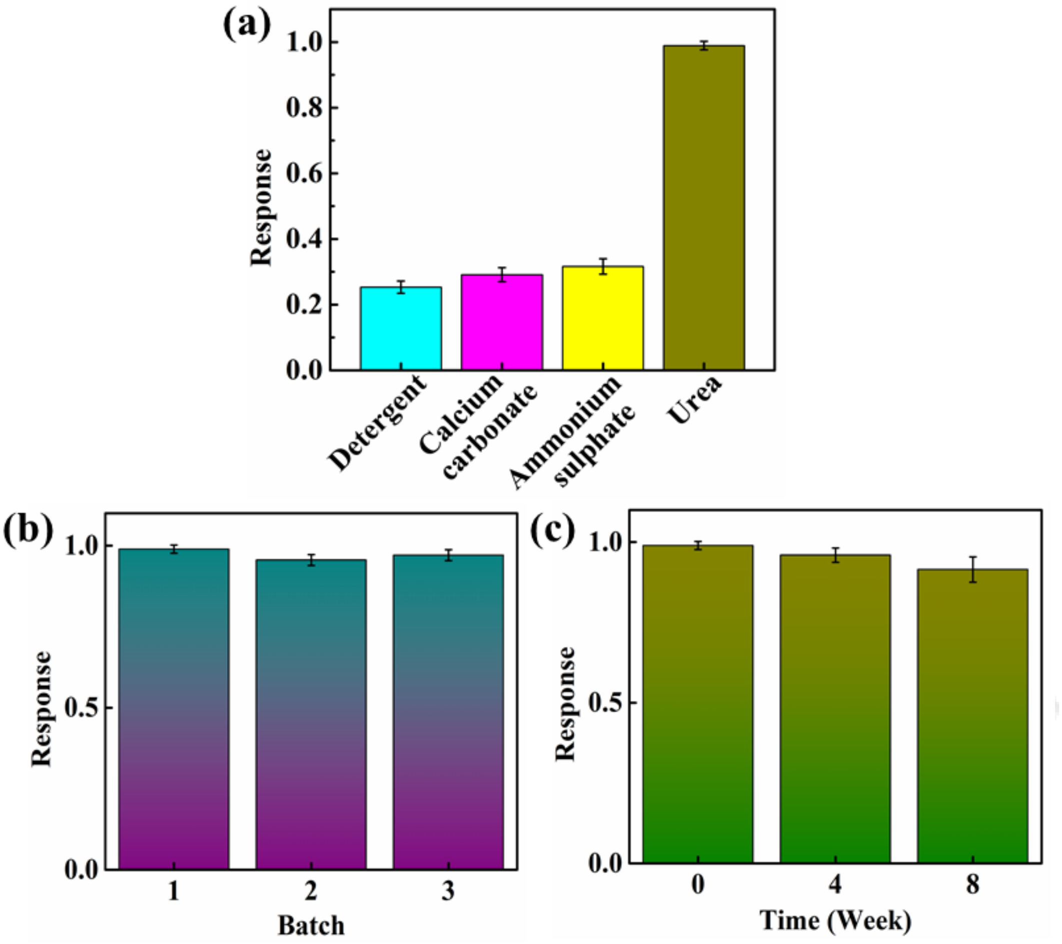

Figure 2.8: (a) Selectivity, (b) Reproducibility, and (c) Stability of the MWCNT-SH/S-AuNP nanocomposite based urea sensor.

2.3.4 Milk quality assessment

The urea sensor was examined to detect urea in raw milk sample to test its practicability. Spike and recovery method was used for the detection of urea in raw milk samples at various concentrations. For this purpose, known concentrations of urea were spiked in the milk sample, and the % recovery of urea from the real sample was calculated by using the following equation,

$$\% \text{ Recovery } = \frac{\mathrm{M-B}}{\mathrm{S}} \tag{2.3}$$

where M and B are the analytical response due to urea in spiked and blank samples, respectively, and S is the urea's analytical response in standard aqueous solutions. Figure 2.9 represents responses for aqueous solution and real sample (milk) between 10 mg/dL and 60 mg/dL concentrations of urea. A gradual increase in response is observed with increase in urea concentrations. The % recovery between 85.17 % and 88.73 % of urea from the milk samples is obtained at different tested concentrations. Further, the results of proposed urea sensor are validated with the standard pH technique, which is used as a standard analytical method for urea quantification in the raw milk samples [48]. Spike and recovery method was used for the detection of urea in raw milk samples at various concentrations. The pH of the sample varies directly proportional to the urea concentrations due to the hydrolysis of urea by an enzyme urease. The urease enzyme solution (1800 U/mL) was prepared by diluting with aqueous glycerol (50 % v/v). The different urea concentration solutions were prepared in a phosphate buffer solution. Firstly, 0.2 mL of urease solution was taken and added to the solutions of different urea concentrations, and then mixed at room temperature. The pH value of each spiked urea concentration was measured with a pH meter (Thermo Scientific EUTECH pH 150). For each spiked urea concentrations, 10 mL milk samples were prepared by adding 5 mL of raw milk and 5 mL of urea solution prepared in buffer solutions. Again, 0.2 mL of urease solution were added to different spiked milk samples and mixed at room temperature, and the pH of the milk samples were recorded. The analytical details of recovered urea, % recovery and relative standard deviation (RSD) of the proposed sensor and the corresponding results of pH technique are mentioned in Table 2.2.

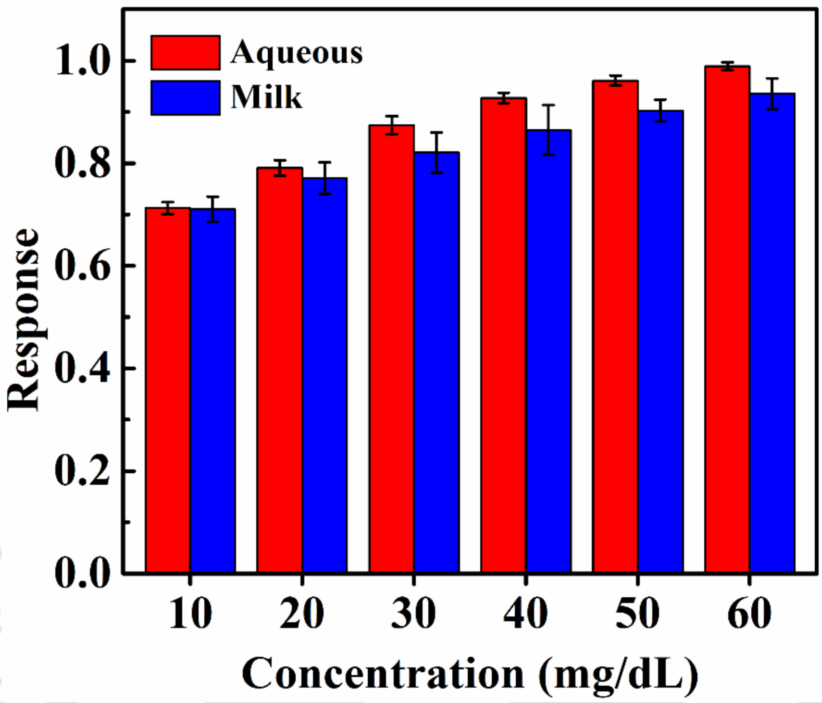

Figure 2.9: Comparative detection of urea in aqueous solution (red bars) and raw milk sample (blue bars) for urea concentrations between 10 mg/dL and 60 mg/dL.

Table 2.2: Recovery of urea from spiked milk samples.

Sl. No.	Spiked urea (mg/dL)	Resistive sensor			Standard method	
		Recovered urea (mg/dL)	% Recovery	RSD	Recovered urea (mg/dL)	% Recovery
1	10	8.87 (±0.03)	88.73	4.11	9.6 (±0.03)	95.99
2	20	17.61 (±0.03)	88.03	3.98	19.44 (±0.03)	97.22
3	30	25.60 (±0.03)	85.32	4.75	28.62 (±0.03)	95.41
4	40	34.07 (±0.04)	85.17	5.61	38.18 (±0.02)	95.45
5	50	43.07 (±0.02)	86.13	2.38	47.05 (±0.03)	94.10
6	60	52.20 (±0.03)	87.01	3.20	56.99 (±0.04)	94.99

2.4 Conclusions

In this work, we have developed a resistive sensor based on MWCNT-SH/S-AuNP nanocomposite for urea detection. The sensor was characterized by FTIR, Raman, UV visible, FETEM, SAED, FESEM, and TGA. The sensor is tested for urea detection in the range of 10 mg/dL to 60 mg/dL with sensitivity and detection limit of 0.72 % per mg/dL and 0.48 mg/dL, respectively. The sensor demonstrated a selective response towards urea and is highly reproducible. The stability of the sensor has been evaluated, where the sensor was found to be stable for two months, with ~7.54 % decrease in sensor response. The sensor can detect urea in raw milk samples with % recovery between 85.17 % and 88.73 %. The prominent features of the developed urea sensor are ease of fabrication, cost effectiveness, robustness, and easy handling. It is suitable for detecting urea in dairy products and has the potential to be translated into a miniaturized portable device for practical applications.

References

[1] V. D. N. Bezzon, T. L. A. Montanheiro, B. R. C. de Menezes, R. G. Ribas, V. A. N. Righetti, K. F. Rodrigues, and G. P. Thim, *Adv. Mater. Sci. Eng.*, 2019, 4293073, 2019.

[2] J. F. Fennell Jr, S. F. Liu, J. M. Azzarelli, J. G. Weis, S. Rochat, K. A. Mirica, J. B. Ravnsbæk, and T. M. Swager, *Angew. Chem., Int. Ed.*, 55 (4), 1266-1281, 2016.

[3] S. Zhang, S. Guo, Z. Chen, Y. Wang, H. Gao, J. Gómez-Herrero, P. Ares, F. Zamora, Z. Zhu, and H. Zeng, *Chem. Soc. Rev.*, 47 (3), 982-1021, 2018.

[4] W. Liu, X. Zhou, L. Xu, S. Zhu, S. Yang, X. Chen, B. Dong, X. Bai, G. Lu, and H. Song, *Nanoscale*, 11 (24), 11496-11504, 2019.

[5] A. A. Yaqoob, H. Ahmad, T. Parveen, A. Ahmad, M. Oves, I. M. I. Ismail, H. A. Qari, K. Umar, and M. N. Mohamad Ibrahim, *Front. Chem.*, 8 (341), 2020.

[6] W. G. Kreyling, M. Semmler-Behnke, and Q. Chaudhry, *Nano Today*, 5 (3), 165-168, 2010.

[7] F. Yavari and N. Koratkar, *J. Phys. Chem. Lett.*, 3 (13), 1746-1753, 2012.

[8] L. Valentini, I. Armentano, J. M. Kenny, C. Cantalini, L. Lozzi, and S. Santucci, *Appl. Phys. Lett.*, 82 (6), 961-963, 2003.

[9] H. Xie, Q. Yang, X. Sun, J. Yang, and Y. Huang, *Sens. Actuators, B*, 113 (2), 887-891, 2006.

[10] E. Czerwosz, E. Kowalska, M. Kozłowski, J. Radomska, H. Wronka, M. Angiola, A. Martucci, and W. Włodarski, *Procedia Eng.*, 87, 963-966, 2014.

[11] D. Yadav, F. Amini, and A. Ehrmann, *Eur. Polym. J.*, 138, 109963, 2020.

[12] B. T. Zhang, X. Zheng, H. F. Li, and J. M. Lin, *Anal Chim Acta*, 784, 1-17, 2013.

[13] L.-M. Peng, Z. Zhang, and S. Wang, *Mater. Today*, 17 (9), 433-442, 2014.

[14] K. D. Patel, R. K. Singh, and H.-W. Kim, *Mater. Horiz.*, 6 (3), 434-469, 2019.

[15] K. S. Novoselov, V. I. Fal′ko, L. Colombo, P. R. Gellert, M. G. Schwab, and K. Kim, *Nature*, 490 (7419), 192-200, 2012.

[16] S. Demir and M. F. Fellah, *Appl. Surf. Sci.*, 504, 144141, 2020.

[17] C. McConnell, S. N. Kanakaraj, J. Dugre, R. Malik, G. Zhang, M. R. Haase, Y.-Y. Hsieh, Y. Fang, D. Mast, and V. Shanov, *ACS Omega*, 5 (1), 487-497, 2020.

[18] N. Roy, R. Sinha, T. T. Daniel, H. B. Nemade, and T. K. Mandal, *IEEE Sens. J.*, 20 (22), 13245-13252, 2020.

[19] P. Supraja, V. Singh, S. R. K. Vanjari, and S. Govind Singh, *Microsyst. Nanoeng.*, 6 (1), 3, 2020.

[20] S. K. Verma, P. Kar, D. J. Yang, and A. Choudhury, *Sens. Actuators, B*, 219, 199-208, 2015.

[21] T. Alizadeh and F. Rezaloo, *Sens. Actuators, B*, 176, 28-37, 2013.

[22] P. S. Francis, S. W. Lewis, and K. F. Lim, *TrAC, Trends Anal. Chem.*, 21 (5), 389-400, 2002.

[23] A. Bose and K. Biswas, *Proc. IEEE Int. Instrum. Meas. Technol. Conf. (I2MTC)*, 1-6, 2018.

[24] S. N. Jha, P. Jaiswal, A. Borah, A. K. Gautam, and N. Srivastava, *Food Bioprocess Technol.*, 8 (4), 926-933, 2015.

[25] U. B. Trivedi, D. Lakshminarayana, I. L. Kothari, N. G. Patel, H. N. Kapse, K. K. Makhija, P. B. Patel, and C. J. Panchal, *Sens. Actuators, B*, 140 (1), 260-266, 2009.

[26] J. S. Jonker, R. A. Kohn, and R. A. Erdman, *J Dairy Sci*, 81 (10), 2681-92, 1998.

[27] B. Roy, B. Brahma, S. Ghosh, D. P. Pankaj, and G. Mandal, *Asian J. Anim. Vet. Adv.*, 6 (1), 1-18, 2011.

[28] H.-H. Deng, G.-L. Hong, F.-L. Lin, A.-L. Liu, X.-H. Xia, and W. Chen, *Anal. Chim. Acta*, 915, 74-80, 2016.

[29] H. Mana and U. Spohn, *Anal. Chim. Acta*, 325 (1), 93-104, 1996.

[30] W.-Q. Xie, K.-X. Yu, and Y.-X. Gong, *Microchem. J.*, 147, 838-841, 2019.

[31] B. K. Boggs, R. L. King, and G. G. Botte, *Chem Commun (Camb)*, (32), 4859-4861, 2009.

[32] G. Abernethy and K. Higgs, *J. Chromatogr. A*, 1288, 10-20, 2013.

[33] W. J. Ma, C. H. Luo, J. L. Lin, S. H. Chou, P. H. Chen, M. J. Syu, S. H. Kuo, and S. C. Lai, *Sensors (Basel, Switzerland)*, 16 (4), 2016.

[34] F. Nie, N. Wang, P. Xu, and J. Zheng, *J. Food Drug Anal.*, 25 (3), 472-477, 2017.

[35] S. G. Ansari, H. Fouad, H.-S. Shin, and Z. A. Ansari, *Chem.-Biol. Interact.*, 242, 45-49, 2015.

[36] S. Amin, A. Tahira, A. Solangi, V. Beni, J. R. Morante, X. Liu, M. Falhman, R. Mazzaro, Z. H. Ibupoto, and A. Vomiero, *RSC Adv.*, 9 (25), 14443-14451, 2019.

[37] Nhi S. Nguyen, G. Das, and Hyon H. Yoon, *Biosens. Bioelectron.*, 77, 372-377, 2016.

[38] S. Mondal and M. V. Sangaranarayanan, *Sens. Actuators, B*, 177, 478-486, 2013.

[39] L. Van Thu, N. Cao Long, L. Quoc Trung, N. Trinh Tung, N. Duc Nghia, and V. Minh Thanh, *Adv. Nat. Sci.: Nanosci. Nanotechnol.*, 4 (3), 035017, 2013.

[40] L. Minati, G. Speranza, S. Torrengo, L. Toniutti, C. Migliaresi, D. Maniglio, M. Ferrari, and A. Chiasera, *Surf. Sci.*, 604 (17), 1414-1419, 2010.

[41] T. K. Sarma and A. Chattopadhyay, *Langmuir*, 20 (9), 3520-3524, 2004.

[42] M. Zhang, Q. Sun, Z. Yan, J. Jing, W. Wei, D. Jiang, J. Xie, and M. Chen, *Aust. J. Chem.*, 66 (5), 564-571, 2013.

[43] A. Yıldırım and T. Seckin, 2014, 1-6, 2014.

[44] S. Abdulla, T. L. Mathew, and B. Pullithadathil, *Sens. Actuators, B*, 221, 1523-1534, 2015.

[45] N. Roy, S. Mitra, N. M. Das, N. Mandal, D. Bandyopadhyay, H. B. Nemade, and T. K. Mandal, *IEEE Sens. J.*, 20 (5), 2278-2286, 2020.

[46] A. Hebeish, A. Aly, A. El-Shafei, and S. Zaghloul, *Egyptian J. Chem.*, 52 (1), 73-89, 2009.

[47] M. Manivannan and S. Rajendran, *Int. J. Eng. Sci. Technol.*, 3 (11), 8048-8060, 2011.

[48] M. Luzzana and R. Giardino, *Le Lait*, 79 (2), 261-267, 1999.

CHAPTER 3

Development of a chemiresistor with surface modified carbon nanotubes for CO gas sensing application

Contents

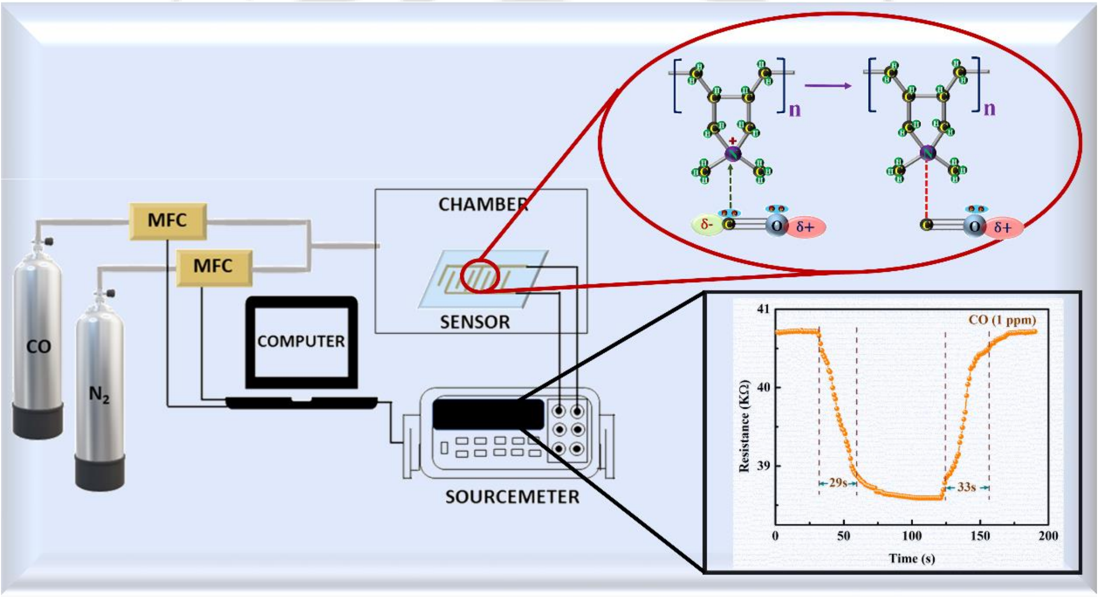

The contents in this chapter have been published in *IEEE Sensors Journal*. 20 (22), 13245-13252 (2020).

Abstract

A resistive sensor based on multiwalled carbon nanotube (MWCNT)-poly(diallyldimethylammonium chloride) solution (PDDA) composite is proposed for highly sensitive carbon monoxide (CO) detection at room temperature. The surface of MWCNTs is functionalized with PDDA, and the functionalization is investigated by Fourier transform infrared and Raman spectroscopy. The MWCNT-PDDA composite is used as a sensing material with deposited interdigitated electrodes (IDE) of silver (Ag) on glass substrates. The resistance of the sensors changes due to charge transfer from CO to the positively charged quaternary ammonium group present on PDDA. The developed sensors are able to detect very low concentrations of CO gas ranging from 1 to 20 ppm with high sensitivity and limit of detection (LOD) of 127 ppb. The interference of other gases and volatile organic compounds is investigated, and the results are presented. The influence of humidity and temperature on the sensors is also explored. The stability and repeatability of the sensors are examined, and the sensors are almost stable for 2 months with excellent reproducibility. The sensors also follow the Langmuir adsorption/desorption model. The sensors have shown excellent potential for rapid CO gas sensing, and it can be used in wearable electronics applications.

3.1 Overview

In recent times, researchers across the globe have been exploring the potential of chemiresistive sensors for gas, chemical, and biosensing applications. The advantages of nanomaterials enabled chemiresistive sensor over conventional sensing techniques have been discussed in detail in the previous chapters. In this regard, several nanoengineered materials such as nanotubes, nanowires, nanoribbons, nanobelts have been used to fabricate chemiresistive sensors for chemical and biosensing applications [1–6]. The prominent features of carbon nanotube (CNT) based sensors and various surface modification/functionalization approaches have been discussed in detail in the previous chapters. In particular, CNTs have been employed to fabricate highly selective and sensitive gas sensors due to their excellent mechanical and electrical properties, and low-temperature operation [7–12]. However, pristine CNTs are hardly selective, and hence surface functionalization is required for selective and sensitive operation [13]. In this regard, suitable metal oxides or metals or conducting polymers can be attached on the surface of CNTs to enhance the selectivity of the sensors [14–16].

Carbon monoxide (CO) is a toxic, odorless, and colorless air pollutant, and it is harmful to human health and the environment when it is leaked in the air [17]. The major source of CO pollutants is automotive emissions, combustion of carbon comprising fuels such as natural gas, coal, gasoline, wood, and industrial activities [18, 19]. Exposure to CO for a longer duration of time can lead to headaches, nausea and vomiting, dizziness, and in severe cases, unconsciousness, or death [20]. Exhalation of moderate to high levels of CO over long periods reduces the amount of oxygen carried by hemoglobin around the human body and increases the risk of heart disease [21]. Thus, CO gas monitoring and sensing at room temperature with high sensitivity and selectivity are of paramount importance for environmental safety, industrial control, and health hazards, etc. Over the last decades, several techniques such as electrochemical, thermoelectric, optical, potentiometric, and resistive sensors have been used for the CO gas detection [22–25]. In this regard, various metal oxide such as zinc oxide (ZnO), copper oxide (CuO), tin oxide (SnO_2), cobalt oxide (Co_3O_4), samarium oxide (Sm_2O_3), gallium oxide (Ga_2O_3), indium oxide (In_2O_3) etc. have been employed as a sensing material for CO detection [26–32]. However, the major drawback of metal oxide-based sensors is high operating temperature and, thus, the requirement of additional heating arrangement for CO detection. Of the late, various nanocomposites based on CNT like PANI-MWCNT, ZnO/MWCNT, Pt/MWCNTs, Pt doped SWCNT have been employed as sensing material for CO detection [33–36].

In contrast to the above works, we have proposed a MWCNT-PDDA composite based resistive sensor for low concentration detection of CO gas at room temperature. For sensor development, MWCNT-PDDA composite was used as a sensing material with deposited interdigitated electrodes (IDE) on glass substrates. The substitution of PDDA on the MWCNT surface was confirmed using Fourier transform infrared (FTIR) and Raman spectroscopy. The gas sensing of different CO concentrations ranging from 1 to 20 ppm was measured inside a controlled gas chamber. The schematic diagram of the CO gas sensing setup with the sensor is shown in Figure 3.1. The effect of temperature and humidity on the sensors was investigated, and the influence of other interfering gases was also explored. The sensors showed fast response and recovery time with limit of detection (LOD) of 127 ppb. We discussed the sensing mechanism of the CO gas sensor based on the adsorption/desorption model, and the experimental results confirmed the Langmuir model.

3.2 Experimental section

3.2.1 Materials

Multiwalled carbon nanotubes (purity 98 %, diameter = 6–13 nm, length = 2.5–20 µm), poly(diallyldimethylammonium chloride) ($(C_8H_{16}NCl)_n$) solution, glass slides, silver wire, methanol (CH_3OH), ethanol (C_2H_5OH), 2-propanol (C_3H_7OH), and acetone (C_3H_6O) were procured from Sigma Aldrich (India). The chemicals were of analytical grade and employed in the experiments without further purification. The Milli-Q grade water was used for cleaning and to prepare the solutions.

3.2.2 Preparation of MWCNT-PDDA composite

The synthesis of the MWCNT-PDDA composite was carried out by following the surface modification method [37]. Typically, MWCNTs (2 mg) were dispersed in 1 mL of aqueous PDDA solution (5 %) and sonicated for 10 min, followed by stirring for 3 h. Further, the solution was centrifuged for 10 min, and the collected MWCNT-PDDA composite was washed with deionized water to remove loosely attached PDDA on the MWCNT surface.

3.2.3 Sensor fabrication

The sensor was fabricated using MWCNT-PDDA composite as the sensing material. The sensor was developed on a glass substrate, which was cut into pieces of 1 cm x 1 cm and cleaned by using standard substrate cleaning methods. The fabrication process of the

MWCNT-PDDA based CO sensor are illustrated in Figure 3.2 (a)–(c). The IDEs were patterned on the glass substrate by using a shadow mask, and Ag electrodes were thermally evaporated (Hind High Vacuum, Auto 500) on the glass substrates. The patterned substrates were treated with UV ozone for 10 min for better adhesion of MWCNT-PDDA composite on the substrates. Typically, 10 µL of MWCNT-PDDA composite solution was drop casted on the patterned substrate and dried at room temperature. A photograph of the MWCNT-PDDA based CO sensor is shown in Figure 3.2 (d). The sensor was placed inside a controlled environment chamber, and the IDEs were connected with a sourcemeter (Keithley 4200 SCS, U.S.A.) for electrical measurements. Computer-controlled mass flow controllers (MFC) were used to regulate the CO and N_2 gas flow to the chamber. A 100 ppm CO gas cylinder was used to prepare five different concentrations of CO, ranging from 1 to 20 ppm.

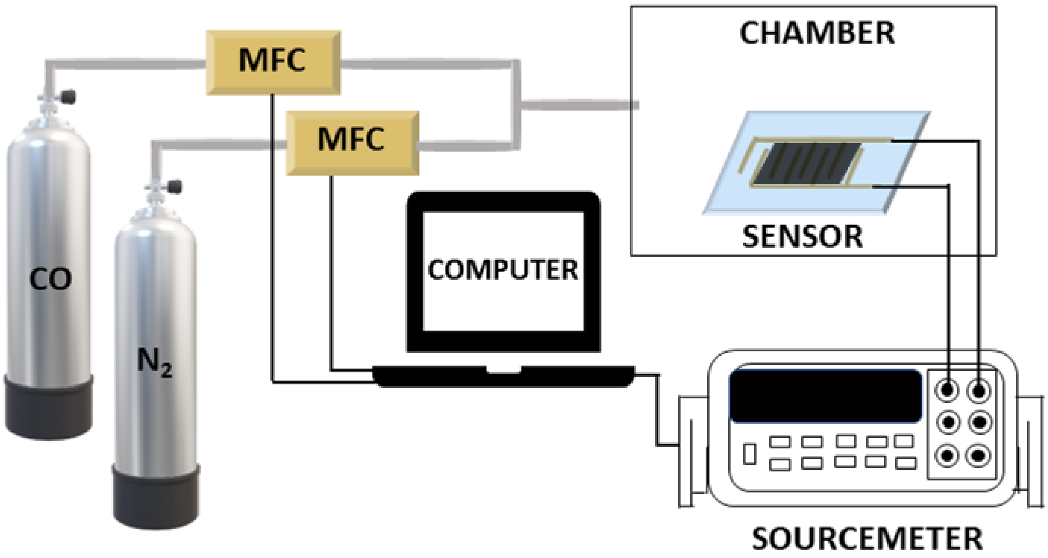

Figure 3.1: Schematic diagram of the CO sensing measurement setup with the sensor.

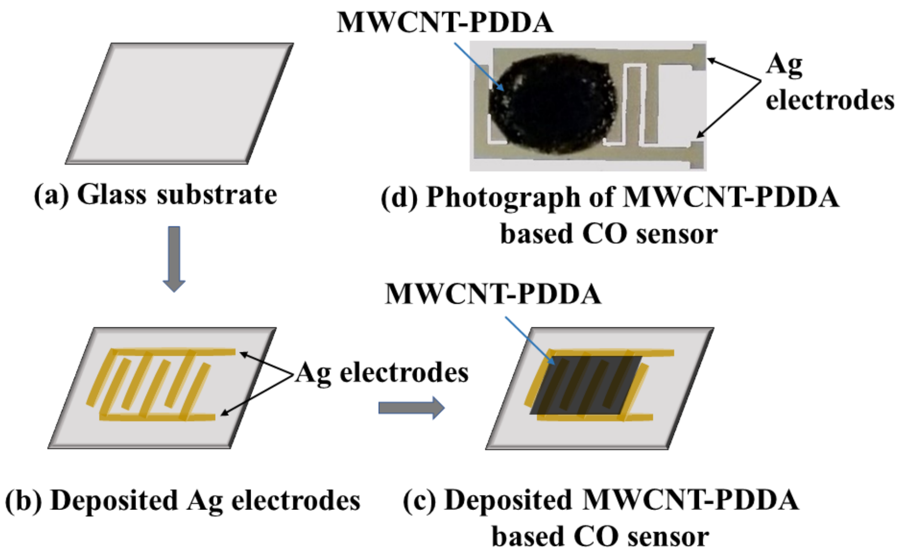

Figure 3.2: (a)–(c) The fabrication steps of the MWCNT-PDDA based CO sensor; (d) Optical image of the CO sensor.

3.2.4 Sensing mechanism

The sensing mechanism of CO sensing is based on the adsorption (physisorption) phenomenon of the CO molecule on the MWCNT-PDDA composite. PDDA contains a positive charge on the nitrogen atom [38]. On the other hand, in the case of CO, the carbon atom acts as the nucleophilic part, as mentioned in the previous work reported by Frenking et al. [39]. Therefore, when the CO comes in contact with the MWCNT-PDDA composite, a charge transfer phenomenon from CO to the positively charged quaternary ammonium group of PDDA takes place, as shown in Figure 3.3. Owing to this charge transfer to the composite, the overall resistance of the sensor decreases. In other words, the charge transfer helps the sensor to gain more conductance resulting in giving higher current. However, during the removal of the CO molecule from the composite, it regains the electrons from the quaternary ammonium group of the PDDA, which increases the resistance of the sensor and thus the current reduces.

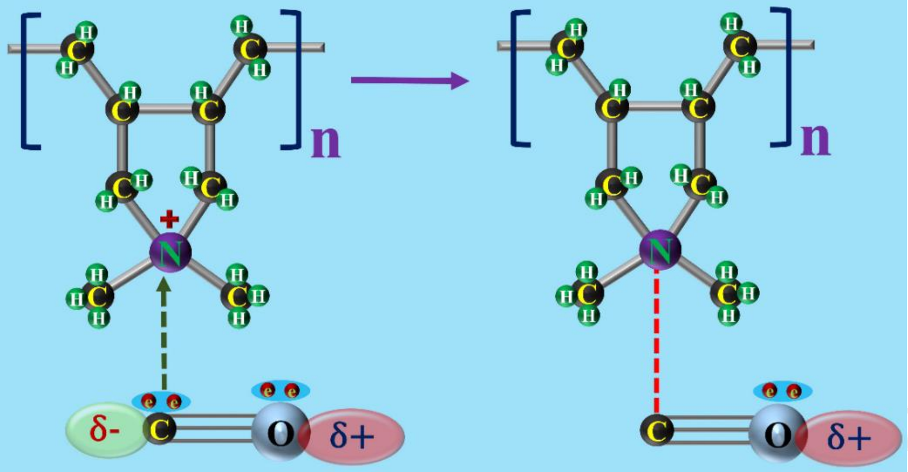

Figure 3.3: Schematic diagram of the CO sensing measurement setup with the sensor.

3.3 Results and discussion

3.3.1 Characterizations

The FTIR spectroscopy (Thermo Scientific Nicolet iS10 FTIR spectrometer, U.S.A.) has been performed to confirm the surface modification of MWCNT with PDDA. The FTIR spectra of MWCNT, PDDA, and MWCNT-PDDA composite is shown in Figure 3.4 (a). The observed peak at 1630 cm^{-1} in the spectrum of MWCNTs can be assigned to the stretching vibration of C=C [40]. The observed peaks at 2900 cm^{-1} and 2830 cm^{-1} in the spectrum of PDDA can be attributed to stretching vibrations of CH_2 and CH_3, respectively. The appearance of peaks at 1637 cm^{-1}, 1479 cm^{-1}, and 1320 cm^{-1} in PDDA have corresponded to C=C bond, CH_2 bending, and C-N bond, respectively [37, 41]. The difference in the spectra of MWCNT-PDDA composite with MWCNT and PDDA confirms the surface modification of PDDA on MWCNT. The peaks at 2881 cm^{-1}, 2816 cm^{-1}, and 1475 cm^{-1} in the spectrum of MWCNT-PDDA composite are attributed to the presence of PDDA on the surface of MWCNT.

Raman spectroscopy (Horiba LabRam HR Evolution Raman spectrophotometer, U.S.A.) analysis of MWCNT and MWCNT-PDDA composite are shown in Figure 3.4 (b). The observed D band (1325 cm^{-1}) and G band (1585 cm^{-1}) for both the spectra, corresponding to the defects in the sp^3 carbon atoms, and crystalline graphitic carbon present in MWCNT [37, 42]. The shifting of D band (1325–1327 cm^{-1}) and G band on (1585–1588 cm^{-1}) confirms the functionalization of PDDA the surface of MWCNT. Further, the change in the intensity ratio of D band and G band (I_D/I_G) can also be used for the confirmation of the functionalization. The measured value of I_D/I_G for MWCNT and MWCNT-PDDA composite is 1.38 and 1.42, respectively. The I_D/I_G is increased for MWCNT-PDDA composite due to the creation of more defects on the surface of MWCNT.

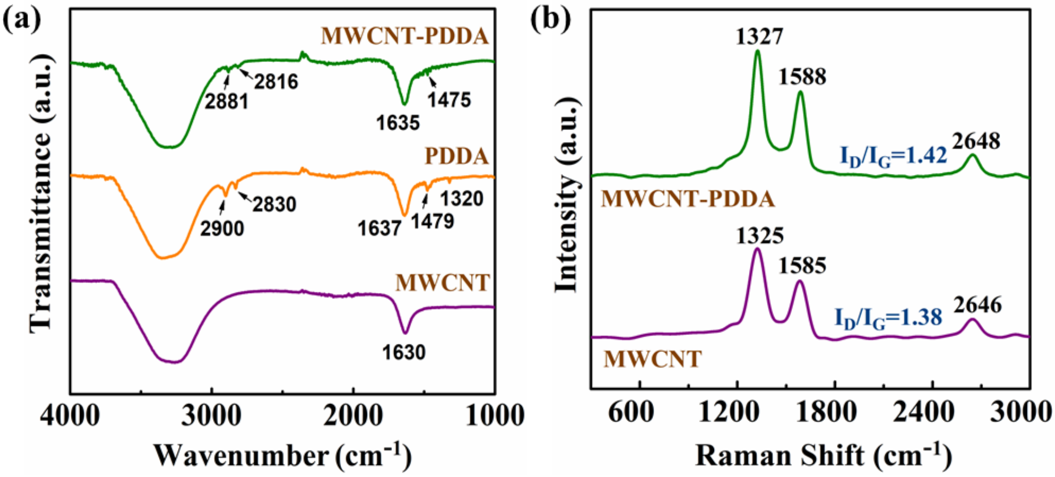

Figure 3.4: Spectroscopic analysis of surface modified MWCNTs at different stages. Plot (a) and (b) show the FTIR and Raman spectra of the MWCNT-PDDA composite, respectively.

3.3.2 Response of CO sensor

The transient response of the sensor based on MWCNT-PDDA composite was measured for different concentrations of CO gas ranging from 1 to 20 ppm. The transient response of the sensor for 1 ppm CO gas is shown in Figure 3.5 (a). When the sensor is exposed to CO gas, the resistance of the sensor decreases and almost saturates after some time due to the adsorption of CO onto the surface of the MWCNT-PDDA composite. The resistance of the sensors changes due to charge transfer from CO to the positively charged quaternary ammonium group present on PDDA. As the CO gas is removed, the sensor reaches its initial resistance. The transient response for other concentrations of CO gas is also the same in nature. Figure 3.5 (b) shows the transient response of the sensor for 1 ppm, 5 ppm, 10 ppm, 15 ppm, and 20 ppm CO gas. The response time of a sensor is defined as the time taken by the sensor to reach from 10 % to 90 % of the output signal and vice-versa for recovery time. The response and recovery time of the sensor for 1 ppm CO gas is shown in Figure 3.5 (c). The response time is lesser compared to the recovery time of the sensor. The response and recovery time variations of the MWCNT-PDDA composite sensor upon exposure to different CO gas concentrations are shown in Figure 3.5 (d). The response time of the sensor decreases as the concentration of CO gas increases, while it is opposite in the case of recovery time. The measured value of response and recovery time is shown in Table 3.1. The sensor exhibited the fastest response and recovery time of 18 s (20 ppm) and 33 s (1 ppm) for CO gas sensing, respectively.

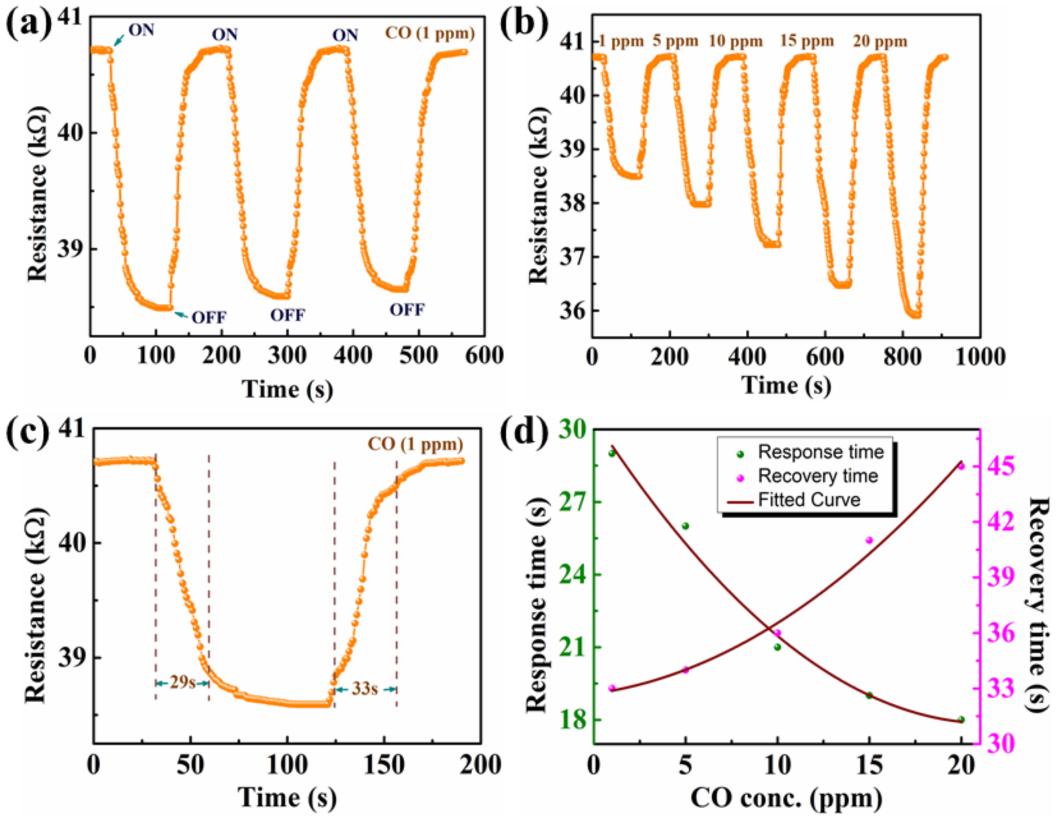

Figure 3.5: Plot (a) and (b) show the transient response of the sensor upon exposure to 1 ppm CO, and other concentrations of CO gas, respectively; Plot (c) and (d) show the measurement of response and recovery time of the sensor upon exposure to 1 ppm CO, and at various concentrations of CO gas, respectively.

Table 3.1: Response and recovery time of the sensor.

CO Concentration (ppm)	Response time (s)	Recovery time (s)
1	29	33
5	26	34
10	21	36
15	19	41
20	18	45

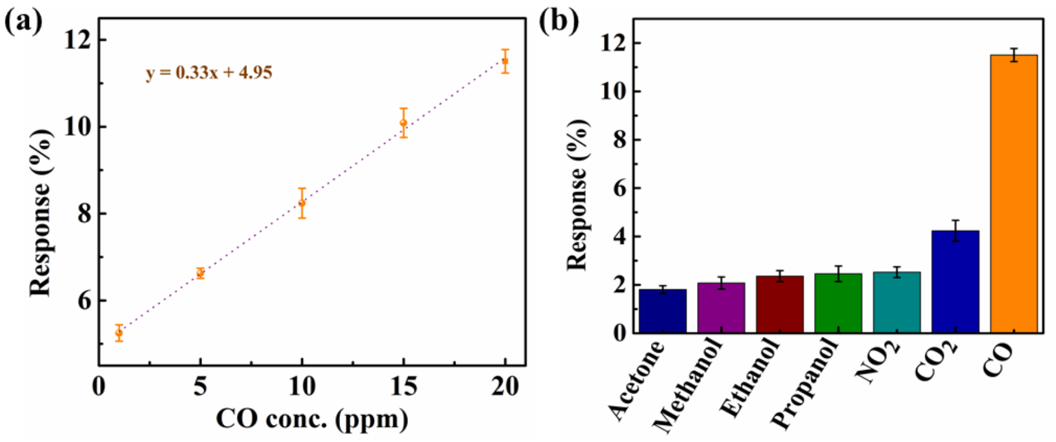

Figure 3.6: Plot (a) shows the response of the MWCNT-PDDA composite towards different CO concentrations ranging from 1 to 20 ppm. Plot (b) shows the response of the sensor towards different gases such as acetone, methanol, ethanol, propanol, NO_2, CO_2, and CO.

The response of the sensor is measured by exposing the MWCNT-PDDA composite to various concentrations of CO gas (1, 5, 10, 15, and 20 ppm). The response of the sensor is given by the following equation,

$$Response\ (\%) = \frac{\Delta R}{R_0}\ \text{x}\ 100\% = \frac{R_g - R_0}{R_0}\ \text{x}\ 100\% \qquad (3.1)$$

where R_0 and R_g are the resistance of the sensor before and after exposure to CO gas, respectively. The response of the sensor for different CO concentrations are shown in Figure 3.6 (a). Further, linear regression analysis is used to calculate the slope of the calibration curve, and Figure 3.6 (a) shows a very good linear response upon exposure to various concentrations (1–20 ppm) of CO gas. The measured value of response (%) for 1 ppm, 5 ppm, 10 ppm, 15 ppm, and 20 ppm are 5.25, 6.62, 8.24, 10.09, and 11.51, respectively. The limit of detection (LOD) of the sensor is calculated and found to be 127 ppb. The sensor was exposed to different gases (20 ppm) to check the selectivity of the sensor. The selectivity analysis of the sensor towards different gases is shown in Figure 3.6 (b). The response of the sensor for CO gas is much bigger compared to the other gases, including CO_2, NO_2, propanol, ethanol, methanol, and acetone.

Since the gas sensing measurements were performed at room temperature, another study was also done to figure out the effect of temperature on the base resistance of the sensors. Figure 3.7 (a) represents that the base resistance of the sensors decreases with an increase in temperature. The change in base resistance of the sensor is less up to 100 °C, and hence, the sensors are considerably stable for different temperatures up to 100 °C. The effect of humidity on the base resistance of the sensors is shown in Figure 3.7 (b). The base resistance of the sensors increases with an increase in relative humidity, and the measured maximum change of base resistance was 4 % for 80 % relative humidity. Though the base resistance of the sensors is changing with relative humidity, the normalized resistance or sensitivity of the sensors changes marginally since the final resistance also changes. This marginal change in normalized resistance does not influence the sensing efficiency of the device. The reproducibility studies of the sensors were carried out with three different sensors prepared distinctly in three different batches and are shown in Figure 3.7 (c). In order to find the stability of the sensors, the base resistance of the sensor was measured for 2 months with a week interval. The sensors were almost stable for 2 months, and the stability study is shown in Figure 3.7 (d). The present sensor exhibits the fastest response time of 18 s and recovery time of 33 s with very low CO detection range at room temperature.

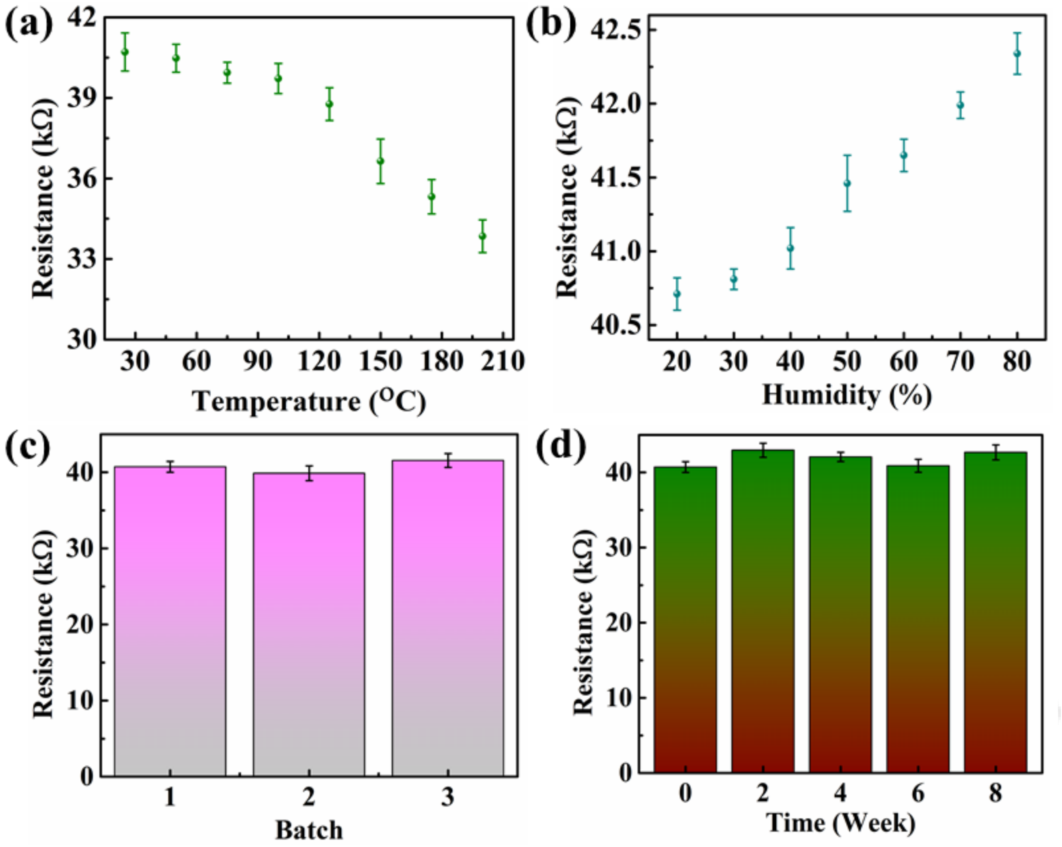

Figure 3.7: Plot (a) and (b) show the effect of temperature and humidity on the base resistance of the sensors, respectively; Plot (c) and (d) show the reproducibility and stability analysis of the sensors, respectively.

3.3.3 Adsorption-desorption kinetics

The interaction between CO molecules and the synthesized MWCNT-PDDA composite occurs by the following reaction pathway [33].

$$CO + e^{-} \xleftrightarrow{k_{+}/k_{-}} CO^{-}\ (ads) \tag{3.2}$$

where, k_+ and k_- are the adsorption and desorption rate constants. Here, we have assumed that a single layer of CO gets deposited on the MWCNT-PDDA composite by following the adsorption/desorption model (Langmuir model). The response and recovery time of the sensing system can also be obtained by fitting the conductance data in the adsorption/desorption model [43]. The changes in conductance values are written below,

$$\Delta g = \Delta g_{\max} \left[1 - e^{\left(-\frac{t}{\tau_+}\right)}\right] \text{ for response} \tag{3.3}$$

$$\Delta g = \Delta g_{\max} \left[e^{\left(-\frac{t}{\tau_-}\right)}\right] \text{ for recovery} \tag{3.4}$$

where Δg and $\Delta g_{\max}$ represent the change in conductance (time-dependent) and the maximum conductance change, respectively. τ_+ and τ_- are the response time and the recovery time, respectively. These two parameters are expressed by the following equations [44],

$$\tau_+ = \frac{1}{k_+ C + k_-} \tag{3.5}$$

$$\tau_- = \frac{1}{k_-} \tag{3.6}$$

where C represents the concentration of CO. However, for reducing the complicacy in fitting, the exponential curves (corresponding equations 3.3 and 3.4) can be converted to straight lines by taking natural logarithm in both the sides and hence, the equations become as follows,

$$\ln\left(1 - \frac{\Delta g}{\Delta g_{\max}}\right) = -\frac{t}{\tau_+} \tag{3.7}$$

$$\ln\left(\frac{\Delta g}{\Delta g_{\max}}\right) = -\frac{t}{\tau_-} \tag{3.8}$$

We have shown one representative result by fitting the data in equations (3.7) and (3.8) in Figure 3.8 (a) and (b), and both the R^2 values for these two plots are 0.99. The R^2 values indicate that our prior assumption regarding the adsorption/desorption model is valid, i.e., our CO sensing system also follows the Langmuir model.

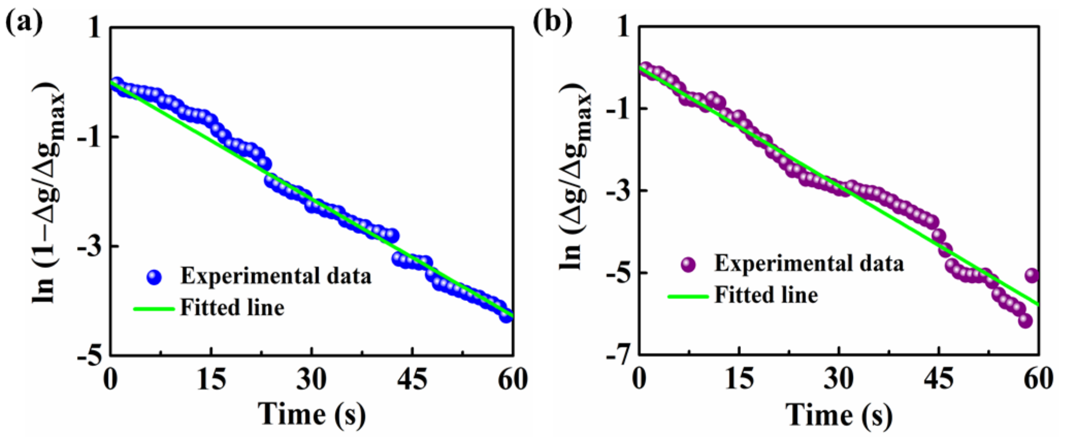

Figure 3.8: Plot (a) shows the Langmuir adsorption model (fitted line) with experimental data, and Plot (b) shows the Langmuir desorption model (fitted line) with experimental data.

3.4 Conclusions

We have reported a highly sensitive resistive sensor for the detection of low-level CO gas at room temperature with MWCNT-PDDA composite as the sensing material. The conductance of the sensors changes due to transfer of charge from CO to the positively charged quaternary ammonium group available on PDDA. The sensors are able to detect very low CO concentrations ranging from 1 to 20 ppm at room temperature. The sensors have shown high sensitivity with fast response and recovery time for CO sensing with LOD of 127 ppb. The influence of temperature and humidity on the sensors has been parametrically studied. The performance of the MWCNT-PDDA based CO sensor improves at elevated temperature up to 100 ℃. The selectivity, stability, and repeatability analysis of the sensors have been reported. Further, the Langmuir adsorption/desorption model has also been studied to understand the sensing mechanism of the CO gas sensor. The device shows excellent potential for rapid CO gas sensing. The sensor can be developed on flexible substrates as portable CO sensor for air quality monitoring in indoor like underground garages, tunnels, engine repair shops, etc. as well as in industrial applications such as chemical, medical and food industries.

References

[1] V. Schroeder, S. Savagatrup, M. He, S. Lin, and T. M. Swager, *Chem. Rev.*, 119 (1), 599-663, 2019.

[2] R. Sinha, N. Roy, R. Rajasekhar, A. Karnawat, and T. K. Mandal, *J. Environ. Chem. Eng.*, 9 (1), 104971, 2021.

[3] A. Mirzaei, J.-H. Lee, S. M. Majhi, M. Weber, M. Bechelany, H. W. Kim, and S. S. Kim, *J. Appl. Phys.*, 126 (24), 241102, 2019.

[4] V. D. N. Bezzon, T. L. A. Montanheiro, B. R. C. de Menezes, R. G. Ribas, V. A. N. Righetti, K. F. Rodrigues, and G. P. Thim, *Adv. Mater. Sci. Eng.*, 2019, 4293073, 2019.

[5] J. F. Fennell Jr, S. F. Liu, J. M. Azzarelli, J. G. Weis, S. Rochat, K. A. Mirica, J. B. Ravnsbæk, and T. M. Swager, *Angew. Chem., Int. Ed.*, 55 (4), 1266-1281, 2016.

[6] A. A. Yaqoob, H. Ahmad, T. Parveen, A. Ahmad, M. Oves, I. M. I. Ismail, H. A. Qari, K. Umar, and M. N. Mohamad Ibrahim, *Front. Chem.*, 8 (341), 2020.

[7] S. Xie, W. Li, Z. Pan, B. Chang, and L. Sun, *J. Phys. Chem. Solids*, 61 (7), 1153-1158, 2000.

[8] R. Shamsi, M. Mahyari, and M. Koosha, *J. Appl. Polym. Sci.*, 134 (10), 2017.

[9] S. Park, M. Vosguerichian, and Z. Bao, *Nanoscale*, 5 (5), 1727-1752, 2013.

[10] D. W. H. Fam, A. I. Y. Tok, A. Palaniappan, P. Nopphawan, A. Lohani, and S. G. Mhaisalkar, *Sens. Actuators, B*, 138 (1), 189-192, 2009.

[11] E. H. Espinosa, R. Ionescu, C. Bittencourt, A. Felten, R. Erni, G. Van Tendeloo, J. J. Pireaux, and E. Llobet, *Thin Solid Films*, 515 (23), 8322-8327, 2007.

[12] Z. Zanolli, R. Leghrib, A. Felten, J.-J. Pireaux, E. Llobet, and J.-C. Charlier, *ACS Nano*, 5 (6), 4592-4599, 2011.

[13] H. Hu, T. Zhang, S. Yuan, and S. Tang, *Adsorption*, 23 (1), 73-85, 2017.

[14] P. L. Gai, O. Stephan, K. McGuire, A. M. Rao, M. S. Dresselhaus, G. Dresselhaus, and C. Colliex, *J. Mater. Chem.*, 14 (4), 669-675, 2004.

[15] R. Tang, Y. Shi, Z. Hou, and L. Wei, *Sensors*, 17 (4), 882, 2017.

[16] C. Liu, I. Sergeichev, I. Akhatov, and K. Lafdi, *Compos. Sci. Technol.*, 159, 111-118, 2018.

[17] J. Sein Anand, D. Schetz, W. Waldman, and M. Wiśniewski, *PLoS One*, 12 (1), e0170621-e0170621, 2017.

[18] S. Zhuiykov, *Sens. Actuators, B,* 129 (1), 431-441, 2008.

[19] K. Mahendraprabhu, A. Selva Sharma, and P. Elumalai, *Sens. Actuators, B,* 283, 842-847, 2019.

[20] K.-C. Hsu, T.-H. Fang, I. T. Tang, Y.-J. Hsiao, and C.-Y. Chen, *J. Alloys Compd.*, 822, 153475, 2020.

[21] G. Neri, A. Bonavita, G. Micali, G. Rizzo, E. Callone, and G. Carturan, *Sens. Actuators, B,* 132 (1), 224-233, 2008.

[22] S. S. Sebt Ahmadi, B. Raissi, R. Riahifar, M. Sahba Yaghmaee, H. R. Saadati, S. Ghashghaie, and M. Javaheri, *J. Electrochem. Soc.*, 162 (11), D3101-D3108, 2015.

[23] T. Goto, T. Itoh, T. Akamatsu, N. Izu, and W. Shin, *Sens. Actuators, B,* 223, 774-783, 2016.

[24] Z. Wang, Y. Li, T. Zhang, J. Hu, Y. Wang, Y. Wei, T. Liu, T. Sun, and K. T. V. Grattan, *IEEE Sens. J.*, 20 (1), 171-177, 2020.

[25] T. Hyodo, T. Goto, T. Ueda, K. Kaneyasu, and Y. Shimizu, *J. Electrochem. Soc.*, 163 (7), B300-B308, 2016.

[26] D. Punetha and S. K. Pandey, *IEEE Sens. J.*, 19 (7), 2450-2457, 2019.

[27] D. N. Oosthuizen, D. E. Motaung, and H. C. Swart, *Appl. Surf. Sci.*, 466, 545-553, 2019.

[28] W. Zeng, Y. Li, B. Miao, L. Lin, and Z. Wang, *Sens. Actuators, B*, 191, 1-8, 2014.

[29] T. Sen, N. G. Shimpi, and S. Mishra, *J. Appl. Polym. Sci.*, 133 (42), 2016.

[30] S. Rasouli Jamnani, H. Milani Moghaddam, S. G. Leonardi, N. Donato, and G. Neri, *Appl. Surf. Sci.*, 487, 793-800, 2019.

[31] H.-J. Lin, H. Gao, and P.-X. Gao, *Appl. Phys. Lett.*, 110 (4), 043101, 2017.

[32] N. Singh, R. K. Gupta, and P. S. Lee, *ACS Appl. Mater. Interfaces*, 3 (7), 2246-2252, 2011.

[33] A. Roy, A. Ray, P. Sadhukhan, K. Naskar, G. Lal, R. Bhar, C. Sinha, and S. Das, *Synth. Met.*, 245, 182-189, 2018.

[34] T. Hojati, M. Ebrahimi, and R. Afzalzadeh, *Mater. Chem. Phys.*, 207, 50-57, 2018.

[35] Y. Guan, F. Liu, B. Wang, X. Yang, X. Liang, H. Suo, P. Sun, Y. Sun, J. Ma, J. Zheng, Y. Wang, and G. Lu, *Sens. Actuators, B*, 239, 696-703, 2017.

[36] S. Demir and M. F. Fellah, *Appl. Surf. Sci.*, 504, 144141, 2020.

[37] N. Roy, S. Mitra, N. M. Das, N. Mandal, D. Bandyopadhyay, H. B. Nemade, and T. K. Mandal, *IEEE Sens. J.*, 20 (5), 2278-2286, 2020.

[38] S. Zhan, D. Li, S. Liang, X. Chen, and X. Li, *Sensors*, 13 (4), 4378-4389, 2013.

[39] G. Frenking, C. Loschen, A. Krapp, S. Fau, and S. H. Strauss, *J. Comput. Chem.*, 28 (1), 117-126, 2007.

[40] M. Zhang, Q. Sun, Z. Yan, J. Jing, W. Wei, D. Jiang, J. Xie, and M. Chen, *Aust. J. Chem.*, 66 (5), 564-571, 2013.

[41] S. Liu and C. Cai, *J. Electroanal. Chem.*, 602, 103-114, 2007.

[42] S. Abdulla, T. L. Mathew, and B. Pullithadathil, *Sens. Actuators, B*, 221, 1523-1534, 2015.

[43] N. M. Vuong, N. D. Chinh, B. T. Huy, and Y.-I. Lee, *Sci. Rep.*, 6 (1), 26736, 2016.

[44] N. M. Vuong, D. Kim, and H. Kim, *Sens. Actuators, B*, 224, 425-433, 2016.

CHAPTER 4

Synthesis of MoS_2-CuO nanocomposite for room temperature acetone gas sensing application

Contents

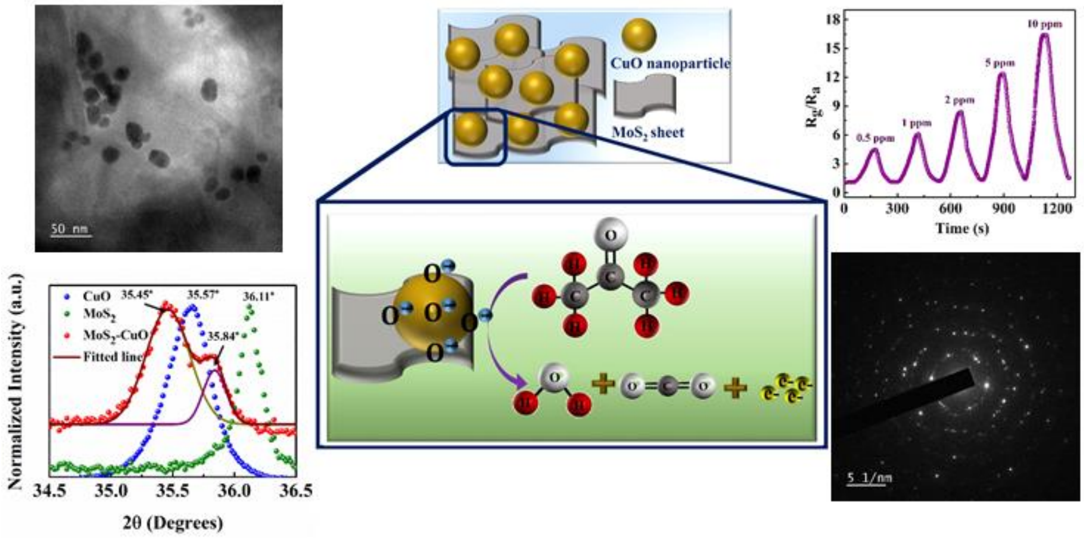

The contents in this chapter have been under review.

Abstract

Rapid and efficient detection of acetone gas at room temperature is of great importance for non-invasive screening of diseases as well as environmental and industrial safety. In this work, we have demonstrated a resistive room temperature acetone gas sensor based on molybdenum disulfide (MoS_2)-copper oxide (CuO) nanocomposites. The morphological and structural characteristics, crystalline nature, and attachment of CuO nanoparticles on MoS_2 nanosheets were investigated using field emission scanning electron microscope (FESEM), energy dispersive X-ray (EDX), field emission transmission electron microscope (FETEM), X-ray diffractometer (XRD), and Raman analysis. The sensing properties of the MoS_2-CuO nanocomposite sensor were investigated systematically by exposing to various acetone gas concentrations at room temperature. It was found that the sensor showed excellent response towards acetone with high sensitivity and fast response and recovery time with detection limit of 93 ppb. Furthermore, the sensor also showed good repeatability, reproducibility and stability at room temperature, and portended enormous potential for real time monitoring of acetone in the fields of health care, environmental, and industrial applications. The probable sensing mechanism of MoS_2-CuO nanocomposite based acetone sensor has been discussed in detail.

4.1 Overview

The salient features of nanomaterial enabled chemiresistive sensors have been discussed in detail in the previous chapters and considered as promising candidates for room temperature portable gas sensing due to their small size, robustness, simplicity, ease of fabrication and integration [1–8]. In this regard, metal oxide semiconductor based sensors have been able to attract attention of researchers because of the prominent features like high chemical stability, cost effectiveness, easy miniaturization, integration, and real-time monitoring [9–11]. In this regard, a variety of metal oxide semiconductors such as zinc oxide (ZnO), copper oxide (CuO), indium oxide (In_2O_3), titanium oxide (TiO_2), tungsten oxide (WO_3), cobalt oxide (Co_3O_4), tin oxide (SnO_2) etc. have been reported for gas sensing application [12–18]. However, sensors based on pristine metal oxide semiconductor usually exhibit low sensitivity, poor selectivity, slow response and recovery and require high operating temperature. In recent times, sensors employing p-n heterojunction metal oxide semiconductor have attracted attention for enhancing the performance of gas sensors by resistance manipulation through controlling the interface potential energy barrier and narrowing the conduction channel [19–21]. CuO is a p-type narrow bandgap metal oxide semiconductor, which shows good stability and high catalytic activity towards gas sensing [22]. Molybdenum disulphide (MoS_2) is an n-type semiconductor, and exhibits excellent properties such as high mobility, high surface to mass ratio, tuneable bandgap, nontoxic, and excellent mechanical strength [23, 24]. Thus, the development of room temperature highly sensitive gas sensor based on heterojunction sensing materials is of great importance in the field of sensors for biomedical, industrial and environmental safety applications.

Human breath analysis is an attractive topic of research as it facilitates rapid, simple, cost effective, and non-invasive early diagnosis of diseases [25–27]. The volatile organic compounds (VOCs) present in exhaled human breath are considered as biomarkers of several diseases, and their excessive presence indicates health disorder [28]. The detection of VOCs is essential in industries, as prolonged exposure to VOCs is harmful to humans and may cause ailments related to lung, nose, eye, kidney, liver, and nervous systems [29, 30]. The efficient and rapid detection of VOCs is essential for early detection of health hazards and industrial and environmental safety. Among VOCs, acetone vapor in human breath is considered as a biomarker for diabetic patients. The acetone vapor in exhaled breath of a healthy person is in the range of 300–900 ppb and exceeds 1800 ppb for diabetic patients [31]. Conventional analytical technique such as gas chromatography mass spectroscopy (GCMS) has been used for acetone gas sensing [32]. However, analytical techniques are expensive and time consuming, involve complex collection and pre-possessing of samples, and require expertise in performing the experiment. Thus, the point-of-care detection of acetone gas is of high importance in healthcare and environmental monitoring.

In this work, we present fabrication and demonstration of a room temperature resistive acetone gas sensor using MoS_2-CuO nanocomposite as a sensing layer. The characteristics of the MoS_2-CuO nanocomposite are investigated by using Raman, FESEM, FETEM, EDX, and XRD analysis. The MoS_2-CuO nanocomposite sensor is exposed to various acetone gas concentrations and systematically investigated the response of the sensor at room temperature. The repeatability, reproducibility, and stability of the sensor are evaluated. In addition, the mechanism of acetone gas sensing by the synthesized MoS_2-CuO nanocomposite sensor is discussed in detail.

4.2 Experimental section

4.2.1 Materials

Molybdenum disulfide (MoS_2), copper (II) nitrate trihydrate ($Cu(NO_3)_2·3H_2O$), copper (II) chloride dihydrate ($CuCl_2·2H_2O$), poly(diallyldimethylammonium chloride) ($(C_8H_{16}NCl)_n$) solution (PDDA), sodium hydroxide (NaOH), silver wire, glass slides, acetone (CH_3COCH_3), methanol (CH_3OH), ethanol (C_2H_5OH), propanol (C_3H_7OH), acetic acid (CH_3COOH), hexane (C_6H_{14}) and toluene (C_7H_8) were procured from Sigma Aldrich, India.

4.2.2 Preparation of materials

The preparation of acetone gas sensing material involved two-step process. Firstly, CuO nanoparticles were synthesized by precipitation method using copper nitrate trihydrate ($Cu(NO_3)_2·3H_2O$) and copper chloride dihydrate ($CuCl_2·2H_2O$). Typically, 0.1 M of $CuCl_2·2H_2O$ and 0.1 M of $Cu(NO_3)_2·3H_2O$ were added to 100 mL of deionized water and stirred for 10 min. Then, 1 M NaOH was added dropwise to the solution and stirred till the precipitation occurred. Afterwards, the solution was stirred and heated at 330 °C till the precipitate turned black. The precipitates were washed thoroughly with deionized water and absolute ethanol several times till the pH of the solution became neutral. Subsequently, the washed precipitates were vacuum dried to get the CuO nanoparticles. Secondly, 4 mg of MoS_2 powder and 2 mg of CuO nanoparticles were dispersed in 2 mL of aqueous PDDA solution (2 %) and stirred for 30 min. Further, the solution was washed with deionized water and centrifuged to obtain the MoS_2-CuO nanocomposite.

4.2.3 Characterization

Raman spectra were recorded on a Horiba LabRam HR Evolution Raman spectrometer. Field emission scanning electron microscopy (FESEM) images were recorded on JEOL JSM-7610F scanning electron microscope. Energy dispersive X-ray (EDX) spectra were recorded using Zeiss, Sigma 300 energy dispersive X-ray spectroscope. Field emission transmission electron microscopy (FETEM) images and selected area electron diffraction (SAED) pattern were recorded on JEOL JEM-2100F transmission electron microscope. The crystallinity of the sample was checked with an X-ray diffractometer (XRD) using Bruker, D8 Advance XRD with Cu-Kα [$\alpha = 1.54$ Å]. All the electrical characterizations of the acetone sensor were carried out with Keithley 4200-SCS semiconductor parameter analyzer at room temperature.

4.2.4 Sensor fabrication and measurement

The acetone gas sensor was fabricated on a clean glass substrate, and silver (Ag) electrodes were patterned on the glass substrate using a shadow mask with the help of a thermal evaporator (Hind High Vacuum, Auto 500). Subsequently, MoS_2-CuO nanocomposite was deposited on the channel region of the sensor by drop casting and dried at 60 °C for 1 hour. The fabrication process steps of the acetone sensor are illustrated in Figure 4.1 (a)–(d), and the optical image of a fabricated acetone sensor is shown in Figure 4.1 (e). The MoS_2-CuO nanocomposite based acetone sensor was placed inside a controlled environment chamber, and the electrical parameters of the sensor were

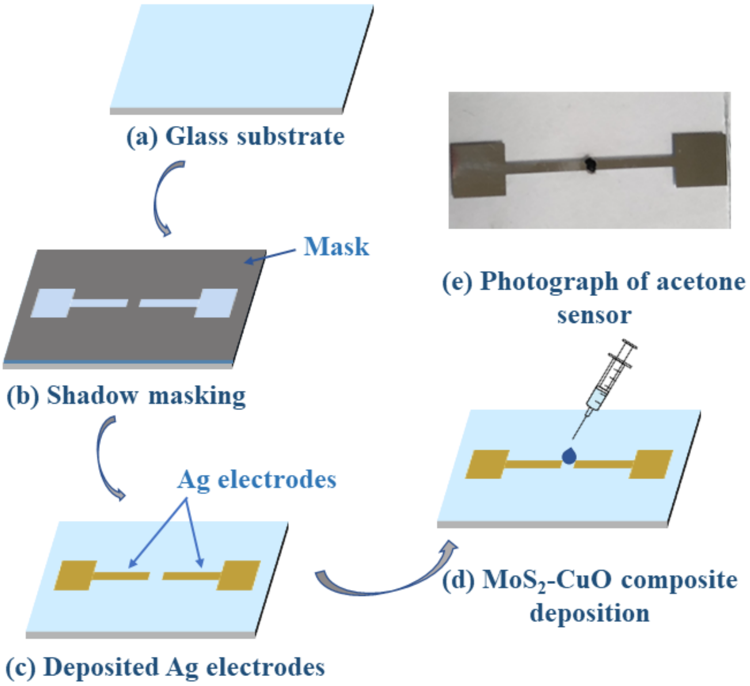

Figure 4.1: (a)–(d) Schematic illustration of the fabrication process of MoS$_2$-CuO nanocomposite based acetone sensor; (e) Optical image of a fabricated acetone sensor.

measured using a sourcemeter. The flow of background gas (nitrogen) was controlled by the mass flow controller (MFC) and the calculated volume of target analyte was loaded in a bubbler connected with the test chamber. The required concentration of the target analyte is calculated by using the following equation [33, 34],

$$C_g = \frac{V_L.\rho_L}{MW.V_C} \text{ x } 2.24 \text{ x } 10^7 \tag{4.1}$$

where C_g is the concentration of acetone gas (ppm), V_L is the volume of liquid analyte (µL) to be injected, and ρ_L is the density of the liquid (g/mL), MW is the molecular weight of liquid analyte (g/mol), and V_C is the volume of the test chamber (mL). The electrical response of the sensor was measured by exposing the sensor to target gas concentrations.

The response of the sensor is calculated by using the equation, $Response = R_g/R_a$, where R_a and R_g are the resistances of the sensor before and after exposure to acetone gas, respectively.

4.3 Results and discussion

4.3.1 Morphological and structural characteristics

Figure 4.2 (a) represents the FESEM image of MoS_2, which displays the stacking pattern of nanoflakes. FESEM images of CuO nanoparticle clusters and MoS_2-CuO nanocomposite are shown in Figure 4.2 (b) and 4.2 (c), respectively. As illustrated in Figure 4.2 (c), it can be observed that CuO nanoparticle clusters are implanted in the MoS_2 nanoflakes. Figure 4.2 (d) represents the scanning area for EDX and elemental mapping of the MoS_2-CuO nanocomposite. The peaks in Figure 4.2 (e) confirm the presence of elements Mo, S, Cu, and O on the composite and the inset shows the weight percentage of these elements. Figure 4.2 (f)–(i) represent the elemental mapping of Mo, S, Cu, and O in the scanning area. Figure 4.3 (a) represents the FETEM image of MoS_2-CuO nanocomposite where black spots can be ascribed to the attachment of CuO nanoparticles on MoS_2 surface. The HRTEM and SAED pattern of the MoS_2-CuO nanocomposite are shown in Figure 4.3 (b) and (c), respectively.

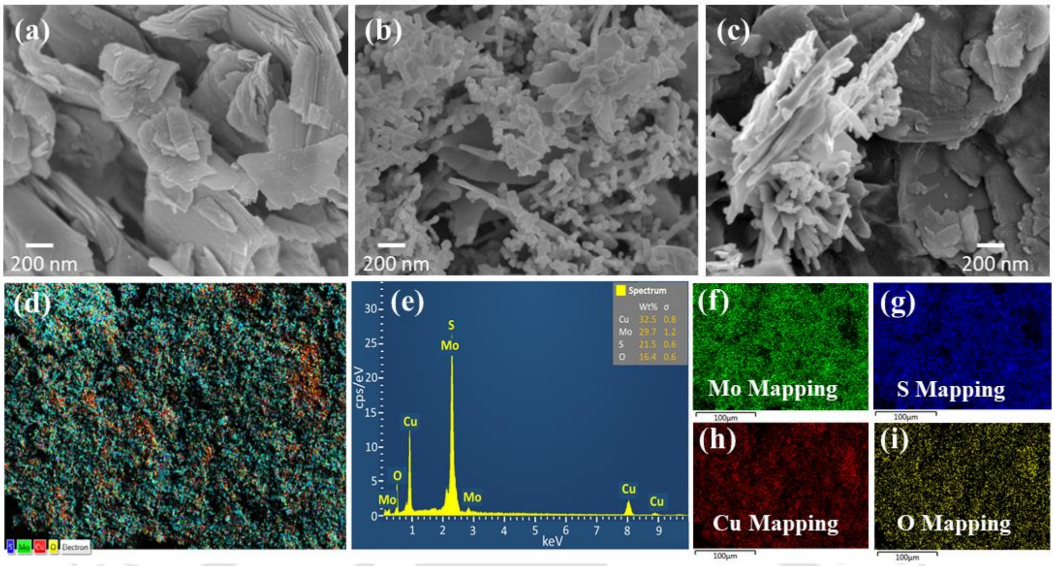

Figure 4.2: FESEM images of (a) MoS_2, (b) CuO, and (c) MoS_2-CuO nanocomposite; (d) Scanning area for EDX analysis, (e) EDX spectrum of the MoS_2-CuO nanocomposite; Mapping images of (f) Mo, (g) S, (h) Cu, and (i) O.

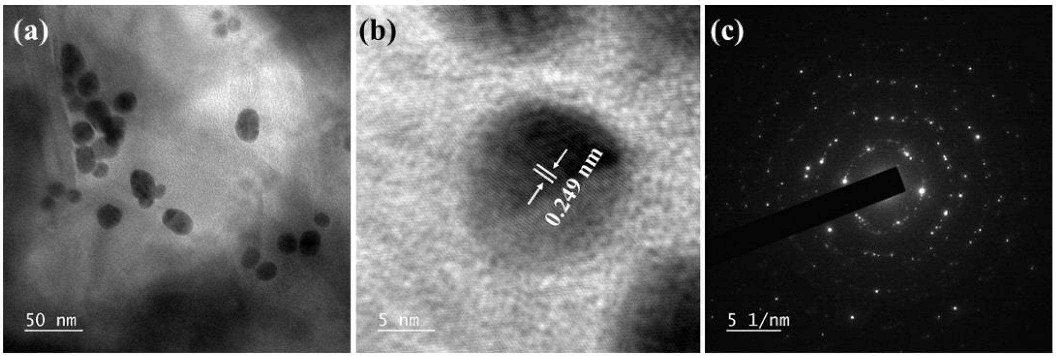

Figure 4.3: (a) FETEM image, (b) HRTEM image, and (c) SAED pattern of the MoS_2-CuO nanocomposite.

Some important information of the synthesized CuO nanoparticle and MoS_2-CuO nanocomposite can be obtained from the Raman spectra shown in Figure 4.4 (a). It is well established that the structure of CuO crystal is monoclinic, and it belongs to the spacegroup of C_{2h}^{6} [35, 36]. In CuO nanocrystals, a total of twelve optically responsive zone centers exist, viz. $4A_u + 5B_u + A_g + 2B_g$. Three out of twelve, i.e. $A_g + 2B_g$ are Raman active [37], where A_g is situated in the near proximity of 300 cm^{-1}, and the two B_gs are situated in the proximities of 350 cm^{-1} and 636 cm^{-1}, respectively. The evidence of peaks near the mentioned wavenumber regions is very much clear in the spectra of both CuO and MoS_2-CuO nanocomposite in Figure 4.4 (a). We have further deconvoluted the Raman spectrum of CuO to get a better understanding and it is shown in Figure 4.4 (b). The peaks at 280 cm^{-1} and 320 cm^{-1} can be assigned to A_g and B_g^1 respectively, whereas the peak at 617 cm^{-1} can be assigned to B_g^2 [37]. The assigned wavenumbers for the peaks are lower than the reported ones, which can be due to the size effects of the particles [36]. In this figure, three more peaks are also observable at 245 cm^{-1}, 603 cm^{-1} and 643 cm^{-1}. Amongst these, the peak at 245 cm^{-1} can be assigned to the one-magnon scattering generated from the antiferromagnetically ordered Cu^{2+} ions [35, 38]. The other two peaks (603 cm^{-1} and 643 cm^{-1}) can be assigned to the two-phonon scattering of the non-zero density of states region in the CuO crystal. Interestingly, the prominent peaks of CuO are still intact in the MoS_2-CuO nanocomposite (Figure 4.4 (a)). However, after deconvolution of the selective peak regions, it is seen that there is a minute but definite redshift of the A_g (282 cm^{-1}) and B_g^1 (336 cm^{-1}) peaks (Figure 4.4 (c)). On the contrary, in B_g^2 peak (582 cm^{-1}), a definite blueshift is observed in Figure 4.4 (d). A similar phenomenon has happened to other peaks due to the two-phonon scattering in the sample. In addition, the peak due to the one-magnon scattering has diminished in the composite material, and a new peak near the 300 cm^{-1} region has appeared, which can be assigned to the B_g^1 corresponding to the phonon vibration of the $2\Gamma_{12}^{-} + \Gamma_{25}^{-}+\Gamma_{2}^{-}$ mode [37]. Moreover, the prominent peaks of MoS_2 (380 cm^{-1} and 406 cm^{-1}) have also shifted left (376 cm^{-1} and 401 cm^{-1}) after the formation of the composite, as seen in Figure 4.4 (a). The shifts in the peaks can also be considered as confirmations about the formation of the nanocomposite (MoS_2-CuO).

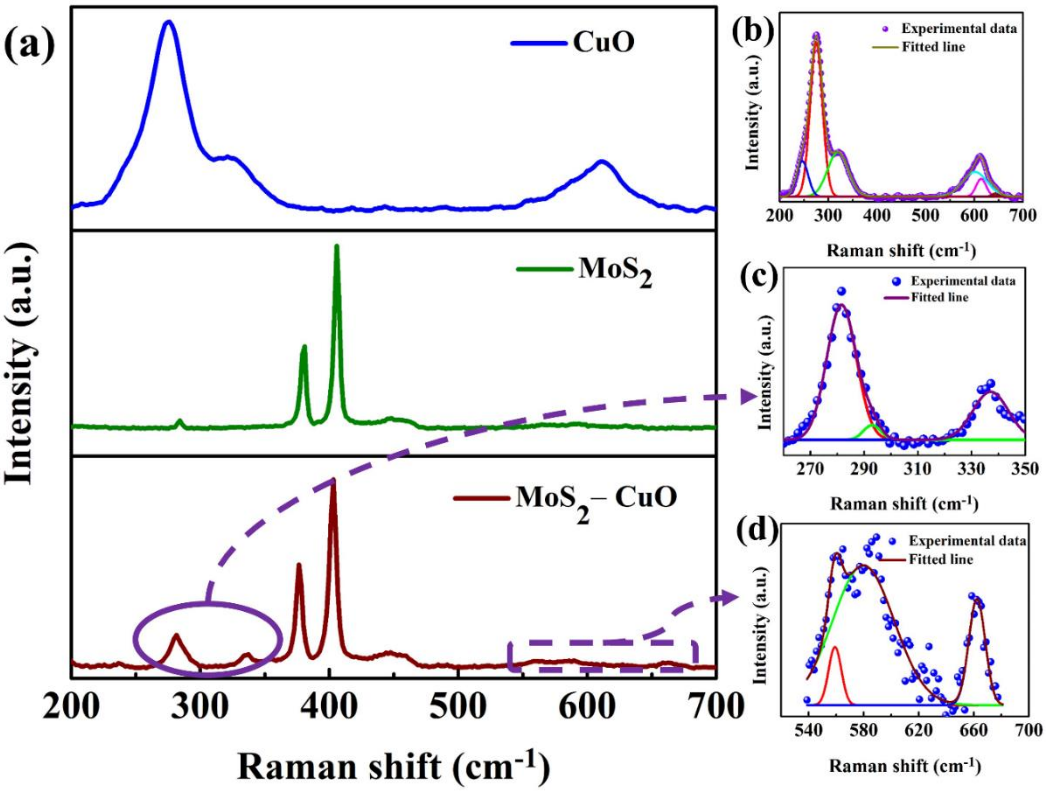

Figure 4.4: (a) Raman Spectra of CuO, MoS_2, and MoS_2-CuO nanocomposite; Deconvoluted peaks of (b) CuO, and (c) & (d) MoS_2-CuO nanocomposite.

The crystalline nature of CuO before and after MoS_2 attachment can be examined from the XRD spectra shown in Figure 4.5 (a). The polycrystalline nature of the synthesized CuO is quite evident by matching the crystalline planes (110), (002), (111), (-202), (020), (-113), (-311), (220), (-312), and (203) at the corresponding 2θ values of 32.58°, 35.57°, 38.9°, 48.98°, 53.37°, 61.8°, 66.3°, 68.14°, 72.3°, and 75.35°, respectively. These results are in good agreement with the results reported by Zhu et al. and Azam et al. [39, 40]. However, it is clear from the figure that the full width at half maximum (FWHM) of the CuO reduces after the attachment with MoS_2 nanosheets. Furthermore, a minute but noticeable shift in the peaks (for both CuO and MoS_2) is observed in the XRD spectrum of the MoS_2-CuO nanocomposite, evident from Figure 4.5 (b) which shows the normalized deconvoluted plots of CuO and MoS_2-CuO nanocomposite expanded around 35.57° corresponding to (002) plane of CuO. Interestingly, the peak corresponding to (102) plane of MoS_2 falls in this region [41], and is included in Figure 4.5 (b). In the case of the composite, a duplet is observed, which conveys the information about the presence of the properties of both CuO and MoS_2. After deconvolution, it is observed that there is a definite blue shift in the peaks of the composite with respect to the pristine materials. This shift can also correspond to the generated strain in the nanocomposite after attachment.

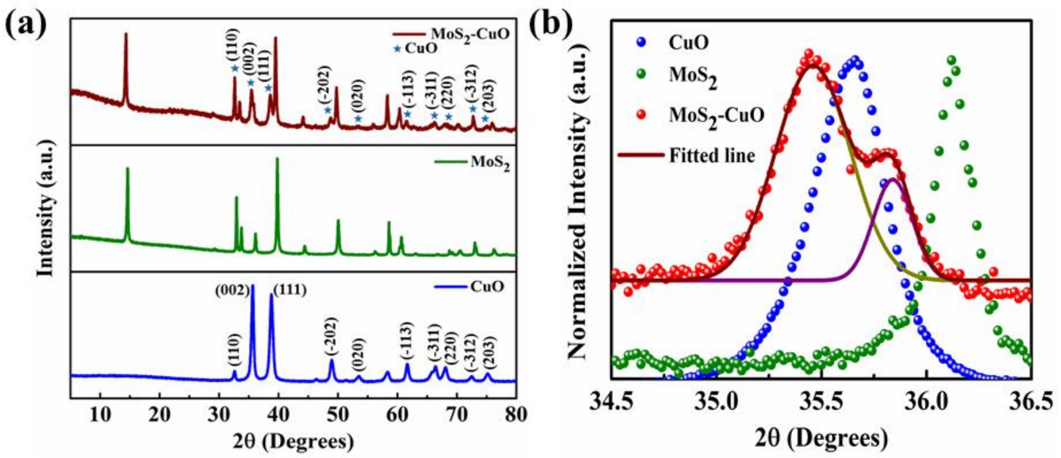

Figure 4.5: (a) XRD pattern of CuO, MoS_2, and MoS_2-CuO nanocomposite, and (b) Normalized deconvoluted peaks of CuO, MoS_2, and MoS_2-CuO nanocomposite expanded around 35.57° corresponding to (002) plane of CuO.

4.3.2 Gas sensing performance

The MoS_2-CuO nanocomposite based sensor was exposed to a wide range of acetone concentrations from 0.5 ppm to 10 ppm at room temperature, and the transient response of the acetone sensor is shown in Figure 4.6 (a). It is observed that the response of the sensor increases with an increase in acetone gas concentration. Figure 4.6 (b) plots the response of the sensor against acetone gas concentration at room temperature. The inset plot of Figure 4.6 (b) demonstrates the response of the sensor for low acetone concentrations in the range of 0.5–2 ppm. The sensor exhibits the response values of 16.21±0.32 and 4.35±0.13 for acetone gas at highest concentration of 10 ppm and lowest concentration of 0.5 ppm, respectively. The sensitivity is calculated from the slope of the curve and limit of detection (LOD) is calculated as, $LOD = 3\sigma_b/Slope$, where σ_b is the standard deviation of the blank sample. The sensitivity and LOD of the acetone sensor are calculated and found to be 2.59 ppm^{-1} and 93 ppb, respectively in the linear range 0.5–2 ppm. The time required for the sensor output to change from 10 % to 90 % of the total response gives the response time on exposure to acetone gas and similarly recovery time after subsequent removal of the gas. Figure 4.6 (c) represents the response and recovery time of the sensor for 0.5 ppm acetone gas concentration. Similarly, response and recovery time are measured for different acetone gas concentrations and shown in Figure 4.6 (d). It is clear from Figure 4.6 (d) that the MoS_2-CuO nanocomposite sensor shows lower response time and larger recovery time at greater concentrations of acetone gas, because a large number of acetone gas molecules are involved in interaction with the sensing material. The sensor exhibited the fastest response time of 61 s and recovery time of 57 s for 10 ppm and 0.5 ppm acetone gas concentrations, respectively.

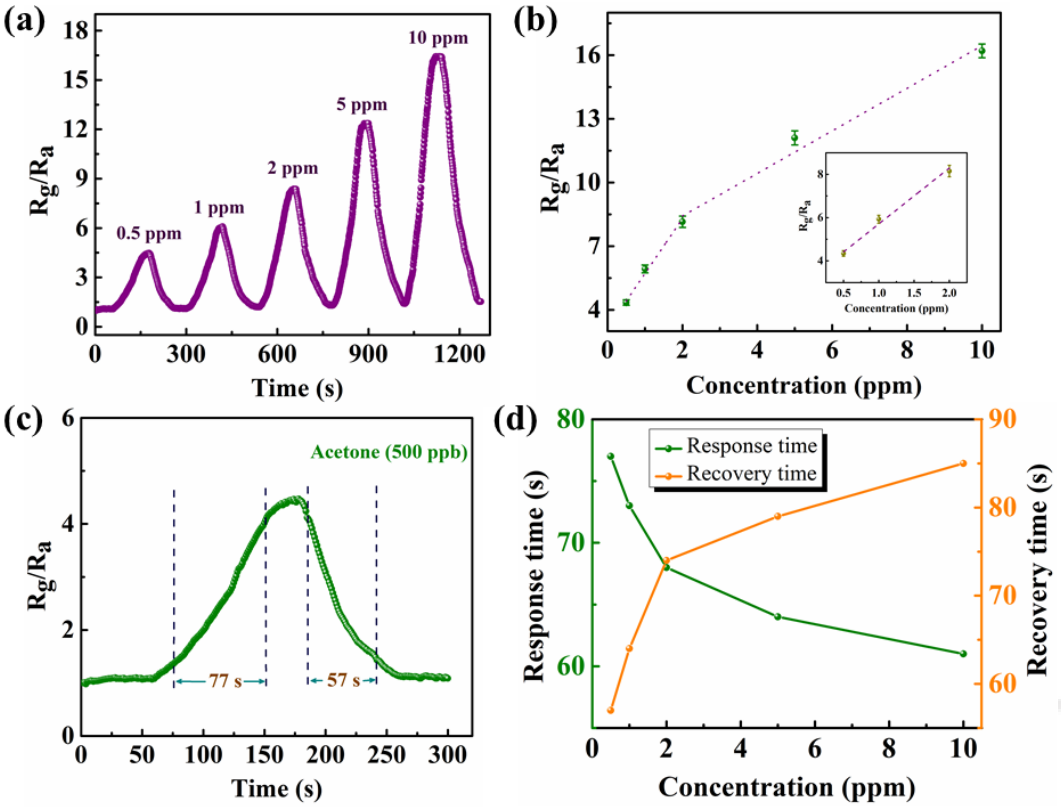

Figure 4.6: (a) Transient response and (b) response versus concentration plot of the sensor towards 0.5–10 ppm acetone gas exposure; (c) Response and recovery time calculation of the sensor for 500 ppb acetone gas; (d) Response and recovery time of the sensor with respect to concentration of acetone gas at room temperature.

The interference of VOCs on sensor performance is evaluated by exposing the sensor to gas having concentration of 10 ppm of each VOC, viz. acetic acid, carbon monoxide, nitric oxide, toluene, propanol, hexane, methanol and ethanol. Figure 4.7 (a) demonstrates the response of the sensor towards VOCs, and suggests that the sensor is highly selective towards acetone. Further, the key performance parameters for the sensor, such as repeatability, reproducibility and stability, are also evaluated by exposing the sensor to acetone gas. Figure 4.7 (b) represents the repeatability analysis of the MoS_2-CuO acetone sensor, where the sensor is exposed to three cycles of 500 ppb of acetone gas, and the decrease in response of the sensor is ~6.2 %. Figure 4.7 (c) demonstrates the reproducibility of the sensor, where three different sensors are prepared in three different batches and exposed to 10 ppm of acetone gas. The stability of the sensor is checked by exposing the same sensor to 10 ppm of acetone gas at an interval of one week for 4 weeks, and the response is plotted in Figure 4.7 (d). The sensor shows excellent stability over a period of time and thus shows excellent viability for acetone gas monitoring at room temperature for practical applications.

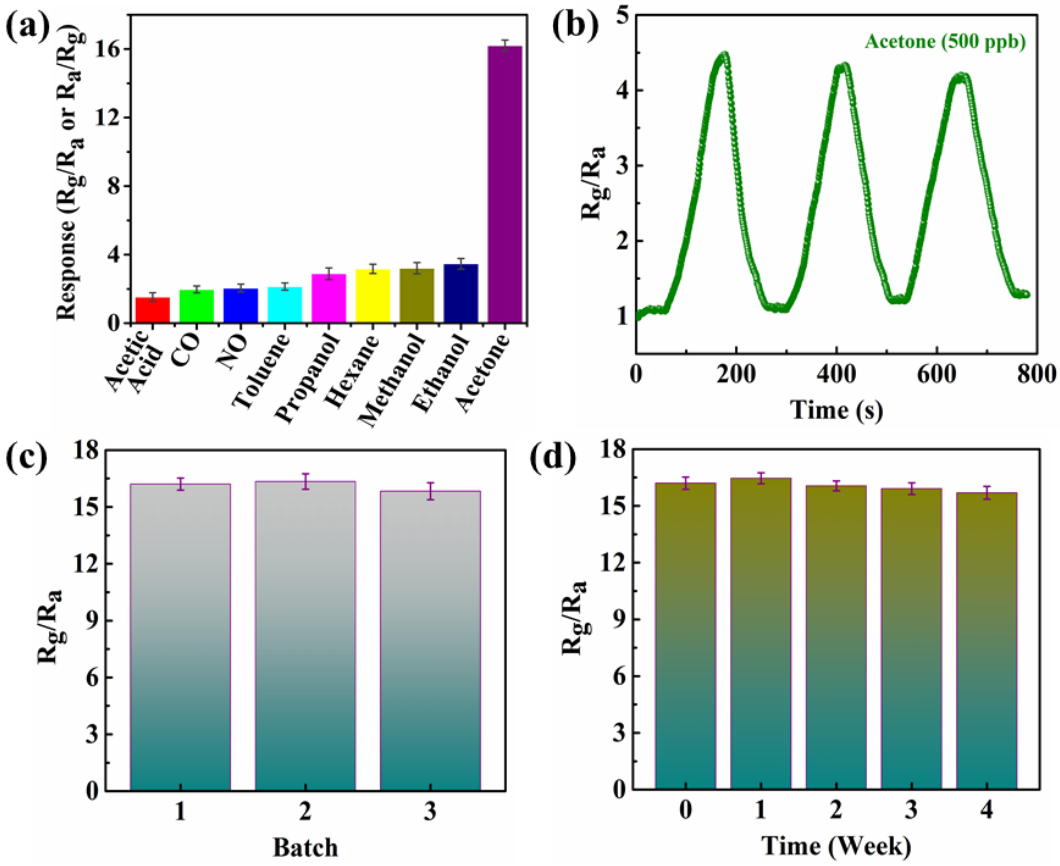

Figure 4.7: (a) Selectivity, (b) repeatability, (c) reproducibility, and (d) stability analysis of the MoS_2-CuO nanocomposite based acetone sensor.

4.3.3 Acetone sensing mechanism

The sensing mechanism can be explained by elucidating the interaction between the acetone molecules with the adsorbed oxygen species on the surface of the CuO nanoparticles. At room temperature, negatively charged oxygen molecules cover the surface of the CuO nanoparticles. This phenomenon helps to generate a hole-accumulation layer on the surface according to the following steps [19].

$$O_{2ads} + e^- \leftrightarrow O_{2ads}^- \tag{4.2}$$

$$O_{2ads}^- + e^- \leftrightarrow 2O_{ads}^- \tag{4.3}$$

$$O_{ads}^- + e^- \leftrightarrow O_{ads}^{2-} \tag{4.4}$$

The adsorbed negatively charged oxygen reacts with acetone and helps the acetone molecules to get oxidized. It can be deemed responsible for the consumption of the hole-accumulation layers. As a result, the conductivity of the CuO nanoparticles is reduced. An overall reaction [19] is shown below, and a pictorial representation of the mechanism is shown in Figure 4.8 (a).

$$C_3H_6O_{gas} + 8O_{ads}^- \leftrightarrow 3H_2O + 3CO_2 + 8e^- \tag{4.5}$$

To understand the phenomenon occurring in the nanocomposite during the above mentioned reactions, which occur at the surface of the CuO nanoparticles, we present the band diagram of the MoS_2-CuO nanocomposite at different reaction conditions. The band structures of CuO and MoS_2 before contact are represented in Figure 4.8 (b). In this figure, E_{vacuum}, E_C, E_F, and E_V refer to the energy levels of vacuum, conduction band, Fermi level, and valance band, respectively. The parameters considered for CuO and MoS_2 respectively

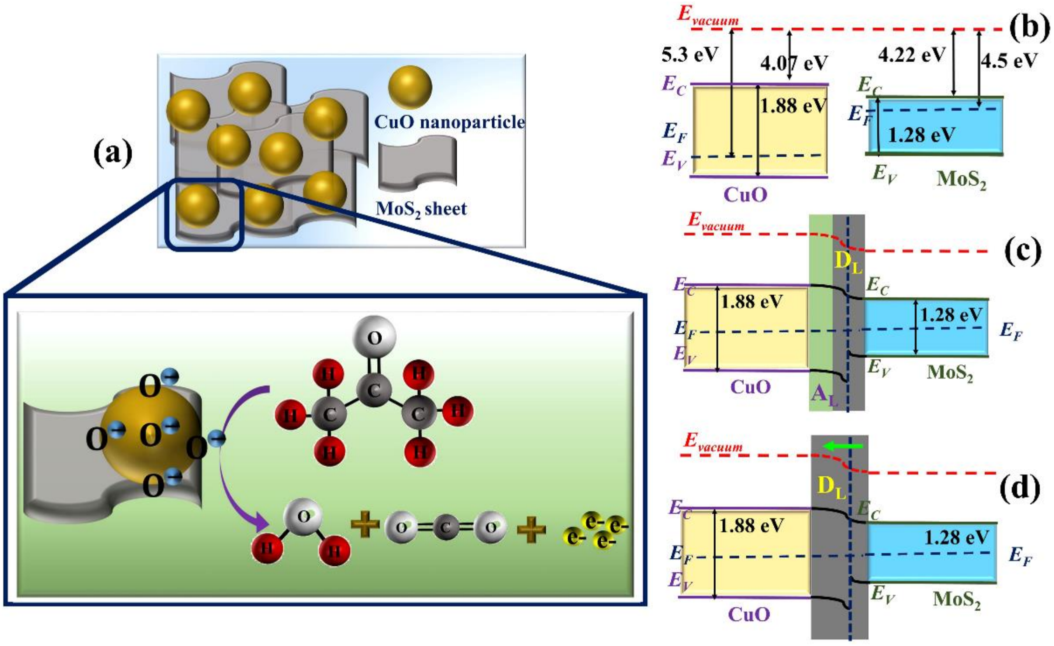

Figure 4.8: (a) Schematic illustration of MoS_2-CuO nanocomposite and acetone gas sensing mechanism (inset), and corresponding band diagram of (b) MoS_2 and CuO before contact, and of MoS_2-CuO nanocomposite (c) in air and (d) in the presence of acetone gas.

are as follows: work function 5.3 eV and 4.5 eV, energy gap 1.88 eV and 1.28 eV, electron affinity 4.07 eV and 4.22 eV [24]. The Fermi levels get flattened (Figure 4.8 (c)) after the two semiconductor materials come in contact with each other as the energies at the junction are equilibrated [24]. Owing to this, a depletion layer (D_L) is generated along with the accumulation layer (A_L) at the junction, as shown in Figure 4.8 (c). These two combined layers act as a potential barrier at the junction and the overall resistance increases. Subsequently, when the acetone (gas) molecules come in contact with the surface of CuO, they consume the oxygen species from the surface and donate electrons, as described in the above equation. It greatly increases the charge concentration at the junction. Consequently, reorganization of charges takes place and the depletion region further expands in the CuO domain as shown in Figure 4.8 (d) causing further increase in the overall resistance through the CuO surface.

4.4 Conclusions

In this study, we have proposed a room temperature acetone gas sensor based on MoS_2-CuO nanocomposite. The structural and morphological characteristics of the MoS_2-CuO nanocomposite sensor were performed through different characterization techniques. The response of the MoS_2-CuO nanocomposite sensor was investigated systematically by exposing it to various acetone gas concentrations. It was found that the sensor exhibits response of 16.21±0.32 and 4.35±0.13 for acetone gas concentrations of 10 ppm and 500 ppb, respectively and a detection limit of 93 ppb at room temperature. Further, the sensor has demonstrated selective response towards acetone and shown good repeatability, reproducibility, and stable sensing performance over a period of time at room temperature. In addition, a probable sensing mechanism of acetone sensing by MoS_2-CuO nanocomposite was also discussed in detail. The sensing performance of the sensor indicates enormous potential for real time acetone gas monitoring for practical applications such as non-invasive healthcare and environmental and industrial safety.

References

[1] N. Roy, R. Sinha, T. T. Daniel, H. B. Nemade, and T. K. Mandal, *IEEE Sens. J.*, 20 (22), 13245-13252, 2020.

[2] J.-F. Feller, N. Gatt, B. Kumar, and M. Castro, *Chemosensors*, 2 (1), 26-40, 2014.

[3] V. Schroeder, S. Savagatrup, M. He, S. Lin, and T. M. Swager, *Chem. Rev.*, 119 (1), 599-663, 2019.

[4] A. Mirzaei, J.-H. Lee, S. M. Majhi, M. Weber, M. Bechelany, H. W. Kim, and S. S. Kim, *J. Appl. Phys.*, 126 (24), 241102, 2019.

[5] T. Sarkar, S. Srinives, S. Sarkar, R. C. Haddon, and A. Mulchandani, *J. Phys. Chem. C*, 118 (3), 1602-1610, 2014.

[6] D. Zhang, A. Liu, H. Chang, and B. Xia, *RSC Adv.*, 5 (4), 3016-3022, 2015.

[7] J. Pan, S. Liu, Y. Yang, and J. Lu, *Nanomaterials*, 8 (6), 2018.

[8] H. Schlicke, M. Rebber, S. Kunze, and T. Vossmeyer, *Nanoscale*, 8 (1), 183-186, 2016.

[9] X. Chang, X. Qiao, K. Li, P. Wang, Y. Xiong, X. Li, F. Xia, and Q. Xue, *Sens. Actuators, B*, 317, 128208, 2020.

[10] Z. Li, H. Li, Z. Wu, M. Wang, J. Luo, H. Torun, P. Hu, C. Yang, M. Grundmann, X. Liu, and Y. Fu, *Mater. Horiz.*, 6 (3), 470-506, 2019.

[11] M. R. Willner and P. J. Vikesland, *J Nanobiotechnol*, 16 (1), 95, 2018.

[12] D. N. Oosthuizen, D. E. Motaung, and H. C. Swart, *Appl. Surf. Sci.*, 466, 545-553, 2019.

[13] W. Liu, X. Zhou, L. Xu, S. Zhu, S. Yang, X. Chen, B. Dong, X. Bai, G. Lu, and H. Song, *Nanoscale*, 11 (24), 11496-11504, 2019.

[14] W. Geng, Z. Ma, Y. Zhao, J. Yang, X. He, L. Duan, F. Li, H. Hou, and Q. Zhang, *Sens. Actuators, B,* 325, 128775, 2020.

[15] X. Liu, K. Zhao, X. Sun, C. Zhang, X. Duan, P. Hou, G. Zhao, S. Zhang, H. Yang, R. Cao, and X. Xu, *Sens. Actuators, B,* 285, 1-10, 2019.

[16] J. Moon, J.-A. Park, S.-J. Lee, T. Zyung, and I.-D. Kim, *Sens. Actuators, B,* 149 (1), 301-305, 2010.

[17] H. Gao, Q. Yu, K. Chen, P. Sun, F. Liu, X. Yan, F. Liu, and G. Lu, *J. Colloid Interface Sci.*, 535, 458-468, 2019.

[18] X. Qiao, C. Ma, X. Chang, X. Li, K. Li, L. Zhu, F. Xia, and Q. Xue, *Sens. Actuators, B,* 327, 128926, 2021.

[19] J. E. Lee, C. K. Lim, H. J. Park, H. Song, S.-Y. Choi, and D.-S. Lee, *ACS Appl. Mater. Interfaces*, 12 (31), 35688-35697, 2020.

[20] F. Shao, M. W. G. Hoffmann, J. D. Prades, R. Zamani, J. Arbiol, J. R. Morante, E. Varechkina, M. Rumyantseva, A. Gaskov, I. Giebelhaus, T. Fischer, S. Mathur, and F. Hernández-Ramírez, *Sens. Actuators, B,* 181, 130-135, 2013.

[21] D. R. Miller, S. A. Akbar, and P. A. Morris, *Sens. Actuators, B,* 204, 250-272, 2014.

[22] D. Gao, J. Zhang, J. Zhu, J. Qi, Z. Zhang, W. Sui, H. Shi, and D. Xue, *Nanoscale Res. Lett.*, 5 (4), 769, 2010.

[23] K. Y. Ko, J.-G. Song, Y. Kim, T. Choi, S. Shin, C. W. Lee, K. Lee, J. Koo, H. Lee, J. Kim, T. Lee, J. Park, and H. Kim, *ACS Nano*, 10 (10), 9287-9296, 2016.

[24] S. Sharma, A. Kumar, N. Singh, and D. Kaur, *Sens. Actuators, B,* 275, 499-507, 2018.

[25] X. Sun, K. Shao, and T. Wang, *Anal. Bioanal. Chem.*, 408 (11), 2759-2780, 2016.

[26] Y. Y. Broza and H. Haick, *Nanomedicine*, 8 (5), 785-806, 2013.

[27] S. M. Aghaei, A. Aasi, S. Farhangdoust, and B. Panchapakesan, *Appl. Surf. Sci.*, 536, 147756, 2021.

[28] S. Das and M. Pal, *J. Electrochem. Soc.*, 167 (3), 037562, 2020.

[29] N. Roy, S. Mitra, N. M. Das, N. Mandal, D. Bandyopadhyay, H. B. Nemade, and T. K. Mandal, *IEEE Sens. J.*, 20 (5), 2278-2286, 2020.

[30] G. de Gennaro, G. Farella, A. Marzocca, A. Mazzone, and M. Tutino, *Int. J. Environ. Res. Public Health*, 10 (12), 6273-6291, 2013.

[31] J. Shin, S.-J. Choi, I. Lee, D.-Y. Youn, C. O. Park, J.-H. Lee, H. L. Tuller, and I.-D. Kim, *Adv. Funct. Mater.*, 23 (19), 2357-2367, 2013.

[32] C. Deng, J. Zhang, X. Yu, W. Zhang, and X. Zhang, *J. Chromatogr. B: Anal. Technol. Biomed. Life Sci.*, 810 (2), 269-275, 2004.

[33] Y. V. Kaneti, Z. Zhang, J. Yue, Q. M. D. Zakaria, C. Chen, X. Jiang, and A. Yu, *Phys. Chem. Chem. Phys.*, 16 (23), 11471-11480, 2014.

[34] A. Kalita, S. Hussain, A. H. Malik, N. V. V. Subbarao, and P. K. Iyer, *J. Mater. Chem. C*, 3 (41), 10767-10774, 2015.

[35] H. F. Goldstein, D.-s. Kim, P. Y. Yu, L. C. Bourne, J. P. Chaminade, and L. Nganga, *Phys. Rev. B*, 41 (10), 7192-7194, 1990.

[36] J. F. Xu, W. Ji, Z. X. Shen, W. S. Li, S. H. Tang, X. R. Ye, D. Z. Jia, and X. Q. Xin, *J. Raman Spectrosc.*, 30 (5), 413-415, 1999.

[37] A. Sahai, N. Goswami, S. D. Kaushik, and S. Tripathi, *Appl. Surf. Sci.*, 390, 974-983, 2016.

[38] J. Chrzanowski and J. C. Irwin, *Solid State Commun.*, 70 (1), 11-14, 1989.

[39] D. Zhu, L. Wang, W. Yu, and H. Xie, *Sci. Rep.*, 8 (1), 5282, 2018.

[40] A. Azam, A. S. Ahmed, M. Oves, M. S. Khan, and A. Memic, *Int J Nanomedicine*, 7, 3527-3535, 2012.

[41] S. Sathiyan, H. Ahmad, W. Y. Chong, S. H. Lee, and S. Sivabalan, *IEEE Photonics J.*, 7 (6), 1-10, 2015.

CHAPTER 5

Development of a paper based enzymatic chemiresistor for POC detection of ethanol in human breath

Contents

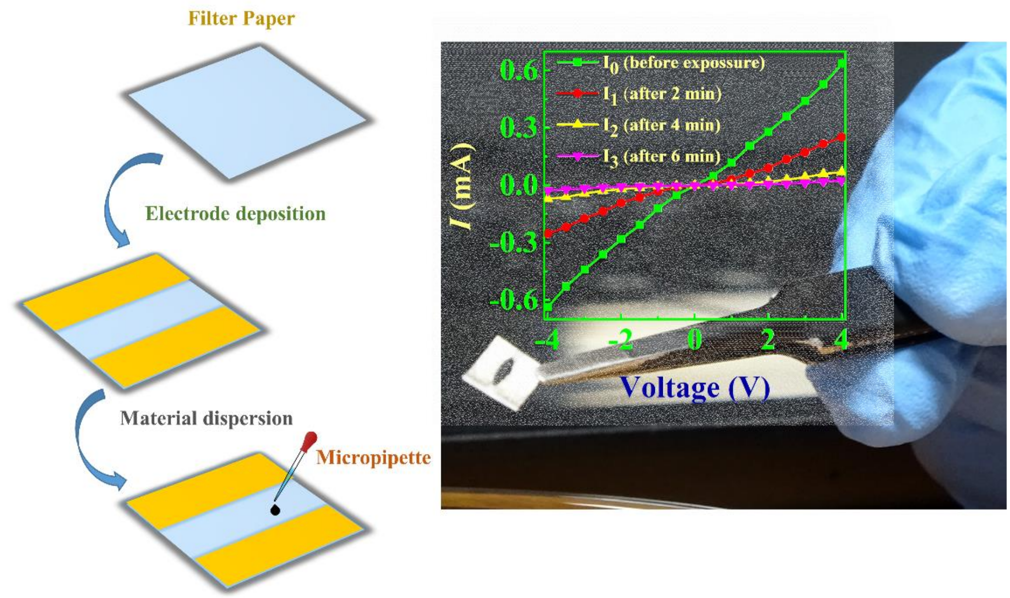

The contents in this chapter have been published in *IEEE Sensors Journal*. 20 (5), 2278-2286 (2020).

Abstract

A paper based chemiresistor has been fabricated to selectively sense ethanol in human breath. The chemiresistor was composed of a sensing mixture of multiwall carbon nanotubes (MWCNTs), poly(diallyldimethylammonium chloride) solution (PDDA), alcohol dehydrogenase (ADH), and coenzyme (NADH). The aluminum electrode was deposited on the paper surface, followed by drop-casting of the aforementioned sensing mixture. The resistance of the sensors was measured by exposing the same in gas-vapor mixture as well as the sample solution. The surface-modified MWCNTs specifically broke down ethanol present in the gas-vapor mixture or in a solution to generate a quantitative electronic response proportional to the ethanol concentration. Subsequently, the interference of other volatile organic materials was also tested to prove the selectivity and sensitivity of the sensor towards ethanol in the presence of different volatile organic compounds (VOCs). The variation of the resistance during the interaction between sensor and ethanol was also characterized by measuring the surface potential of the channel material under ethanol exposure using Kelvin probe force microscopy (KPFM). The sensor was integrated with a voltage divider circuit, a display, and a microcontroller unit to make a proof-of-concept prototype for the point-of-care (POC) detection of ethanol in human breath.

5.1 Overview

The features of carbon nanotube based chemiresistive sensor have been discussed in detail in the previous chapter and considered to be an excellent sensor candidates due to their diverse mechanical and electrical properties, which often lead to a compact, low power, and portable sensing device [1, 2]. The CNT sensors have decent advantageous over the conventional metal oxide sensors because of less toxicity, room temperature operation, ease of functionalization, higher selectivity and sensitivity, ease of fabrication, and lower energy consumption [3, 4]. In particular, the sensitivity and selectivity of CNT sensors can be modulated through their sidewall functionalization towards targeted materials [5]. A charge-transfer during the adsorption of the molecules to be sensed in the functionalized CNTs causes a significant change in the electrical properties of the CNTs, which is translated for chemical and biosensing applications. In this regard, several surface modification approaches on CNT surface such as low-pressure oxygen plasma treatment, plasma treatment, metal nanoparticles or conducting polymers coating, polymeric composites etc. have been reported for various gas sensing applications [6–11].

Exposure to volatile organic compounds (VOCs) either as indoor or outdoor pollutants cause various ailments ranging from eye, nose, lung, liver, kidney to the central nervous systems [12]. The major sources of VOCs in the air are paints and their solvents, wood additives, aerosol sprays, cleansers and disinfectants, repellents, fuels, and automotive products [13–18]. Since most of the VOCs have a negative impact on the environment and subsequently on human health, point-of-care (POC) detection of them is perhaps the need of the hour [19–22]. For example, portable, inexpensive, and user-friendly VOC detection devices are already in use in the industries like food and beverage, paint, biomedical, pharmaceutical, and oil, among others [23–26]. Apart from industrial gaseous or volatile effluents, VOCs are also present in human breath depending on abnormal metabolism or intoxications [27, 28]. Thus, of late, the POC detection of toxic VOCs in human breath has also become important to measure the quality of human health [29]. Intake of alcoholic beverages can increase the concentration of ethanol in the exhaled air, which is an intoxicated state of health condition. In particular, driving under the influence (DUI) of alcohol has been deemed illegal beyond a permissible breath alcohol concentration (BrAC) of 0.05–0.08 % owing to its fatal accidental consequences across the world [30]. Further, due to its flammable properties, sensing and detection of ethanol vapor are also essential during the large scale production of ethanol and fuel processing [31]. In this direction, of late, sensitive, and specific POC detection of ethanol from a gas-mixture is on high demand owing to its applicability in arresting DUI or fire hazards. A low-cost, portable, and user-friendly device with fast response time is expected to detect ethanol specifically from human breath or air in the presence of other VOCs or gases.

The major challenge in the development of such sensors has been the significantly low concentrations of ethanol in human breath or air [32]. Traditionally, there are a number of centralized and costly analytical techniques such as gas chromatography (GC), spectrophotometry and high performance liquid chromatography (HPLC) have been available for such measurements in an accurate as well as specific manner [33–35]. Of late, employing the principle of micro or nanosciences, a wide range of electrochemical, resistive, gravimetric, or optical sensors have been developed for the detection of VOCs [36–39]. In particular, for alcohol sensing, various inorganic materials have been employed in the sensor architecture, such as zinc oxide (ZnO), Au-doped ZnO nanowires, cadmium oxide (CdO), titanium oxide (TiO_2), vanadium oxide (V_2O_5), indium oxide (In_2O_3) nanowire and so on [40–45].

In view of this background, the target of the present work is to develop a paper based disposable miniaturized biosensor for accurate detection of ethanol in liquid solutions and gas-vapor mixtures. For the sensor development, we employ a chemiresistive architecture owing to its ease of fabrication, low fabrication cost, and biodegradability, as they can be fabricated on a paper substrate. For this purpose, a pair of aluminum electrodes were coated on the paper separated by a channel wherein the composite of MWCNTs, poly(diallyldimethylammonium chloride) solution (PDDA), alcohol dehydrogenase (ADH), and coenzyme (NADH) was deposited. The positively charged PDDA surface facilitated the electrostatic attachment of negatively charged ADH on the MWCNTs. The enzyme ADH specifically broke down ethanol present in the gas-vapor mixture to generate an electronic response across the sensor equivalent to the ethanol loading in the analyte. The interferences of other volatile organic materials were also tested to prove the selectivity and sensitivity of the sensor towards ethanol in the presence of a gas-vapor mixture. The variation of the resistance during the interaction between sensor and ethanol was also characterized by measuring the surface potential of the channel material using atomic force microscopy. The sensor has further been integrated with a voltage divider circuit, an LCD screen, and an open-source microcontroller unit to develop a low-cost, portable, and user friendly point-of-care (POC) detection of ethanol in human breath with fast response and recovery times. The proposed breath analyzer is able to detect the ethanol concentration ~0.01 % (v/v) in a liquid phase, which is well below the value ~0.08 % (v/v) recommended by WHO.

5.2 Experimental section

5.2.1 Materials

Multiwalled carbon nanotubes (purity 98 %, diameter = 6–13 nm, length = 2.5–20 µm), poly(diallyldimethylammonium chloride) ($(C_8H_{16}NCl)_n$) solution, alcohol dehydrogenase (EC 1.1.1.1), β-Nicotinamide adenine dinucleotide sodium salt ($C_{21}H_{26}N_7NaO_{14}P_2$), Whatman filter paper, aluminum wire, ethanol (C_2H_5OH), methanol (CH_3OH), 2-propanol (C_3H_7OH), acetone (C_3H_6O), chloroform ($CHCl_3$), acetic acid (CH_3COOH), and hexane (C_6H_{14}) were procured from Sigma Aldrich (India). Phosphate buffered saline (PBS) was obtained from SRL, India. The Arduino Uno R3 development board, Liquid crystal display (LCD), and resistors were procured from Rhydo Labz, India. The chemicals were of analytical grade and employed in the experiments without further purification. The Milli-Q grade water was used for cleaning and to prepare the solutions.

5.2.2 Preparation of materials

The surface of MWCNTs was functionalized with positively charged PDDA. Typically, 3 mg MWCNTs were dispersed in 1 mL of aqueous PDDA solution with 10 min ultrasonication before stirring for 3 h at room temperature [46]. MWCNT-PDDA nanocomposite was collected by centrifuging for 10 min. The composite obtained was washed with deionized (DI) water to remove loosely attached PDDA from the MWCNTs surface. Thereafter, ADH was attached to the surface of MWCNT-PDDA nanocomposite via electrostatic interactions. For this step, typically, 15 mg ADH was added in 1 mL PBS containing 2 mg of MWCNT-PDDA composite, and the solution was then stirred for 10 h at 4 °C. The MWCNT-PDDA-ADH nanocomposites were washed and collected by centrifugation for 10 min. Each step of surface modification of MWCNTs mentioned above was characterized by Fourier transform infrared (FTIR) and Raman spectroscopy. Different ethanol concentration solutions from 0.01–0.20 % (v/v) were prepared by mixing pure ethanol with Milli-Q water. The VOC mixture was prepared by mixing methanol, 2-propanol, acetone, acetic acid, hexane, and chloroform at different proportions in v/v.

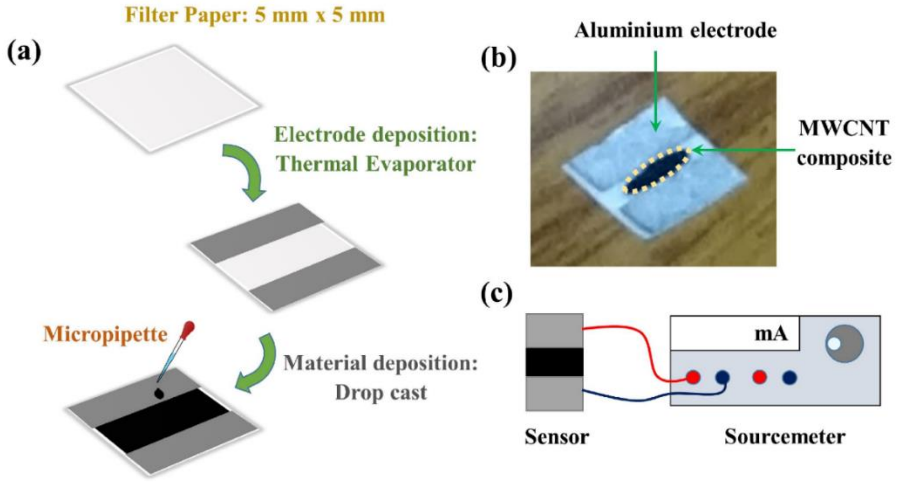

Figure 5.1: Schematic shows the fabrication steps, the fabricated sensor, and the connection of the sensor with a source meter. Image (a) shows sensor fabrication steps, namely electrode deposition, and drop-casting of MWCNT-PDDA-ADH composite as the sensing material. Image (b) shows the top view of the fabricated sensor, and Image (c) shows the sensor connection with a source meter for measurement purposes.

5.2.3 Sensor fabrication

The sketch of the sensor fabrication steps is shown in Figure 5.1 (a). A 5 mm × 5 mm size of Whatman filter was taken, and aluminum electrodes were deposited by thermal evaporation (Hind High Vacuum, Auto 500). The MWCNT-PDDA-ADH solution was deposited on the channel region of the sensor. Typically, 10 µL of MWCNT-PDDA-ADH solution was deposited between two aluminum electrodes by drop-casting. Following this, 1.5 mM NADH solution was prepared and dropped above the MWCNT-PDDA-ADH nanocomposite film. The actual image of the developed sensor is given in Figure 5.1(b). The sensor was connected with a source meter (Model 2614B, Keithley, U.S.A.), as shown in Figure 5.1(c) and initial resistance was measured without the sample solution. Thereafter, 5 µL of alcohol solution was put on the sensor, and resistance was measured. The variation in the resistance of the sensors was studied at different concentrations of ethanol solutions. The measurements were repeated five times for each concentration, and the average value was reported.

5.3 Results and discussion

5.3.1 Sensor characteristics

The FTIR spectroscopy (Thermo Scientific Nicolet iS10 FTIR spectrometer, U.S.A.) has been used to characterize each step of surface modification of MWCNTs. Figure 5.2 (a) shows the FTIR spectra of MWCNTs (Figure 5.2 (a) (i)), PDDA (Figure 5.2 (a) (ii)), MWCNT-PDDA (Figure 5.2 (a) (iii)), ADH (Figure 5.2 (a) (iv)) and MWCNT-PDDA-ADH (Figure 5.2 (a) (v)). The appearance of a peak at 1632 cm^{-1} in Figure 5.2 (a) (i) is due to the stretching of the C=C bond presence the carbon skeleton of MWCNTs [47]. The appearance of peaks at 2901 cm^{-1} and 2831 cm^{-1} in PDDA (Figure 5.2 (a) (ii)) is attributed to the stretching vibrations bands of the groups CH_2 and CH_3, respectively. The peaks at 1638 cm^{-1}, 1473 cm^{-1} and 1339 cm^{-1} in PDDA are appeared due to the presence of C=C bond, CH_2 bending, and C-N bonds, respectively [46]. The PDDA adsorption on the surface of MWCNTs is confirmed by the appearance of the peaks at 2873 cm^{-1}, 2808 cm^{-1} and 1471 cm^{-1} of MWCNT-PDDA composite (Figure 5.2 (a) (iii)). The vibration bands of amide-I and amide-II of ADH appear at 1631 cm^{-1} and 1540 cm^{-1}, respectively (Figure 5.2 (a) (iv)). The adsorption of ADH on MWCNT-PDDA composite is confirmed by the appearance of the vibration band of amide II at 1542 cm^{-1} (Figure 5.2 (a) (v)).

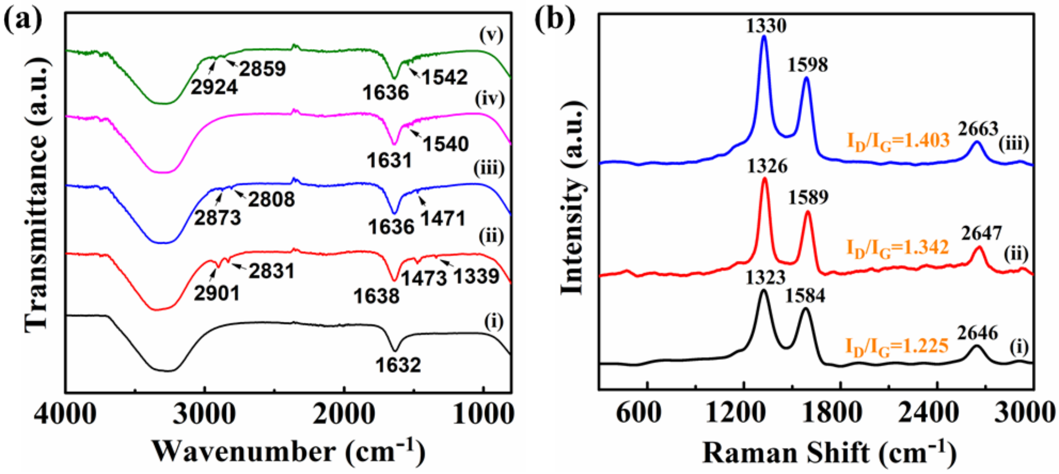

Figure 5.2: Characterization of the modified MWCNTs at different stages of preparation. Image (a) shows FTIR spectra of MWCNTs (i), PDDA (ii), MWCNT-PDDA composite (iii), ADH (iv) and MWCNT-PDDA-ADH composite (v). Image (b) shows Raman spectra of MWCNTs (i), MWCNT-PDDA composite (ii) and MWCNT-PDDA-ADH composite (iii).

Raman spectroscopy (Horiba LabRam HR Evolution Raman spectrophotometer, U.S.A.) is used to confirm the probable interactions between MWCNTs and PDDA in each step of the fabrication process. Figure 5.2 (b) shows the Raman spectra of MWCNTs (Figure 5.2 (b) (i)), MWCNT-PDDA (Figure 5.2 (b) (ii)) and MWCNT-PDDA-ADH (Figure 5.2 (b) (iii)). The appearance of a prominent peak at 1323 cm^{-1} (D band) is attributed to disorder in sp^2 carbons available on the surface of MWCNTs and peak at 1584 cm^{-1} (G band) is corresponding to the sp^2 vibration of carbon atoms on the graphitic surface of MWCNTs [48–50]. After the adsorption of PDDA on the surface of MWCNTs, the D band and G band of spectra shifts from (1323–1326) cm^{-1} and (1584–1589) cm^{-1} respectively (Figure

5.2 (b) (ii)), which confirms the functionalization of PDDA on the MWCNTs surface. After the functionalization of ADH on MWCNT-PDDA surface, the D band and G band further shifts from (1326–1330) cm^{-1} and (1589–1598) cm^{-1}, respectively (Figure 5.2 (b) (iii)) [46]. Another evidence for this functionalization is the increase in I_D/I_G ratio in the Raman spectrum [51, 52]. The calculated I_D/I_G for MWCNTs, MWCNT-PDDA, and MWCNT-PDDA-ADH is 1.225, 1.342 and 1.403, respectively. Functionalization of PDDA on MWCNTs surface creates more defects on the surface of MWCNTs, thus the I_D/I_G ratio increases and as we functionalized further with ADH the ratio increases further.

5.3.2 Sensor performance

The I-V analysis of the sensor was carried out before and after exposure to ethanol at different time intervals such as 2 min, 4 min, and 6 min. It was observed that the current was maximum when the sensor was not exposed to ethanol and as exposure time increased, the current reduced further, as shown in Figure 5.3 (a). The transient current response of the sensor towards ethanol exposure is shown in Figure 5.3 (b). The reduction of sensor current occurred due to a series of reactions through which ethanol oxidized to acetaldehyde in the following manner,

$$\mathrm{CH_3CH_2OH + NAD^+ \xleftrightarrow{ADH} CH_3CHO + NADH + H^+} \tag{5.1}$$

$$\mathrm{NADH \xrightarrow{\quad\quad} NAD^+ + H^+ + 2e^{-1}} \tag{5.2}$$

The electrons produced by the reactions reduce the conductance of the channel material as MWCNTs was originally p-type material and subsequently the current of the sensor reduced.

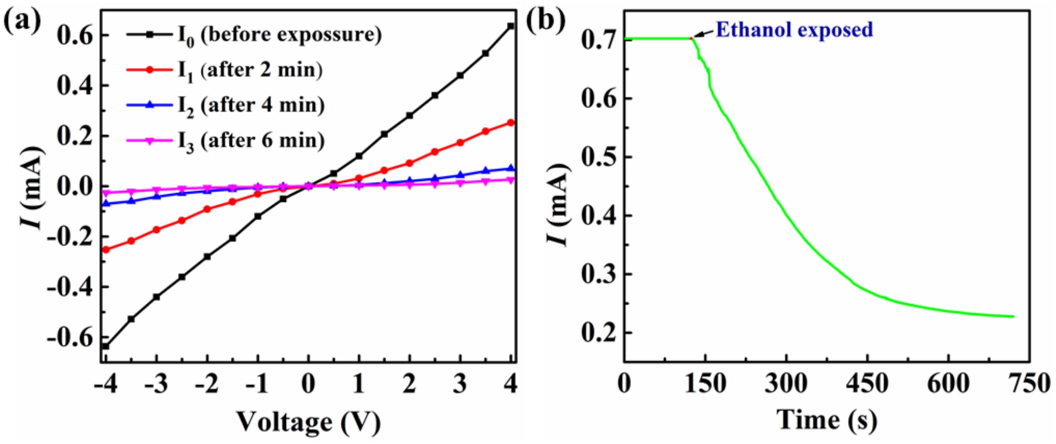

Figure 5.3: Plot (a) shows I-V analysis of the sensor before and after exposure to ethanol for different time duration and plot (b) shows transient current response of sensor upon exposure to 0.08 % (v/v) ethanol concentration at a fixed voltage of 3.3 V.

In order to carry out sensitivity analysis, different ethanol concentrations were prepared ranging from 0.01 % to 0.20 % (v/v). The calibration curve was obtained from the measured values of the current flowing through the channel of the sensor. Figure 5.4 (a) shows the response (S) of the sensor upon exposure to different ethanol concentrations. The sensor response was calculated by using the equation,

$$S = \frac{\Delta R}{R_0} = \frac{R_f - R_0}{R_0} \qquad (5.3)$$

where R_0 and R_f are the resistances of the sensor before and after exposure to ethanol, respectively. Linear regression analysis is used to determine the slope, the regression coefficient (R^2) and intercepts. The sensor showed a good linear response ($R^2 = 0.965$) upon exposure of different ethanol concentrations (0.01 % to 0.20 % (v/v)). The limit of detection (LOD) of the sensor could be calculated by using the equation,

$$LOD = 3 \times \frac{Standard\ deviation\ of\ blank\ sample}{Slope} \qquad (5.4)$$

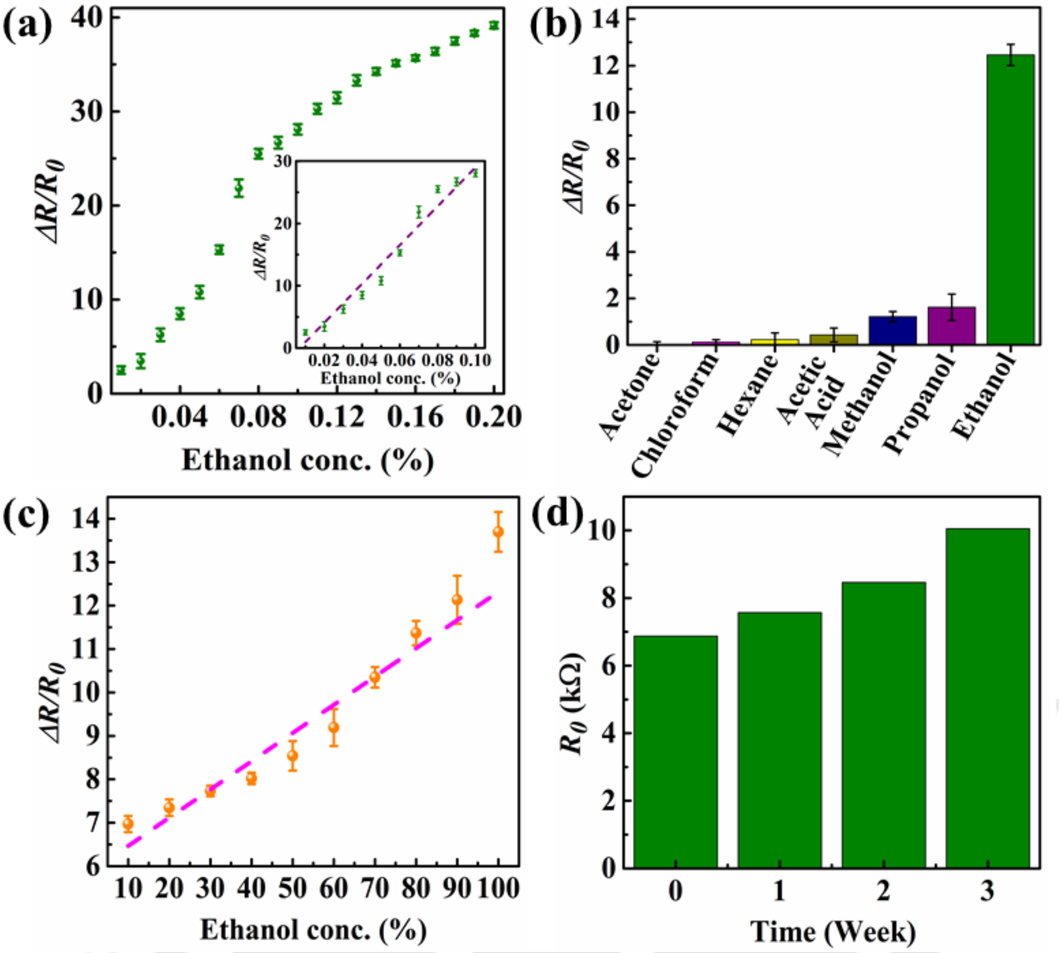

Figure 5.4: (a) Response of the MWCNT-PDDA-ADH sensor towards different ethanol concentrations in aqueous solution and the inset plot is a linear fit for ethanol concentration from 0.01 % to 0.10 % (v/v); Response of the sensor towards (b) vapors of different VOC's and (c) ethanol vapors at varying concentrations in the presence of a mixture of different VOCs; (d) The change of the base resistance of the chemiresistive sensor taken at different time intervals (1, 7, 14, and 21 days) after fabrication at room temperature.

The measured LOD of the sensor determined from the calibration curve is 0.00071 % (v/v). In order to check the selectivity, the sensor was exposed to different VOCs such as acetone, chloroform, hexane, acetic acid, methanol, 2-propanol, and ethanol individually under the same investigating conditions. During the study, it was found that the sensor showed an excellent selectivity towards ethanol vapor, as compared to other VOCs shown in Figure 5.4 (b). The results demonstrated that the sensor could be a good candidate for alcohol breathe analyzer. Further, we performed another experiment to examine whether the prepared sensors were capable to detect ethanol vapors under the interference of a mixture of different VOCs. Here, acetone, chloroform, hexane, acetic acid, methanol, and 2-propanol were used to prepare VOCs mixture. The sensor was exposed to VOC mixture vapor in presence of ethanol concentration varying from 10–100 % (v/v). The sensor response was calculated for each case and the calibration plot has been shown in Figure 5.4 (c). Linear regression analysis is used to determine the slope, the regression coefficient (R^2) and intercepts. The sensor showed a good linear response ($R^2 = 0.922$) under exposure to VOC mixture vapor with different ethanol concentrations (10–100 % (v/v)). The LOD of the sensor determined from the calibration curve was found to be 1.41 % (v/v).

The stability of any sensor is an important property, as far as the usability of the product by the end users. Stability also influences the base resistance and sensitivity of the sensor, which play an important role in determining the quick response of the sensors. Although the sensitivity is defined by the normalized resistance of the fabricated sensor, the base resistance should not be changed much with time in order to make it a marketable end user product. We took the base resistance of a specific sensor at every 7-day interval, till 21 days and the same is plotted in Figure 5.4 (d). It was observed that a marginal change of base resistance took place with the progress in time. However, the variation was not that significant, which could affect the normalized resistance data to a considerable extent. It may also be noted here that, as enzymes are very prone to decomposition at a temperature higher than 45 ℃ and so, the sensors are always kept in a low temperature of ~4 ℃ inside the refrigerator. In such storage conditions, sensors did not show considerable change of resistivity, selectivity and sensitivity. Moreover, the sensors could retain their properties at ambient temperature for around ~48 h after they were withdrawn from the cold environment.

5.3.3 Surface potential measurements

Surface potential (SP) measurement of the sensor was carried out with the help of Kelvin Probe Force Microscopy (KPFM) (Bruker, Innova series, USA) in order to comprehend the distribution of the surface charge on the channel before and after the exposure of alcohol vapor. The main aim of this study was to decipher the science behind the resistive response of the sensor after exposure to alcohol vapor. A modulation voltage of 2 V was applied between the cantilever and the sample surface to attain a resonance frequency of cantilever in order to map the surface potential over the device surface. A Pt/Ir AFM tip has been used for the experiment whose work function has been optimized by using the known work function of a highly oriented pyrolytic graphite (HOPG) surface. The tips were used for measuring the surface potential where the KPFM gave the contact potential difference (CPD) between the work function of the tip (ϕ_{tip}) and the work function of the material (ϕ_{sample}). We could quantitatively measure the surface potential by applying the following equation,

$$CPD = (\emptyset_{tip} - \emptyset_{sample})/e \tag{5.5}$$

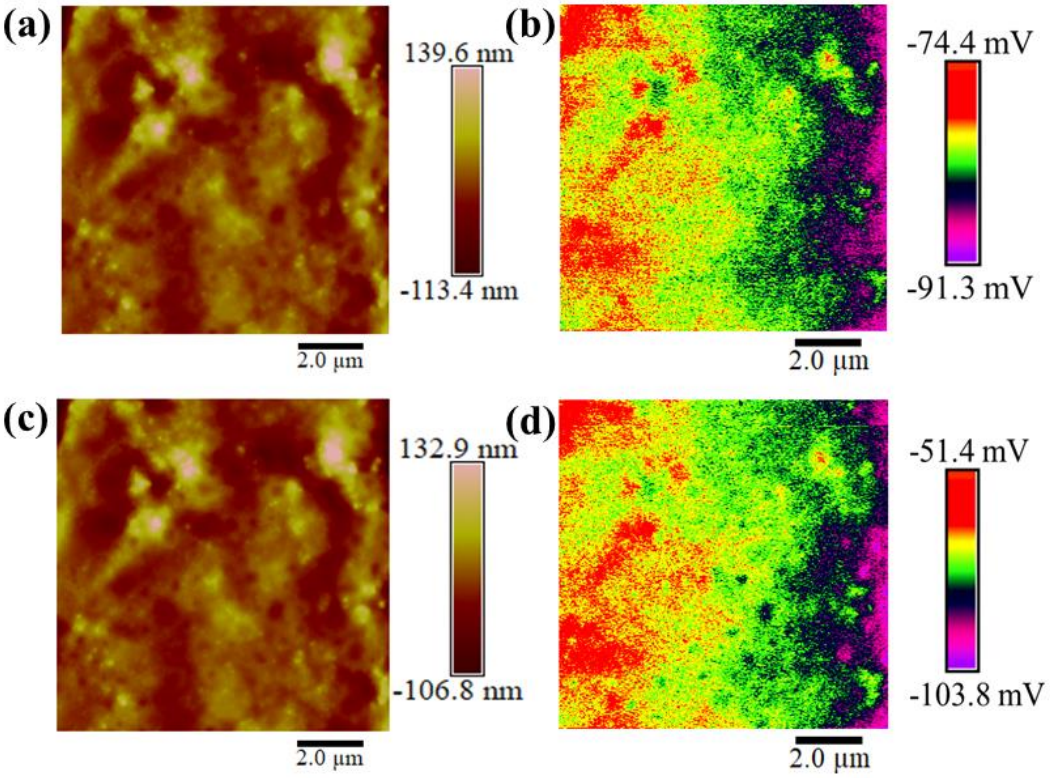

Figure 5.5: Images (a) and (c) denote the topographies of the composite sample before and after the exposure of the alcohol vapors. Images (b) and (d) denote the corresponding Surface Potential Microscopy (SPIOM) images before and after the exposure of alcohol vapors.

where, *e* is the elementary electronic charge. The surface potential was experimentally measured by the null method, which was compensated by a potential feedback circuit. We could get the surface topography and potential images at the same time to corroborate the reliability the site-specific measurement of surface charges. It may be noted here that in these experiments, the same area was chosen for scanning before and after the exposure of alcohol vapor. The ADH-PDDA wrapped MWCNTs showed a negative SP as MWCNTs are a p-type semiconductor, and PDDA has quaternary ammonium ions in its molecular structure. Figure 5.5 (a) shows the distribution of the surface charge of the bare alcohol sensor before exposure to alcohol. The acquired KPFM data were processed by the NanoScope Analysis 1.5 software without further modifying the raw data. It was observed that the CPD attained values in the range of -91.3 mV to -74.4 mV, which led to an average CPD of the surface to be approximately -16.9 mV. After exposure to alcohol, we scanned the same area immediately. It was observed that the exposure of alcohol mitigated the surface charge over the sensor area, and the CPD values were found to be varying from -103.8 mV to -51.4 mV.

Alternatively, the average CPD of the surface after the exposure was found to be nearly -52.4 mV. The results accounted for a change of ±35.5 mV of the CPD values before and after the exposure of the alcohol. With the help of a freshly prepared HOPG sample, the Pt/Ir AFM tip confirmed a work function of ~4.56 eV. Therefore, by using the Eq. (3), the respective work function of the material surface before and after the exposure of the alcohol vapor was estimated to be ~4.58 eV and ~4.61 eV, respectively. These values also justified the variation of the surface potential after the exposure of alcohol vapors. The change was due to the reactive interaction between the gas and the surface of the channel material of the device. The overall electronic interaction caused the surface charge to get changed, and thus, the sensor showed a variation in resistance on alcohol exposure. Mitigation of surface charge was a clear indication of a reduction of charge carriers available on the surface of the sensor. A change in the surface potential leads to the change in resistance of the chemiresistive sensor, which has been attributed to Figure 5.3.

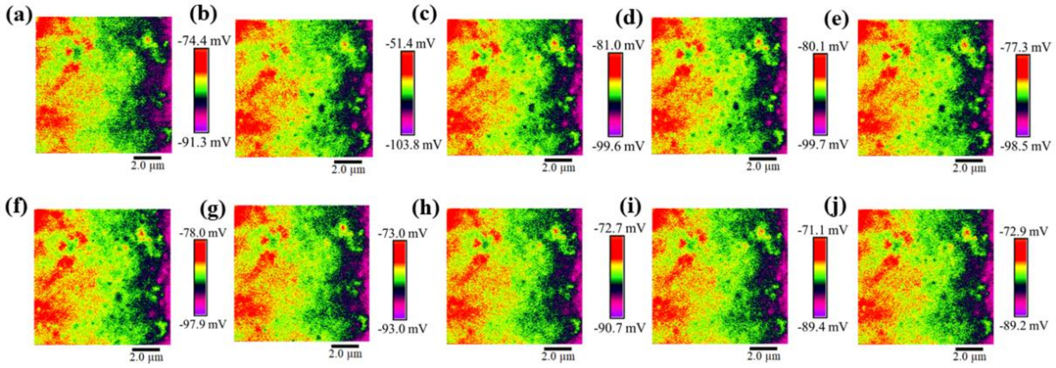

Figure 5.6: KPFM maps showing sensitivity kinetics of ADH-PDDA wrapped MWCNTs before and after exposure to alcohol vapor. (a) shows the initial value before exposure to alcohol vapors. (b–j) show the kinetics of sensitivity just after the exposure of alcohol vapors. Each KPFM map was taken while maintaining 256 number of line scans and 1 Hz of scan frequency.

Further continuing with the experiment, we carried out the kinetics of variation of contact potential differences (V_{CPD}) above the surfaces of ADH-PDDA wrapped MWCNTs before and after the exposure of alcohol vapors. Figure 5.6 shows the kinetics of the change of the surface charge, as measured by the KPFM. The experiment was carried out with 9 steps (as charge saturation was attained after 9 steps) of repetitive scans after the exposure of alcohol vapors. Fixing scan parameters such as keeping 256 lines scans at about 1 Hz of scan frequency, took us about 4 minutes and 30 seconds of time for each image scan. As shown in Figure 5.5, after 30 seconds of alcohol exposure, we started recording the data immediately. The KPFM image, just after the exposure showed a drastic variation in V_{CPD} (Figure 5.6 (b)), which gradually settled to a value close to the value recorded before the exposure (Figure 5.6 (j)). The initial variation of the surface charges might be attributed to the accumulation of free charges due to reactive interaction at the gas and surface interface, and the subsequent decay in the surface charges might be due to the charge neutralization because of the presence of free ions in the atmosphere. The periodical changes of V_{CPD} and attaining a saturation value ±16.3 mV at the end of 9 steps (Figure 5.6 (j), low to high difference) close to the initial measurement (Figure 5.6 (a)) led to the prevalence of lag phase in sensitivity of the device. More importantly, this behavior allowed one to use the same device for another set of data measurements and hold a good prospect of repeatability.

5.3.4 Breath analyzer

The different components and electronic circuits of the breath analyzer prototype are shown in Figure 5.7. Figure 5.7 (a) shows the setup and the connections of the sensor. The position of the sample container and the demonstration of the circuit after exposure of alcohol vapor on the sensor are depicted in Figure 5.7 (b). The internal circuitry of the device presented in Figure 5.7 (c) explains the functioning mechanism of the developed prototype. The integrated circuit with the paper based sensor works on voltage divider principle using the sensor as a variable chemiresistor (9), as shown in Figure 5.7 (c). The integrated electronic circuit with the paper-based alcohol sensor is composed of the following components, namely (i) Arduino UNO R3 microcontroller board, (ii) the LCD, and (iii) a voltage divider circuit made on a breadboard. The two resistors which were used in making the voltage divider circuit are R1 (the variable chemiresistor or the paper based alcohol sensor) and known resistor R2 (100 kΩ). One end of the alcohol sensor was connected with a supply voltage (5 V) while the other resistor terminal was grounded, as shown in Figure 5.7 (c) of the main manuscript. The microcontroller had an integrated 10-bit analog to digital converter (ADC) for digitizing the analog inputs. The analog input from the sensor was given to the analog input through pin A0 on the Arduino UNO R3 development board (4 in Figure 5.7 (c)), and the output was displayed on the LCD unit.

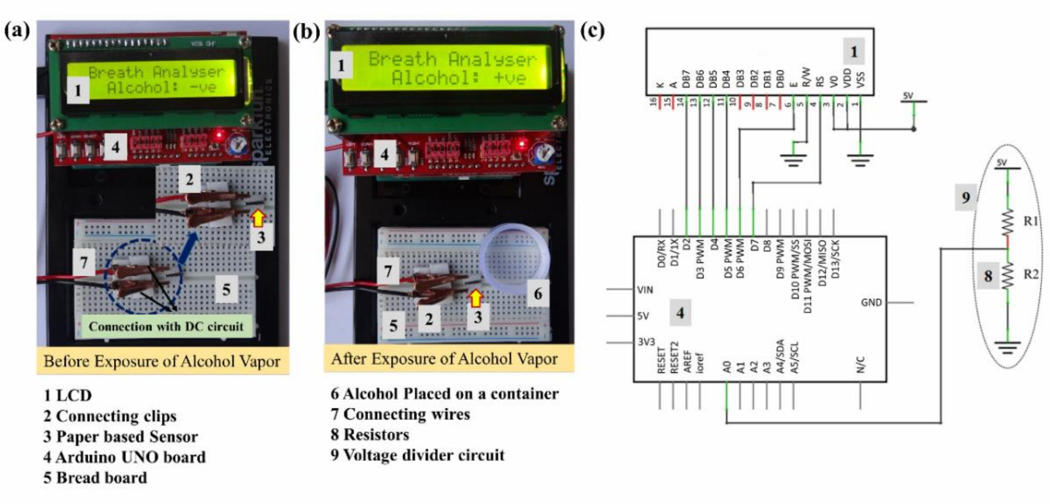

Figure 5.7: Photograph (a) shows the breath analyzer prototype consisting of LCD (1), connection clips (2), paper based alcohol sensor (3), Arduino UNO (4), breadboard (5), and connecting wires (7). (b) shows the live setup after exposing the alcohol vapor coming from the sample container (6). (c) shows the connections of LCD and voltage divider circuit (9) with the Arduino UNO (4). The LCD (1) shows positive and negative response indicating the presence and absence of ethanol.

It was observed that, upon the exposure of alcohol vapor on the sensor, the resistance increased as ethanol is oxidized under the influence of ADH. Subsequently, the normalized resistance increased, as discussed in the Section 5.3.1, and the same had been programmed with the help of Arduino UNO microprocessor board in such a way, that on the exposure of the alcohol vapor the LCD showed the message ‘Alcohol: + ve’. Further, for the detection of alcohol in human breath, we have performed a breath analysis of two different volunteers to check the feasibility of the breath analyzer for real samples. For the demonstration of breath analyzer in human breath, the breath analyzer displays a message

'Alcohol: + ve' for the volunteer who has consumed alcohol, and it shows 'Alcohol: - ve' for the volunteer who has not consumed alcohol.

5.4 Conclusions

We report the development of a low-cost, disposable, sensitive, and selective paper based chemiresistive sensor for the ultrafast detection of ethanol from a gas-vapor mixture or a solution. The channel material of the sensor was composed of a mixture containing surface-modified MWCNTs and coenzyme (NADH), which made the sensor very selective towards ethanol in the gas-vapor mixture. The variations in the surface charge during the exposure of the ethanol has been characterized by the KPFM. The sensor could detect alcohol concentration even below 0.01 % (v/v) in a vapor mixture, which is found to be much lower than that found in human breath after the consumption of alcohol. The details of the stability, specificity, and selectivity statistics have been parametrically reported as sensor statistics. The paper based sensor is further integrated with a voltage divider circuit, a display, an open-source microcontroller unit to make a proof-of-concept prototype for sensitive and selective POC detection of ethanol in human breath.

References

[1] R. Tang, Y. Shi, Z. Hou, and L. Wei, *Sensors*, 17 (4), 882, 2017.

[2] V. D. N. Bezzon, T. L. A. Montanheiro, B. R. C. de Menezes, R. G. Ribas, V. A. N. Righetti, K. F. Rodrigues, and G. P. Thim, *Adv. Mater. Sci. Eng.*, 2019, 4293073, 2019.

[3] J.-F. Feller, N. Gatt, B. Kumar, and M. Castro, *Chemosensors*, 2 (1), 26-40, 2014.

[4] M. Leidinger, T. Sauerwald, T. Conrad, W. Reimringer, G. Ventura, and A. Schütze, *Procedia Eng.*, 87, 1449-1452, 2014.

[5] H. Hu, T. Zhang, S. Yuan, and S. Tang, *Adsorption*, 23 (1), 73-85, 2017.

[6] E. H. Espinosa, R. Ionescu, C. Bittencourt, A. Felten, R. Erni, G. Van Tendeloo, J. J. Pireaux, and E. Llobet, *Thin Solid Films*, 515 (23), 8322-8327, 2007.

[7] C. Chen, A. Ogino, X. Wang, and M. Nagatsu, *Appl. Phys. Lett.*, 96 (13), 131504, 2010.

[8] D. W. H. Fam, A. I. Y. Tok, A. Palaniappan, P. Nopphawan, A. Lohani, and S. G. Mhaisalkar, *Sens. Actuators, B*, 138 (1), 189-192, 2009.

[9] S. Sharma, S. Hussain, S. Singh, and S. S. Islam, *Sens. Actuators, B*, 194, 213-219, 2014.

[10] S. Middya, M. Bhattacharjee, and D. Bandyopadhyay, *Nanotechnology*, 30 (14), 145502, 2019.

[11] Z. Zanolli, R. Leghrib, A. Felten, J.-J. Pireaux, E. Llobet, and J.-C. Charlier, *ACS Nano*, 5 (6), 4592-4599, 2011.

[12] G. de Gennaro, G. Farella, A. Marzocca, A. Mazzone, and M. Tutino, *Int. J. Environ. Res. Public Health*, 10 (12), 6273-6291, 2013.

[13] D. Hu and K. C. Hornbuckle, *Environ. Sci. Technol.*, 44 (8), 2822-2827, 2010.

[14] L. Kuai, J. Geng, C. Chen, E. Kan, Y. Liu, Q. Wang, and B. Geng, *Angew. Chem.*, 126 (29), 7677-7681, 2014.

[15] B. Liu, D. Chen, W. Zhou, N. Nasr, T. Wang, S. Hu, and B. Zhu, *J. Cleaner Prod.*, 194, 309-317, 2018.

[16] S. Deshmukh, S. Patil, S. Mullani, and S. Delekar, *Mater. Sci. Eng. C*, 97, 954-965, 2018.

[17] G. Min Shi, L. Hao, K. Anderson, and T.-S. Chung, *Ind. Eng. Chem. Res.*, 56, 13791-13799, 2017.

[18] M. Schaub, L. Jenni, and F. Bairlein, *Behav. Ecol.*, 19 (3), 657-666, 2008.

[19] M. H. Zarifi, A. Sohrabi, P. M. Shaibani, M. Daneshmand, and T. Thundat, *IEEE Sens. J.*, 15 (1), 248-254, 2015.

[20] J.-K. Chen, J.-H. Wang, C.-J. Chang, and C.-F. Huang, *Sens. Actuators, B*, 188, 1123-1131, 2013.

[21] T. Endo, Y. Yanagida, and T. Hatsuzawa, *Sens. Actuators, B*, 125 (2), 589-595, 2007.

[22] X. Zhu, H. Zhang, and J. Wu, *Sens. Actuators, B*, 202, 105-113, 2014.

[23] B. Eklund and T. P. Nelson, *J. Air & Waste Manage. Assoc.*, 45 (3), 196-205, 1995.

[24] J. Schuberth, *Anal. Chem.*, 68 (8), 1317-1320, 1996.

[25] Y. Chang, N. Tang, H. Qu, J. Liu, D. Zhang, W. Pang, and X. Duan, *Sci. Rep.*, 6, 23970, 2016.

[26] S. Matindoust, M. Baghaei-Nejad, H. Shahrokh Abadi Mohammad, Z. Zou, and L.-R. Zheng, *Sens. Rev.*, 36 (2), 169-183, 2016.

[27] M. Bhattacharjee, H. B. Nemade, and D. Bandyopadhyay, *Biosens. Bioelectron.*, 94, 544-551, 2017.

[28] M. Bhattacharjee and D. Bandyopadhyay, *Sens. Actuators, A*, 285, 241-247, 2019.

[29] O. Lawal, W. M. Ahmed, T. M. E. Nijsen, R. Goodacre, and S. J. Fowler, *Metabolomics*, 13 (10), 110-110, 2017.

[30] E. Bihar, Y. Deng, T. Miyake, M. Saadaoui, G. G. Malliaras, and M. Rolandi, *Sci. Rep.*, 6, 27582-27582, 2016.

[31] A. Mirzaei, S. G. Leonardi, and G. Neri, *Ceram. Int.*, 42 (14), 15119-15141, 2016.

[32] A. Daneshkhah, S. Shrestha, M. Agarwal, and K. Varahramyan, *Sens. Actuators, B*, 221, 635-643, 2015.

[33] P. Vesely, L. Lusk, G. Basarova, J. Seabrooks, and D. Ryder, *J. Agric. Food Chem.*, 51 (24), 6941-6944, 2003.

[34] L. S. G. Teixeira, E. S. Leão, A. l. F. Dantas, H. s. L. C. Pinheiro, A. C. S. Costa, and J. B. de Andrade, *Talanta*, 64 (3), 711-715, 2004.

[35] P. J. Sabourin, W. E. Bechtold, and R. F. Henderson, *Anal. Biochem.*, 170 (2), 316-327, 1988.

[36] M. Penza, G. Cassano, P. Aversa, A. Cusano, M. Consales, M. Giordano, and L. Nicolais, *IEEE Sens. J.*, 6 (4), 867-875, 2006.

[37] J. Gębicki, A. Kloskowski, and W. Chrzanowski, *Sens. Actuators, B*, 177, 1173-1179, 2013.

[38] X. Wang, S. Hou, H. Goktas, P. Kovacik, F. Yaul, A. Paidimarri, N. Ickes, A. Chandrakasan, and K. Gleason, *ACS Appl. Mater. Interfaces*, 7 (30), 16213-16222, 2015.

[39] Y. Chen, H. Zhang, Z. Feng, H. Zhang, R. Zhang, Y. Yu, J. Tao, H. Zhao, W. Guo, W. Pang, X. Duan, J. Liu, and D. Zhang, *ACS Appl. Mater. Interfaces,* 8 (33), 21742-21749, 2016.

[40] P. Shankar and J. B. B. Rayappan, *J. Mater. Chem. C,* 5 (41), 10869-10880, 2017.

[41] N. Hongsith, C. Viriyaworasakul, P. Mangkorntong, N. Mangkorntong, and S. Choopun, *Ceram. Int.*, 34 (4), 823-826, 2008.

[42] A. S. Kamble, R. C. Pawar, J. Y. Patil, S. S. Suryavanshi, and P. S. Patil, *J. Alloys Compd.*, 509 (3), 1035-1039, 2011.

[43] M. Mabrook and P. Hawkins, *Sens. Actuators, B,* 75 (3), 197-202, 2001.

[44] J. Liu, X. Wang, Q. Peng, and Y. Li, *Adv. Mater.*, 17 (6), 764-767, 2005.

[45] C. Xiangfeng, W. Caihong, J. Dongli, and Z. Chenmou, *Chem. Phys. Lett.*, 399 (4), 461-464, 2004.

[46] S. Liu and C. Cai, *J. Electroanal. Chem.,* 602 (1), 103-114, 2007.

[47] M. Zhang, Q. Sun, Z. Yan, J. Jing, W. Wei, D. Jiang, J. Xie, and M. Chen, *Aust. J. Chem.*, 66 (5), 564-571, 2013.

[48] L. Bokobza and J. Zhang, *eXPRESS Polym. Lett.*, 6 (7), 601 - 608, 2012.

[49] M. Eising, C. E. Cava, R. V. Salvatierra, A. J. G. Zarbin, and L. S. Roman, *Sens. Actuators, B,* 245, 25-33, 2017.

[50] S. Abdulla, T. L. Mathew, and B. Pullithadathil, *Sens. Actuators, B,* 221, 1523-1534, 2015.

[51] F. M. Machado, C. P. Bergmann, E. C. Lima, M. A. Adebayo, and S. B. Fagan, *Mat. Res.*, 17, 153-160, 2014.

[52] P. Kaur, M.-S. Shin, A. Joshi, N. Kaur, N. Sharma, J.-S. Park, and S. S. Sekhon, *J. Phys. Chem. B*, 117 (11), 3161-3166, 2013.

CHAPTER 6

Summary and Future scope

Contents

6.1 Summary

In summary, the present thesis takes advantage of the salient features of nanomaterials by employing them in sensor technology for various applications. The thesis aims to develop affordable, compact, low cost, and robust nanomaterial enabled chemiresistor devices for various sensing applications, including healthcare, food processing, agriculture, and environmental monitoring. The first chapter provides a brief overview of various sensor technologies, sensor architectures, and sensing nanomaterials.

In the second chapter, we discuss the development of a nanomaterial based chemiresistive sensor to quantify urea concentration in an aqueous solution. The sensor consists of a pair of silver (Ag) electrodes deposited on a glass substrate and surface modified multiwall carbon nanotubes (MWCNTs) composite as the sensing material. The surface of MWCNTs was functionalized using the oxidation of MWCNTs, followed by the attachment of the thiol group on the surface of MWCNTs. The thiol functionalized MWCNTs were used as a conducting channel between the electrodes, and the starch coated gold nanoparticles (S-AuNPs) layer provides the platform for starch-urea reaction. The change in electrical resistance was measured based on starch-urea interaction for different urea concentrations, and the influence of other milk adulterants was also performed. The stability and reproducibility of the urea sensor were examined for the feasibility of its commercial potential. Further, the standard addition and spike-recovery methods were used to detect urea in the raw milk sample.

The third chapter illustrates the fabrication of a room temperature carbon monoxide (CO) sensor based on MWCNT-poly(diallyldimethylammonium chloride) solution (MWCNT-

PDDA) composite. Interdigitated electrodes (IDEs) were deposited on glass substrates, and MWCNT-PDDA composite was used as a sensing material. The sensing performance of the MWCNT-PDDA composite was determined for various CO gas concentrations. The effect of temperature and humidity on the sensors was investigated, and the influence of other interfering gases was also explored. We discussed the sensing mechanism of the CO gas sensor based on the adsorption/desorption model, and the experimental results confirmed the Langmuir adsorption/desorption model.

In the fourth chapter, we discuss the fabrication of a room temperature acetone gas sensor based on molybdenum disulfide (MoS_2)-copper oxide (CuO) nanocomposite. The sensor consists of Ag electrodes deposited on a glass substrate and MoS_2-CuO nanocomposite as the sensing material. The MoS_2-CuO nanocomposite sensor was exposed to various acetone gas concentrations at room temperature, and the response of the sensor was investigated systematically. The selectivity of the MoS_2-CuO nanocomposite sensor was examined by exposing the sensor towards various interfering gases and volatile organic compounds. The repeatability, reproducibility, and stability of the sensor were evaluated. In addition, the mechanism of acetone gas sensing by the synthesized MoS_2-CuO nanocomposite sensor was discussed in detail.

The fifth chapter illustrates the development of a paper based disposable miniaturized sensor for accurate detection of ethanol in liquid solutions and gas-vapor mixtures. The sensor was developed on a paper substrate with alcohol dehydrogenase (ADH) modified MWCNTs as a sensing layer. The sensing performance of the paper based sensor was measured by exposing the sensor towards various ethanol concentrations in the gas-vapor mixture and the sample solution. The interferences of other volatile organic compounds were also examined to prove the selectivity and sensitivity of the sensor towards ethanol in the presence of a gas-vapor mixture. In addition, the variation of the resistance during the interaction between sensor and ethanol was also characterized by measuring the surface potential of the channel material using atomic force microscopy. Further, the sensor was integrated with an electronic circuit to develop a low-cost, portable, and user-friendly point-of-care (POC) ethanol detection in human breath with fast response and recovery times.

6.2 Salient outcomes of the thesis

The salient outcomes of the thesis can be highlighted in the following ways,

- Non-enzymatic urea detection in raw milk sample
- Room temperature carbon monoxide gas sensing in ppm level
- Room temperature acetone gas sensing
- Paper based disposable sensor for ethanol detection
- Breath analyzer prototype for ethanol sensing in human breath

6.3 Future scope

The work in the present thesis can be extended for future study in the following ways,

- The MWCNT-SH composite based non-enzymatic sensor can also be targeted to detect urea concentrations in water bodies and agricultural fields.

- The surface of MWCNTs can be modified with other suitable functional groups for the detection of various environmental pollutants such as NO, NO_2, H_2S, CO_2, SO_2, and other volatile organic compound gases.
- Metal based nanomaterial heterojunction can be used to detect various volatile organic compounds apart from acetone sensing with MoS_2-CuO nanocomposite, as discussed.
- The paper based disposable sensor can also be targeted for other biosensing applications by incorporating suitable enzymes on sensing material surface.

APPENDIX – I

Publications, Patents, Conferences, and Awards

Publications:

From Thesis:

- Non-enzymatic urea sensing based on MWCNT nanocomposite. **Nirmal Roy,** Shirsendu Mitra, Harshal B. Nemade, and Tapas K. Mandal, ***IEEE Sensors Journal***, 21 (17), 18417-18424, 2021. **DOI:** 10.1109/JSEN.2021.3088752

- Highly sensitive room temperature CO gas sensor based on MWCNT-PDDA composite. **Nirmal Roy**, Rupam Sinha, Thomas T. Daniel, Harshal B. Nemade and Tapas K. Mandal, ***IEEE Sensors Journal***, 20 (22), 13245-13252, 2020. **DOI:** 10.1109/JSEN.2020.3004994

- Paper based enzymatic chemiresistor for POC detection of ethanol in human breath. **Nirmal Roy,** Shirsendu Mitra, Nayan Mani Das, Nilanjan Mandal, Dipankar Bandyopadhyay, Harshal B. Nemade, and Tapas K. Mandal, ***IEEE Sensors Journal***, 20 (5), 2278-2286, 2020. **DOI:** 10.1109/JSEN.2019.2952940

- Synthesis of MoS_2-CuO nanocomposite for room temperature acetone gas sensing application. **Nirmal Roy**, Rupam Sinha, Harshal B. Nemade, and Tapas K. Mandal. (*Manuscript under review*)

Outside Thesis:

- Multimodal chemo-/magneto-/phototaxis of 3G CNT-bots to power fuel cells. Shirsendu Mitra, **Nirmal Roy**, Surjendu Maity, and Dipankar Bandyopadhyay, ***Microsystems & Nanoengineering***, 6 (19), 1-12, 2020. **DOI:** 10.1038/s41378019-0122-x

- Growth of carbon dot-decorated ZnO nanorods on a graphite-coated paper substrate to fabricate a flexible and self-powered Schottky diode for UV detection. Rupam Sinha, **Nirmal Roy**, and Tapas K. Mandal, ***ACS Applied Materials & Interfaces***, 12 (29), 33428-33438, 2020. **DOI:** 10.1021/acsami.0c10484

- N-doped carbon dot from cigarette-tobacco: Picric acid sensing in real water sample and synthesis of CD-MWCNT nano-composite for UV-photodetection. Rupam Sinha**, Nirmal Roy**, Ravula Rajasekhar, Aabhas Karnawat, and Tapas K. Mandal, ***Journal of Environmental Chemical Engineering***, 9 (1), 104971, 2021. **DOI:** 10.1016/j.jece.2020.104971

- SWCNT/ZnO nanocomposite decorated with carbon dots for photoresponsive supercapacitor applications. Rupam Sinha, **Nirmal Roy**, and Tapas K. Mandal, ***Chemical Engineering Journal***, 431, 133915, 2022. **DOI:** 10.1016/j.cej.2021.133915

- A simple uric acid sensor based on organic electrochemical transistor. **Nirmal Roy**, Nilanjan Mandal, and Tapas K. Mandal. (*Manuscript under preparation*)

Patents:

- Paper based flexible and self-powered UV photodetector. Rupam Sinha, **Nirmal Roy**, and Tapas K. Mandal, ***202031051178***, 2020.

- Point-of-care detection of ethanol in human breath and other analytes. **Nirmal Roy**, Shirsendu Mitra, Dipankar Bandyopadhyay, Harshal B. Nemade, and Tapas K. Mandal, ***201931040108***, 2019.

Conferences:

- Synthesis of surface modified carbon nanotube composite for environmental pollutant sensing application. **Nirmal Roy** and Tapas K. Mandal, ***7th International Conference on Advanced Nanomaterial and Nanotechnology (ICANN-2021)***, IIT Guwahati, India, 2021. (Oral)

- PDDA functionalized MWCNT composite as room temperature CO sensor. **Nirmal Roy**, Rupam Sinha, and Tapas K. Mandal, ***International Conference on Advances in Sustainable Research for Energy and Environmental Management (ASREEM-2021),*** SVNIT Surat, India, 2021. (Oral)

- Paper based sensor for alcohol detection and its application as breath analyzer. **Nirmal Roy** and Tapas K. Mandal, ***International Conference on Advances in Chemical Engineering-2020 (AdChE-2020),*** UPES Dehradun, India. (Oral)

- A disposable chemiresistive sensor based on Multiwall carbon nanotubes for alcohol detection. **Nirmal Roy** and Tapas K. Mandal, ***6th International Conference on Advanced Nanomaterial and Nanotechnology (ICANN-2019)***, IIT Guwahati, India, 2019. (Poster)

- Surface modification of Multiwall carbon nanotubes and its applications on alcohol detection. **Nirmal Roy** and Tapas K. Mandal, ***National Conference on Advanced Nanomaterials and their Applications (ANA-2018),*** MNNIT Allahabad, India. (Oral)

- Multiwall carbon nanotube based chemi-resistive sensor for urea detection. **Nirmal Roy** and Tapas K. Mandal, ***12th International Conference on Complex Fluids and Soft Matter (COMPFLU -2018)***, IIT Roorkee, India. (Poster)

- MWCNT, AuNP nanocomposite based POCT sensor for quantitative detection of urea in biological samples. **Nirmal Roy** and Tapas K. Mandal, ***Research Conclave 2018***, IIT Guwahati, India. (Poster)

Awards:

Best Oral Presentation Award, ***International Conference on Advances in Sustainable Research for Energy and Environmental Management (ASREEM-2021)***, SVNIT Surat, India. PDDA functionalized MWCNT composite as room temperature CO sensor. **Nirmal Roy**, Rupam Sinha, and Tapas K. Mandal.

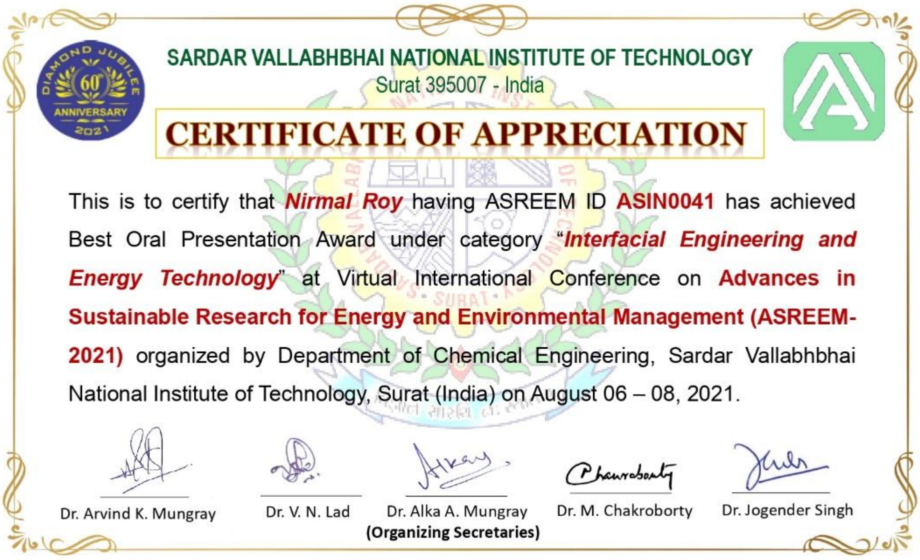

SARDAR VALLABHBHAI NATIONAL INSTITUTE OF TECHNOLOGY
Surat 395007 - India

CERTIFICATE OF APPRECIATION

This is to certify that ***Nirmal Roy*** having ASREEM ID **ASIN0041** has achieved Best Oral Presentation Award under category "***Interfacial Engineering and Energy Technology***" at Virtual International Conference on **Advances in Sustainable Research for Energy and Environmental Management (ASREEM-2021)** organized by Department of Chemical Engineering, Sardar Vallabhbhai National Institute of Technology, Surat (India) on August 06 – 08, 2021.

Dr. Arvind K. Mungray
Dr. V. N. Lad
Dr. Alka A. Mungray
(Organizing Secretaries)
Dr. M. Chakroborty
Dr. Jogender Singh